JRC TECHNICAL REPORTS

The European Commission Atmospheric Observatory

2017 Report

J.P. Putaud, P. Bergamaschi, F. Cavalli, A. Dell'Acqua, K. Douglas, I. Goded, F. Grassi, C. Gruening, N.R. Jensen, F. Lagler, G. Manca, S. Martins Dos Santos, M. Matteucci, R. Passarella, V. Pedroni.

2019

Joint Research Centre

EUR 29638 EN

Contact information
Name: Jean-Philippe Putaud
Address: European Commission, Joint Research Centre, Ispra, Italy
E-mail: jean.putaud@ec.europa.eu

EU Science Hub
https://ec.europa.eu/jrc

JRC 115241

EUR 29638 EN

PDF ISBN 978-92-79-99284-1 ISSN 1831-9424 doi:10.2760/698101

Print ISBN 978-92-79-99283-4 ISSN 1018-5593 doi:10.2760/982200

Luxembourg: Publications Office of the European Union, 2019

All content © European Union 2019, except: *Fig. 1 (background from Google Earth), Fig. 14 (EMEP), Fig. 18 (Thermo Scientific), Fig. 55 (Gill Instruments), Fig. 56 (LI-COR), Fig. 57 (Wikipedia), and Fig. 58 (*Schlumberger Water Services*).*

How to cite this report: Putaud, J.P., Bergamaschi, P., Cavalli, F., Dell'Acqua, A., Douglas, K., Goded, I., Grassi, F., Gruening, C., Jensen, N.R., Lagler, F., Manca, G., Martins Dos Santos, S., Matteucci, M., Passarella, R., Pedroni, V., *The European Commission Atmospheric Observatory: 2017 report*, EUR 29638 EN, Publications Office of the European Union, Luxembourg, 2019, ISBN 978-92-79-99284-1, doi:10.2760/698101, JRC115241.

Contents

Abstract 1

1 Introduction 3

2 Quality management system 4

3 Greenhouse gas concentration monitoring at the JRC-Ispra site 7

3.1 Location 7

3.2 Measurement programme 7

3.3 Instrumentation in Building 5 9

3.3.1 Sampling 9

3.3.2 Analyses 9

3.4 Instrumentation in the new Atmospheric Observatory (Bd 77R) 11

3.4.1 Air sampling 11

3.4.2 Analyses 11

3.5 Overview of measurement results 14

4 Short-lived atmospheric species at the JRC-Ispra site 21

4.1 Introduction 21

4.1.1 Location 21

4.1.2 Underpinning programmes 21

4.2 Measurements and data processing 25

4.2.1 Air pollutant and short-lived radiative forcer measurements at the JRC- Ispra station in 2017 25

4.2.2 Measurement techniques 26

4.2.3 On-line data acquisition system/data management 37

4.2.4 Data evaluation 38

4.3 Quality assurance 41

4.4 Results for the year 2017 43

4.4.1 Meteorology 43

4.4.2 Gas phase air pollutants 43

4.4.3 Particulate phase 47

4.4.4 Wet deposition chemistry 63

4.5 Results of year 2017 in relation to 30+ years of measurements 65

4.5.1 Sulphur and nitrogen compounds 65

4.5.2 Particulate matter mass 67

4.5.3 Ozone 67

4.5.4 Aerosol micro-physical and optical properties 69

4.6 Conclusions 69

5. Atmosphere – Biosphere flux monitoring at the forest station of San Rossore 73

5.1 Location and site description 73
5.2 Measurements in 2017 75
5.3 Description of the instruments 76
  5.3.1 Infrastructural 76
  5.3.2 Ecosystem fluxes 76
  5.3.3 Radiation instruments 78
  5.3.4 Meteorological sensors 78
  5.3.5 Soil instruments 78
  5.3.6 Flux data processing 81
5.4 Results of the year 2017 83
  5.4.1 Meteorology 83
  5.4.2 Radiation 83
  5.4.3 Soil variables 85
  5.4.4 Eddy covariance flux measurements 85
References 88
Links 90
List of figures 91
List of tables 94

Abstract

Following the set-up of the greenhouse gas measurements in November 2016, the equipment for measuring short-lived pollutants and climate forcers was moved to the Atmospheric Observatory at the site of the historical EMEP-GAW site of the JRC in Ispra by July 1997. A comprehensive set of essential atmospheric variables have since then been measured at this single site to continue the assessment of the impact of European policies and international conventions on air pollution and climate forcing that started in 1985. The variables we measure at the Atmospheric Observatory in Ispra include greenhouse gas concentrations (CO_2, CH_4, N_2O, SF_6), radon (^{222}Rn) activity concentration, short-lived gaseous and particulate pollutant (CO, SO_2, NO, NO_2, O_3, $PM_{2.5}$ and its main ionic and carbonaceous constituents) concentrations, atmospheric particle micro-physical characteristics (number concentration and size distribution) and optical properties (light scattering and absorption in-situ, light scattering and extinction vertical profiles remotely), eutrophying and acidifying species (SO_4^{2-}, NO_3^-, NH_4^+) wet deposition. On-line measurements data are available in real time at http://abc-is.jrc.ec.europa.eu/. Vegetation ⇆ atmosphere exchanges (CO_2, O_3, H_2O and heat) are measured at our Mediterranean Forest Flux Station of San Rossore, backed up by meteorological and pedological measurements. All measurements are performed under international projects and programmes including ICOS (Integrated Carbon Observation System), ACTRIS (Aerosols, Clouds and Trace gases Research Infra-Structure), EMEP (co-operative Programme for Monitoring and Evaluation of the long range transmission of air pollutants in Europe) and GAW (Global Atmosphere Watch), each of which requires the use of standard methods and scales, and the participation in quality assurance activities. The JRC has a leading role in ACTRIS and EMEP regarding the quality assurance for carbonaceous aerosol measurements. Data obtained at Atmospheric Observatory are submitted to international open data bases (www.europe-fluxdata.eu, fluxnet.ornl.gov, www.ingos-infrastructure.eu, ACTRIS Data Portal) and can be freely downloaded from these web sites. The data we produce are used in European wide assessments, for model inputs and validation, and for calibrating satellite airborne sensors. The European Commission Atmospheric Observatory 2017 report presents the data produced during the past year in the context of the previous years of measurements.

All the essential in-situ and remote sensing measurements scheduled for 2017 were regularly performed across the year, except for short periods needed for moving, calibrating, and maintaining the equipment.

Greenhouse gas (GHG) measurements have been performed at the JRC Ispra site since October 2007. Minimum values of CH_4, N_2O and SF_6 measured in Ispra under clean air conditions are close to marine background values, while CO_2 mixing ratios can even be lower than the Mace Head baseline due to the continental biospheric CO_2 sink. Deviations from baseline concentrations provide information about regional and larger scale European greenhouse gas sources. From our daytime measurements, we derived increasing trends in CO_2 (+0.5% yr^{-1}) and CH_4 (+0.4% yr^{-1}) between 2008 and 2017, and in N_2O (+0.3% yr^{-1}) between 2001 and

2017. ICOS-compliant GHG measurements from the 100 m high tower of our new Atmospheric Observatory in Ispra started in December 2016.

While CO concentrations slightly decreased (-2%) in 2017 compared to 2016, the concentrations of other short-lived pollutants monitored at the Atmospheric Observatory (NO_2, O_3, atmospheric particulate matter) have all increased by about 5 to 15%. In contrast, NH_4^+, NO_3^-, and SO_4^{2-} wet deposition decreased (between -15 and -30%), but the number of acid rain events jumped from 3 in 2016 to 8 in 2017. These observations can be at least in part explained by the weather conditions, 2017 being exceptionally dry compared both to 2016 and to the decadal 1990-2000 average. In general, 2017 did not break the general decreasing trend in atmospheric pollution observed in Ispra since 1986. A noticeable exception regards ozone (O_3), whose concentrations have remained relatively high in 2017. The indicators for health and ecosystem safeguard have deteriorated since 2012 (2014 excluded) compared to the 2000's. It would be worth studying the geographical extent of this tendency across Europe to understand its origin.

The long time series in O_3 indices and PM related variables (particle light scattering, particle number and wintertime mass concentrations, …) suggest that a break in the decreasing trend in air pollution observed over the past 3 decades occurred around year 2014. This was particularly dramatic for O_3, whose indicators for vegetation and human safeguard reached levels barely or never observed at the JRC-Ispra site in the past. Regarding particulate pollution, increased mass and number concentrations could have adverse effects on health. However, the increase in visible light scattering seen over the recent years is not accompanied by a similar increase in light absorption. This "lightening" of the atmospheric aerosol means that the negative radiative forcing (climate cooling) potential of the atmospheric particles encountered in our area has started to increase again. These observed changes in the long-term trends of particulate and O_3 pollution would of course need to be confirmed over several more years and at other observatories to have a wider scientific and policy-relevant significance.

The atmosphere ⇆ vegetation exchange measurements at our Mediterranean forest flux station of San Rossore show that the pine tree forest is a net sink for CO_2 (510 gC/m² absorbed in 2017). The sequence of alternate wet and dry years since 2013 (when the measurement site was moved 600 m inland) allows us to observe that the total annual precipitation amount is not a key factor for determining the annual carbon sequestration by this Mediterranean.

1 Introduction

The mission of the Atmosphere-Biosphere-Climate Integrated monitoring Station (ABC-IS) is to measure changes in atmospheric variables to obtain data that are essential for the conception, development, implementation and monitoring of the impact of European policies and International conventions on air pollution and climate change. Measurements include greenhouse gas concentrations, forest ⇆ atmosphere fluxes, and concentrations of pollutants in the gas phase, particulate matter and precipitations, as well as aerosol micro-physical and optical characteristics. Most measurements are performed at the JRC-Ispra site (Fig. 1), and some at the typical Mediterranean site of San Rossore site (Fig. 51). The goal of ABC-IS is to establish real world interactions between air pollution, climate change and the biosphere, highlighting possible trade-offs and synergies between air pollution and climate change policies. Possible interactions include the role of pollutants in climate forcing and CO_2 uptake by vegetation, the impact of climate change and air pollution on CO_2 uptake by vegetation, the effect of biogenic emission on air pollution and climate forcing, etc…

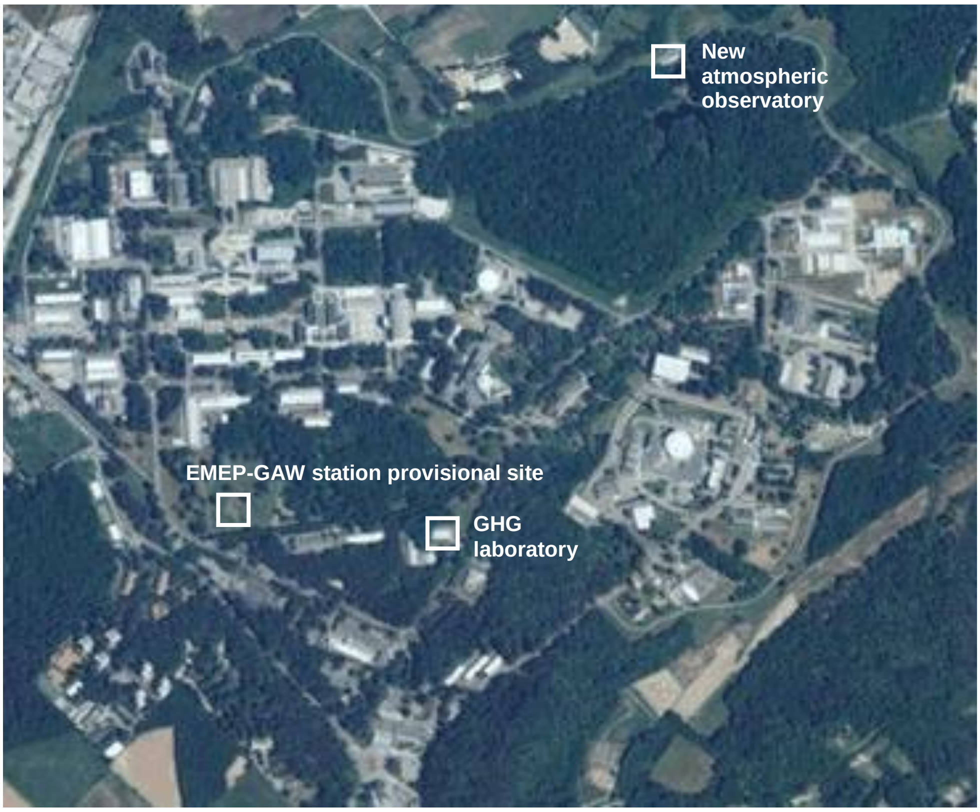

Fig. 1: The JRC-Ispra site and the location of the provisional EMEP-GAW site, the greenhouse gas laboratory, and the new atmospheric observatory, built on the spot of the historical EMEP-GAW station.

Measurements are performed in the framework of international monitoring programmes like the European Research Infrastructure Consortium project ICOS (Integrated Carbon Observation System), EMEP (Co-operative programme for monitoring and evaluation of the long range transmission of air pollutants in Europe of the UN-ECE *Convention on Long-Range Transboundary Air Pollution* CLRTAP) and GAW (the Global Atmosphere Watch programme of the World Meteorological Organization). The infrastructure has also been used in competitive projects (e.g. ACTRIS, InGOS).

Through the participation of the Atmospheric Observatory in international networks, inter-laboratory comparisons are conducted and standard methods are developed within the European Reference Laboratory for Air Pollution of the JRC Air and Climate Unit.

2 Quality management system

The European Commission Atmospheric Observatory is a research infrastructure of JRC's *Directorate for Energy, Transport and Climate*.

We achieved ISO 9001 certification in 2010 and re-certification in 2013 and in 2016, all by external audits, which is also valid for the year 2017 (ISO 9001 is mainly about "project management"). In addition, internal ISO 9001 audit was performed successfully in 2017.

In addition, JRC Ispra also achieved in 2010 the ISO 14001 certificate (ISO 14001 is mainly about "environmental issues"), which was valid for several years: In 2017, external audits took place at JRC-Ispra (achieving again the ISO 14001 certificate).

For information (the links below being accessible to JRC staff only), the "quality management system (QMS) for the Atmospheric Observatory" includes server space at the following links:

\\ies.jrc.it\H02\H02QMS_year_2017_

\\ies.jrc.it\H02\LargeFacilities\ABC-IS\

\\ies.jrc.it\H02\Laboratories

\\ies.jrc.it\H02\Laboratories\LifeCycleSheets

where the following information can be found: list of instruments; information about calibrations; standards used and maintenance; standard operational procedures (SOP's); instrument lifecycle sheets and log-books; manuals for the instruments; *etc*. For additional specific details about QMS, for the year 2017 and the Atmospheric Observatory, see e.g. the file 2017_Instruments'_calibration_&_standards_&_maintenance.xls, that can be found under \\ies.jrc.it\H02\LargeFacilities\ABC-IS\Quality_management.

More QMS information/details can also be found in the sections "Measurement techniques" in this report.

More general QMS information/documentations about how the AC Unit (H02/C5) was run in 2017, the management of all of the projects within the Unit and the running of the Atmospheric Observatory can also be found at

\\ies.jrc.it\h02\H02QMS_year_2017_\1_Unit\QMS_info\QMS_documents_and_Unit

\\ies.jrc.it\h02\H02QMS_year_2018_\1_Unit\QMS_info\QMS_documents_and_Unit

and specially in the seven C5 Unit QMS documents listed here (latest versions):

QMS_DIR_C_C5_Quality_Unit_Management_Manual_v12_0.pdf
QMS_C5_MANPROJ_PROJ_Laboratory_Management_v11_0.pdf
QMS_C5_MANPROJ_PROJ_Model_Management_v11_0.pdf
QMS_C5_MANPROJ_PROJ_Informatics_Management_v11_0.pdf
QMS_C5_MANPROJ_PROJ_Knowledge_Management_v11_0.pdf
QMS_C5_MANPROJ_PROJ_Review_Verification_Validation_Approval_v7_0.pdf
QMS_C5_MANPROJ_PROJ_Administration_Implementation_v6_0.pdf

The latest versions of these documents are available at:

\\ies.jrc.it\H02\H02QMS_year_2018_\1_UNIT\QMS_info\QMS_documents_and_Unit.

Fig. 2: The laboratories for atmospheric GHG measurements at Building 5 with 15m mast (left), and at the new JRC Atmospheric Observatory with the 100m-tall tower (Building 77r).

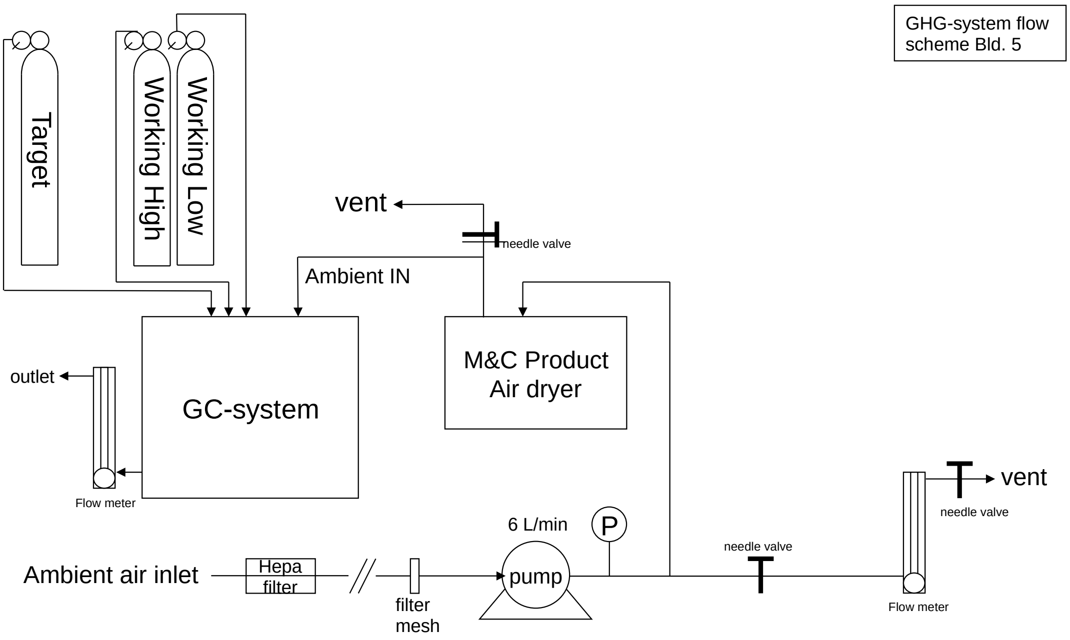

Fig. 3: Bd 5 GHG-system flow scheme

3 Greenhouse gas concentration monitoring at the JRC-Ispra site

3.1 Location

The JRC monitoring station at Ispra is currently the only low altitude measurement site for greenhouse gases (GHGs) near the Po Valley. The unique location of the station at the South-Eastern border of Lake Maggiore in a semi-rural area at the North-Western edge of the Po Valley allows sampling of highly polluted air masses from the Po Valley during meteorological conditions with southerly flow, contrasted by situations with northerly winds bringing relatively clean air to the site. A high-resolution modelling study analysed in detail the sensitivity of the atmospheric concentrations at the monitoring station [*Bergamaschi and Brunner, 2015*]. The sensitivity usually shows a significant diurnal cycle, during night dominated by the area 40-60 km around the station, while daytime footprints are much larger, typically dominated by distances of more than 60 km. During summer daytime, the radius τ_{s50} (at which the cumulative surface sensitivity reaches 50% of the total sensitivity) is about 187 km on average. Furthermore, the diurnal cycle in local wind direction due to the regional mountain - lake/valley wind system leads to a significant diurnal cycle of the sensitivity (north-west vs. south-east), especially during summer time.

The main cities around the station are Varese, 20 km east of the station, Novara, 40 km south, Gallarate - Busto Arsizio, about 20 km southeast, and Milan, 60 km south-east of the station. The JRC GHG station has been setup in 2007 at Building 5 (Fig. 2) of the JRC Ispra site (45.807°N, 8.631°E, 223 m asl) and has been operated at that location continuously since end 2007 until June 2018 and has been discontinued afterwards. In 2016 a new station building inside the JRC premises (building 77r, 45.8147°N, 8.6360°E, 210 m asl) has been completed. The new station includes a 100m tower on top of the station building (Fig. 2), with platforms every 20 m. End of 2016 the new station has been equipped with a new GHG instrument and sampling system, with multiple sampling lines at 40, 60, and 100m. The new GHG station has been integrated into the European Integrated Carbon Observation System (ICOS) network (https://www.icos-ri.eu/) and received the ICOS certificate at the ICOS General Assembly on 30 November 2018.

3.2 Measurement programme

The GHG monitoring station in building 5 is in operation since October 2007, complementary to the JRC-Ispra EMEP-GAW station, which started in 1985 [*Putaud et al., 2018*], and to the flux measurement tower in the forest of San Rossore. GHG measurements at the new Atmospheric Observatory started end of November 2016. The new GHG station has successfully passed the second step of the official ICOS labelling procedure on 06 November 2018 and received the ICOS certificate at the ICOS General Assembly on 30 November 2018. The station is now an official "ICOS class-2" atmospheric station, which requires continuous CO_2, CH_4 and meteorological measurements, following strictly the ICOS guidelines (which includes rigorous standardization of instrumentation, sampling, calibration, QA/QC and centralized data processing).

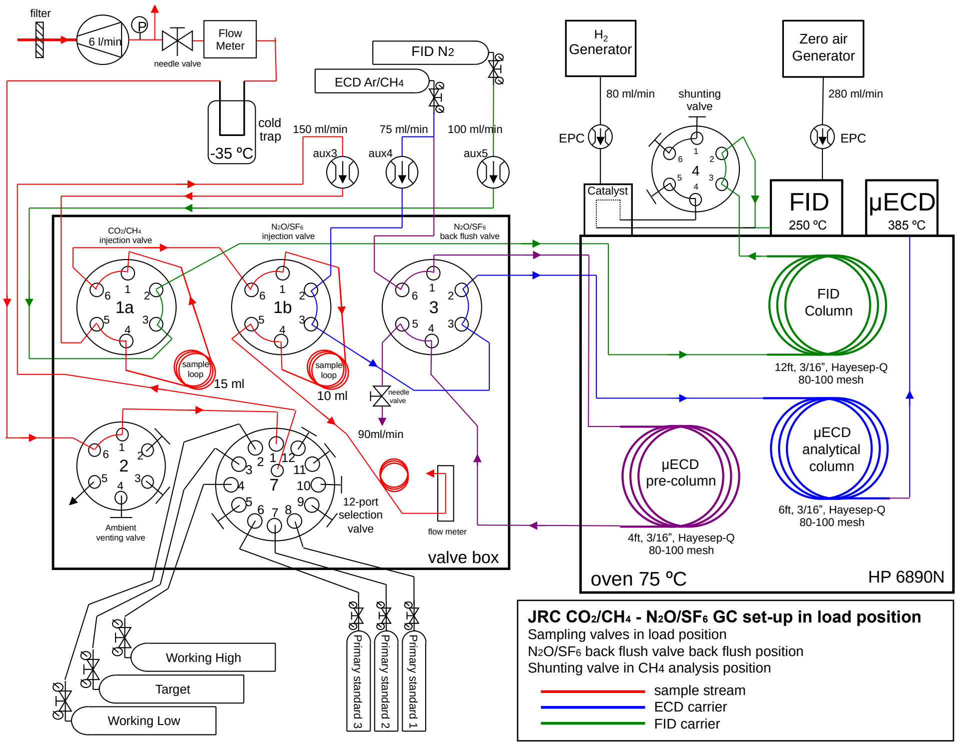

Data File C:\CHEM32\1\DATA\ISPRA\AMBIENT_20150807 2016-10-19 16-11-58\SIG10017.D
Sample Name: AMBIENT

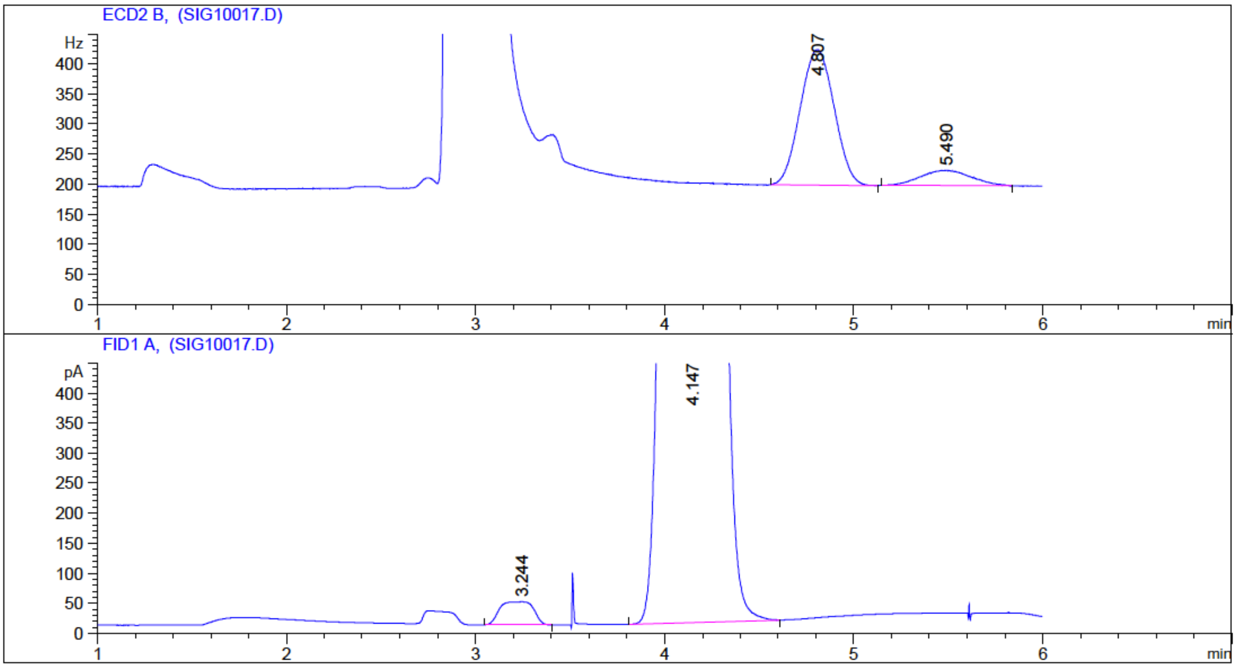

Fig. 4: The top panel shows a schematic of the GC-system set-up. Typical chromatograms are shown in the lower panels.

The GHG station in Building 5 has been run until end of June 2018 (providing overlapping measurements from both stations during an 18 month period) and has been discontinued afterwards.

3.3 Instrumentation in Building 5

3.3.1 Sampling

Air samples in Building 5 are collected on the top of a 15 m high mast via a 50 m ½" Teflon tube at a flow rate of ~6 L /min using a KNF membrane pump (KNF N811KT.18). The sampled air is filtered from aerosols by a Pall Hepa filter (model PN12144) positioned 10 m downstream of the inlet and dried cryogenically by a commercial system from M&C TechGroup (model EC30 FD) down to a water vapour content of <0.015%v before being directed to the analyzer. The remaining water vapour is equivalent to a maximum 'volumetric error' of <0.06 ppmv of CO_2 or <0.3 ppbv of CH_4 or <0.05 ppbv N_2O. A schematic overview of the sample flow set-up is shown in Fig. 3.

3.3.2 Analyses

3.3.2.1 Gas Chromatograph Agilent 6890N (S/N US10701038)

Continuous monitoring at 6 minute time resolution of CO_2, CH_4, N_2O, and SF_6 is performed with an Agilent 6890N gas chromatograph equipped with a Flame Ionization Detector (FID) and micro-Electron Capture Detector (µECD) using a set-up described by *Worthy el al.* (1998). The calibration strategy has been adopted from *Pepin et al.* (2001) and is based on a Working High (WH) and Working Low (WL) standard (namely bracketing standards), which are calibrated regularly using NOAA primary standards. The WH and WL are both measured 2 times per hour for calculating ambient mixing ratios, and a target (TG) sample is measured every 6 hours for quality control. The working standards and target cylinders are filled with synthetic air, while NOAA primary standards are filled with real air.

N_2O concentrations were also calculated using a second calibration strategy that is based on the one-point-reference method with a correction for non-linearity of µECD. The non-linear response of the µECD was estimated using NOAA primary standards and then it has been applied to the entire time series. This second method improves the quality of the time series when the bracketing standards do not cover the range for N_2O ambient concentrations (i.e. range too large or range that does not include ambient concentrations). GHG measurements are reported as dry air mole fractions (mixing ratios) using the WMO NOAA2004 scale for CH_4, the WMOX2007 for CO_2 and the NOAA2006A scale for N_2O and SF_6. We apply a suite of five NOAA tanks ranging from 369-523 ppm for CO_2, 1782-2397 ppb for CH_4, 318-341 ppb for N_2O, and 6.1-14.3 ppt for SF_6 as primary standards. The GC control and peak integration runs on *ChemStation* commercial software. Further processing of the raw data is based on custom built software developed in C language and named GC_6890N_Pro. A schematic of the GC-system set-up and typical chromatograms are shown in Fig. 4.

In March 2016 all the GC columns were replaced with new ones. The new columns have the same properties as the old columns. The nickel catalyst used to convert CO_2 to CH_4 was replaced during the same intervention.

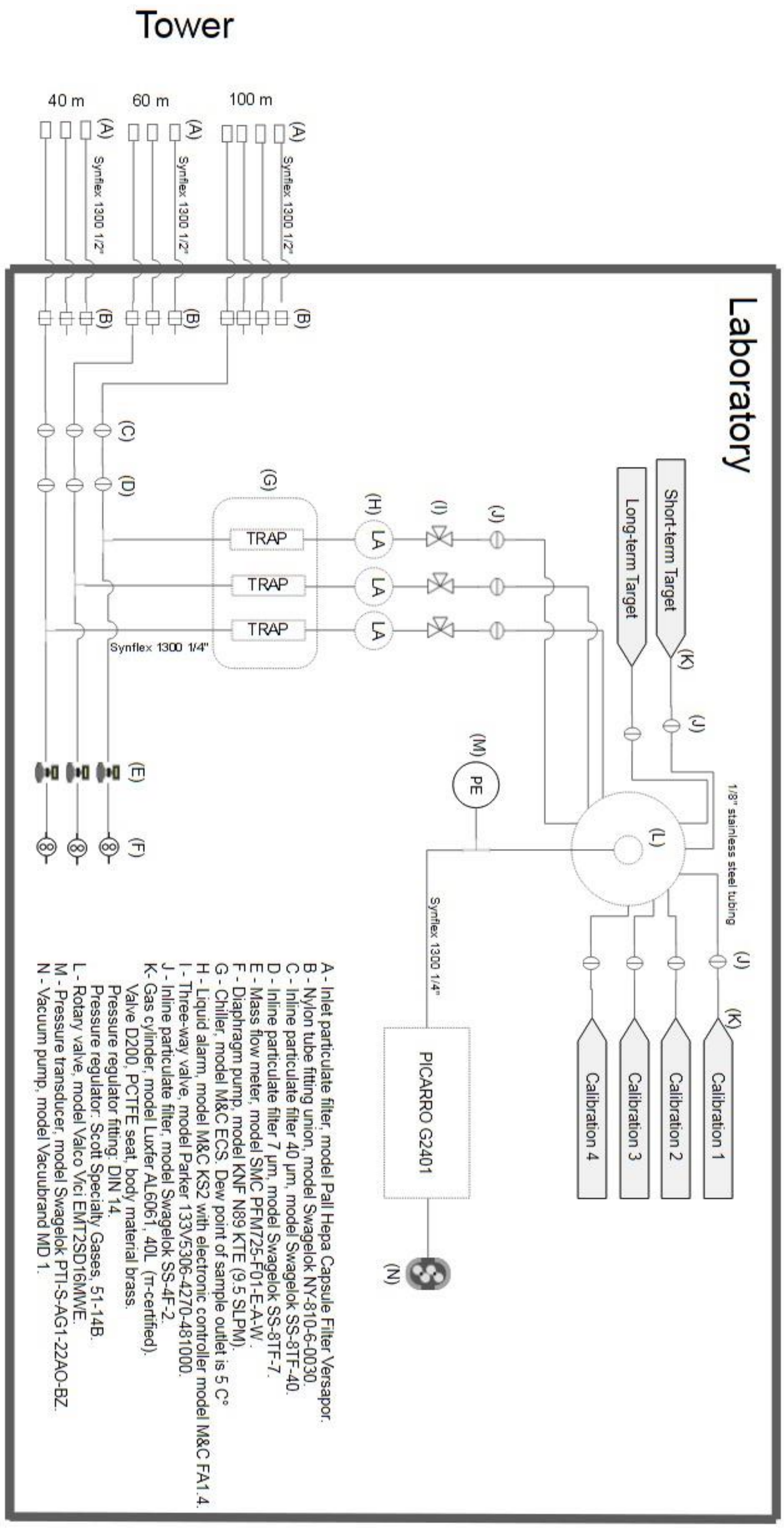

Fig. 5: Sampling, conditioning and distribution system diagram for the GHG measurements at the new Atmospheric Observatory (Building 77r).

The different types of uncertainties affecting the GC measurements have been estimated using the algorithms developed in the InGOS ("Integrated non-CO2 Greenhouse gas Observing System") project (http://www.ingos-infrastructure.eu/). These uncertainties are defined as follows:

- 'Working standard repeatability' is calculated as the 24-hours centered moving, 1σ standard deviation of the bracketing standards (or reference standard in case of the one-point-reference method).
- 'Laboratory internal scale consistency uncertainty' (LISC) is the median of the difference between measured and assigned values of the target gas. The median is calculated for different time periods where GC settings were constant (including the used working standards and target gas).
- 'Monthly reproducibility' represents the values of the smoothed target residuals. Smoothing is performed with a centered running median with a window length of 30 days.

'Scale transfer and non-linearity uncertainty' is based on the uncertainty of the assigned working standard concentration and it accounts for the uncertainty introduced by scale transfer from NOAA standards to the working standards.

3.3.2.2 Radon analyser ANSTO (custom built)

^{222}Radon activity concentrations in Bq m^{-3} have been semi-continuously monitored (30 minute time integration) applying an ANSTO dual-flow loop two-filter detector (Zahorowski et al., 2004) since October of 2008 till December 2016 [*Putaud et al., 2018*]. In December 2016 the detector has been moved to the new Atmospheric Observatory (Building 77r).

3.4 Instrumentation in the new Atmospheric Observatory (Bd 77R)

3.4.1 Air sampling

Air samples are collected at the different levels on the tower using ½" Synflex tubes at a flow rate of ~9 L min^{-1}. Each sampling line is provided with a KNF diaphragm pump (KNF N89 KTE) and three different particulate filters: a Pall Hepa Capsule Versapor filter at the inlet, and two filters with nominal pore size of 40 μm and 7 μm (model Swagelok SS-8TF-40 and SS-8TF-7, respectively).

A small air flow (around 0.2 L min^{-1}) is diverted from the main line toward the Picarro G2401 instrument using a dedicated vacuum pump (model Vacuubrand, MD1) located downstream to the analyser. This flow is partially dried by a chiller (M&C Techground, model ECS) to a dew point of 5 °C. A liquid water alarm is located downstream of the chiller to prevent any liquid water reaching the analyser.

3.4.2 Analyses

3.4.2.2 Cavity Ring-Down Spectrometer Picarro G2401 (S/N 2326-CFKADS2193)

The GHG laboratory at the new Atmospheric Observatory (Building 77r) is equipped with a Picarro G2401 Cavity Ring-Down Spectrometer that measures concentrations of CO_2, CH_4, CO and H_2O with a time resolution of 5 seconds. Concentrations are measured at three levels on the tower: 40 m, 60 m and 100 m above ground level (Fig. 5). A rotary valve, model Valco Vici EMT2SD16MWE, allows to select the tower level to be analysed.

The Picarro G2401 instrument directly controls this valve in order to sample the three levels sequentially within one hour. Measurement sequence is showed in Table 1.

Table 1: Measurement sequence of Picarro G2401. This cycle is repeated continuously every hour.

Sampling Level	**Sampling duration (minutes)**
100 m	15 (first 5 min rejected)
60 m	15 (first 5 min rejected)
100 m	15 (first 5 min rejected)
40 m	15 (first 5 min rejected)

The calibration strategy for the Picarro G2401 instrument is based on four gas tanks provided by ICOS CAL laboratory (https://www.icos-cal.eu/). Performance of the Picarro G2401 instrument has been evaluated using a short-term target (measured once a day since June 2017) and a long-term target (measured once a month since June 2017). Both targets were provided by ICOS-CAL laboratory.

3.3.2.3 Radon analyser ANSTO (custom built)

Measurements of ^{222}Rn at the Atmospheric Observatory (Building 77r) started in December 2016, after the move of the ANSTO radon monitor from Building 5 to Building 77r. Air sample is taken from a separate inlet at 100 m above ground by using a blower (Becker, model SV 8.130/1-01). A 500 L decay tank was placed in the inlet line to allow for the decay of Thoron (^{220}Rn with a half-life of 55.6 s) before reaching the ^{222}Radon monitor. The ANSTO ^{222}Radon monitor has been calibrated once a month using a commercial passive ^{226}Radium source from Pylon Electronic Inc. (Canada) inside the calibration unit with an activity of 21.99 kBq, which corresponds to a ^{222}Radon delivery rate of 2.77 Bq min^{-1}. The lower detection limit is 0.02 Bq m^{-3} for a 30% precision (relative counting error). The total measurement uncertainty is estimated to be <5% for ambient ^{222}Radon activities at Ispra.

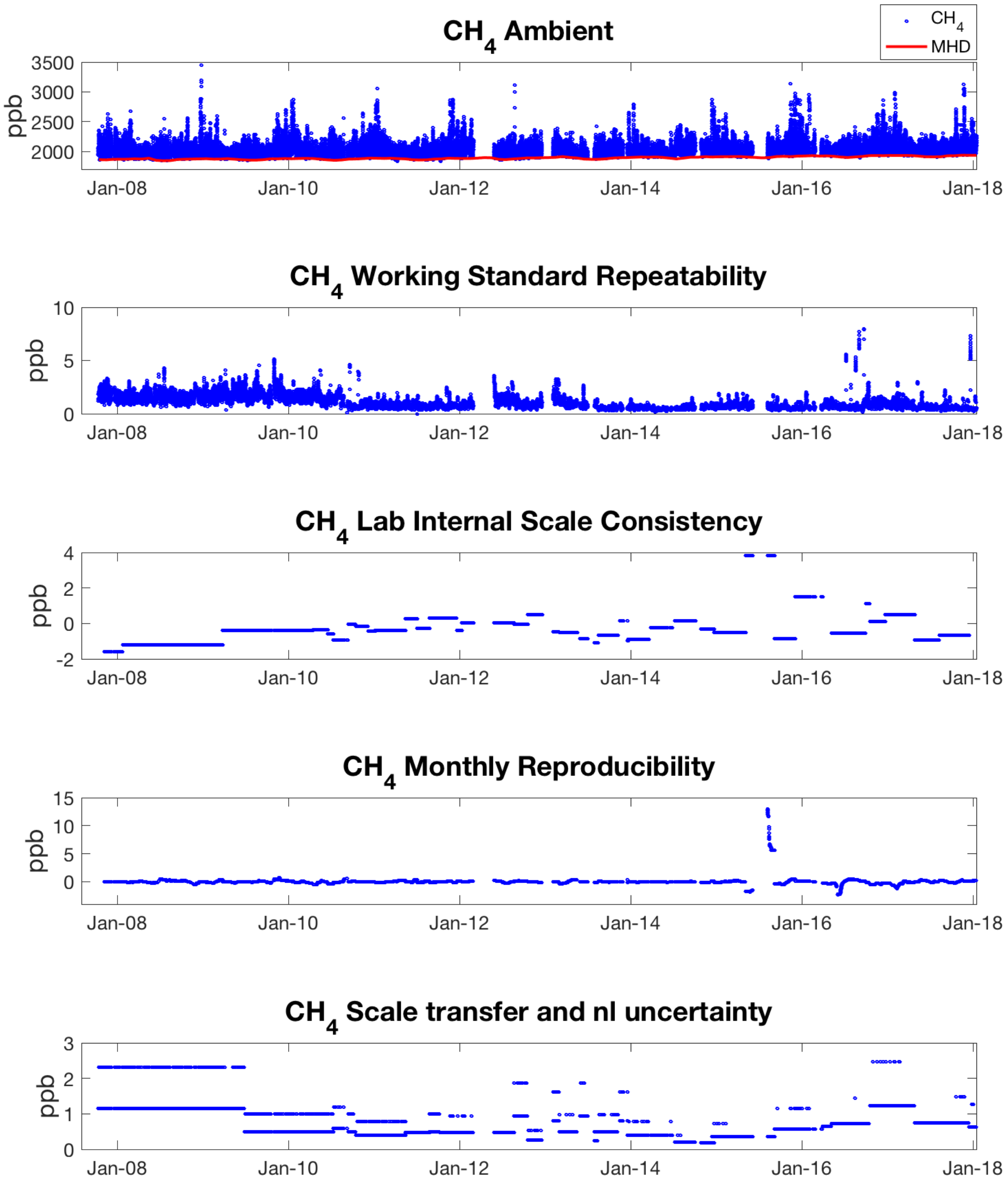

Fig. 6: Time series of continuous CH_4 ambient measurements at Ispra (Building 5) between October 2007 and December 2017 with associated uncertainties. CH_4 ambient concentrations are reported as hourly mean values of dry air mole fractions. Furthermore, monthly mean concentrations from the background station Mace Head (MHD) on the West coast of Ireland are also included (Mace Head data from Simon O'Doherty, University of Bristol).

3.5 Overview of measurement results

Fig. 6, 7, 8 and 9 give an overview of the GC GHG measurements in building 5 since the start of measurements in October 2007 until December 2017. These figures show also the uncertainties of the ambient concentrations; the 'scale transfer and non-linearity' uncertainty has been calculated only for CH_4 and N_2O. For N_2O and SF_6 only data since 15/09/2010 are shown. Before this date there was a dilution problem of the sample loop connected to the column of the µECD detector. The flushing of the sample loop during ambient measurement was not sufficient to remove completely the carrier gas used in the previous analysis. The N_2O data shown in Figure 7 are calculated using the one-point-reference method (see above).

Measurements collected in Building 5 are plotted together with the monthly mean baseline data from the Mace Head (Ireland) station to illustrate the Atlantic background mixing ratios. Minimum values of CH_4, N_2O and SF_6 measured at the JRC-Ispra site are close to the Mace Head baseline, while CO_2 mixing ratios can be lower than the Mace Head baseline due to the continental biospheric CO_2 sink.

During summer 2015 the GC has undergone a significant maintenance in which the jet of the FID detector, the multi-position rotary valve and the nickel catalyser were replaced. After the maintenance, the precision of CO_2 measurements was worse than before because of the continuous decrease in the efficiency of the new nickel catalyst used to convert the CO_2 into methane. This catalyser has been replaced in March 2016. Afterward, the precision of CO_2 measurements has returned to typical values observed before summer 2015.

During the period October 2016 – April 2017 precision of CH_4 measurements was worse than before because of the too large range covered by working standards cylinders. In particular the WH bracketing standard concentration was too high (3135 ppb) compared to ambient concentrations observed in Ispra.

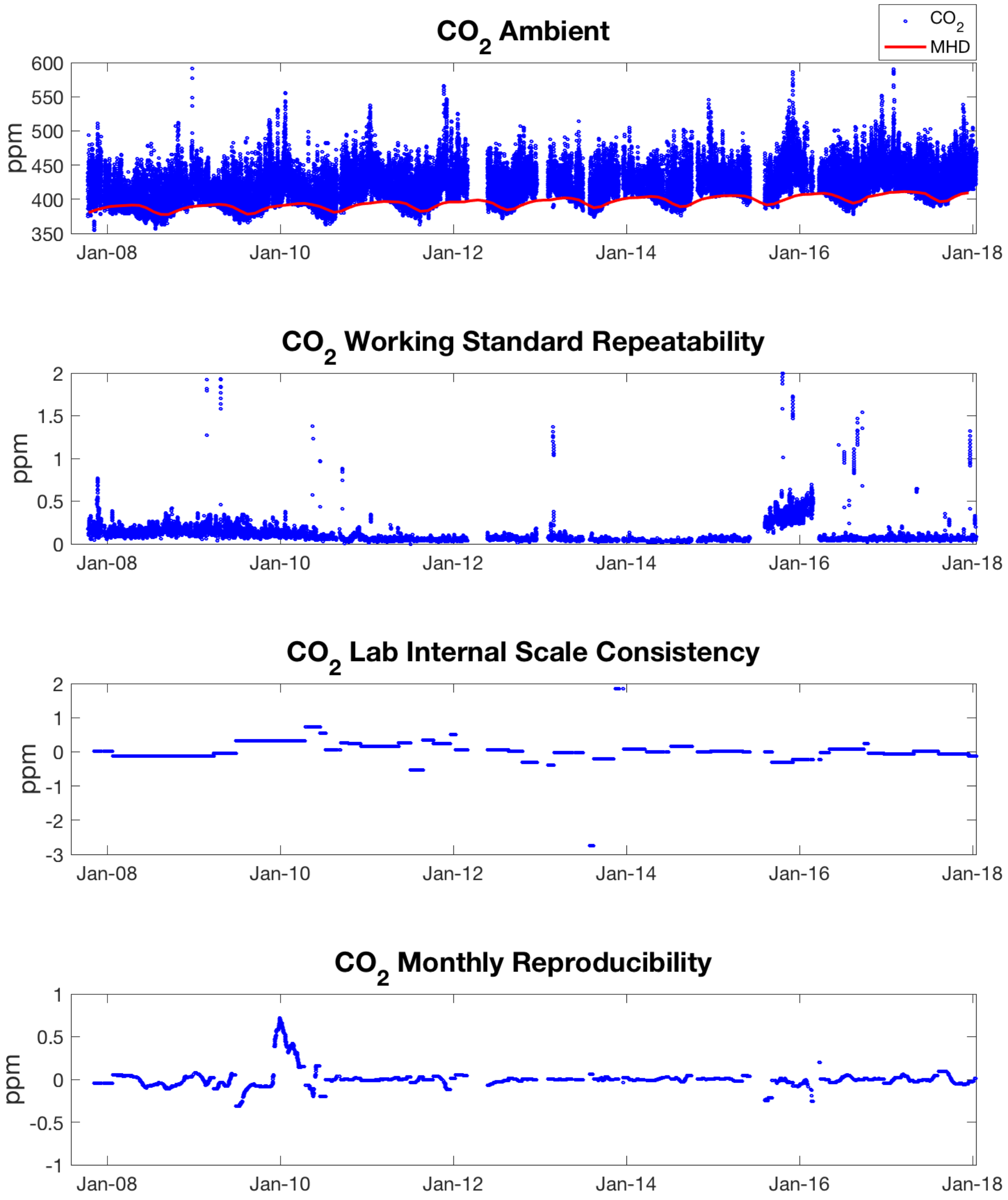

Fig. 7: Time series of continuous CO_2 ambient measurements at Ispra (Building 5) between October 2007 and December 2017 with associated uncertainties. CO_2 ambient concentrations are reported as hourly mean values of dry air mole fractions. Furthermore, flask measurements from the background station Mace Head (MHD) on the West coast of Ireland are also included (Dlugokencky, et al., 2017).

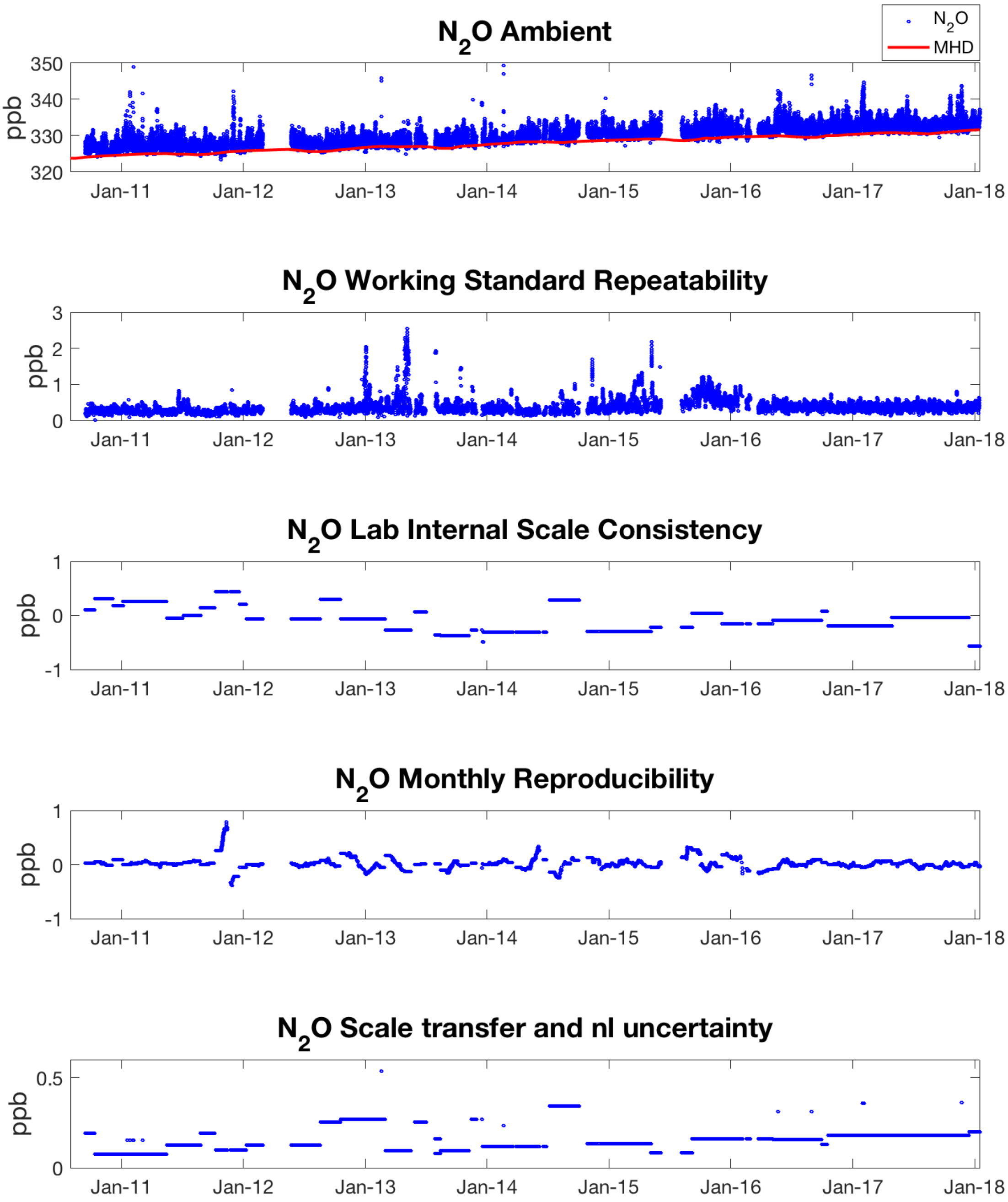

Fig. 8: Time series of continuous N_2O ambient measurements at Ispra (Building 5) between September 2010 and December 2017 with associated uncertainties. N_2O ambient concentrations are reported as hourly mean values of dry air mole fractions. Furthermore, monthly mean concentrations from the background station Mace Head (MHD) on the West coast of Ireland are also included (Mace Head data from Simon O'Doherty, University of Bristol).

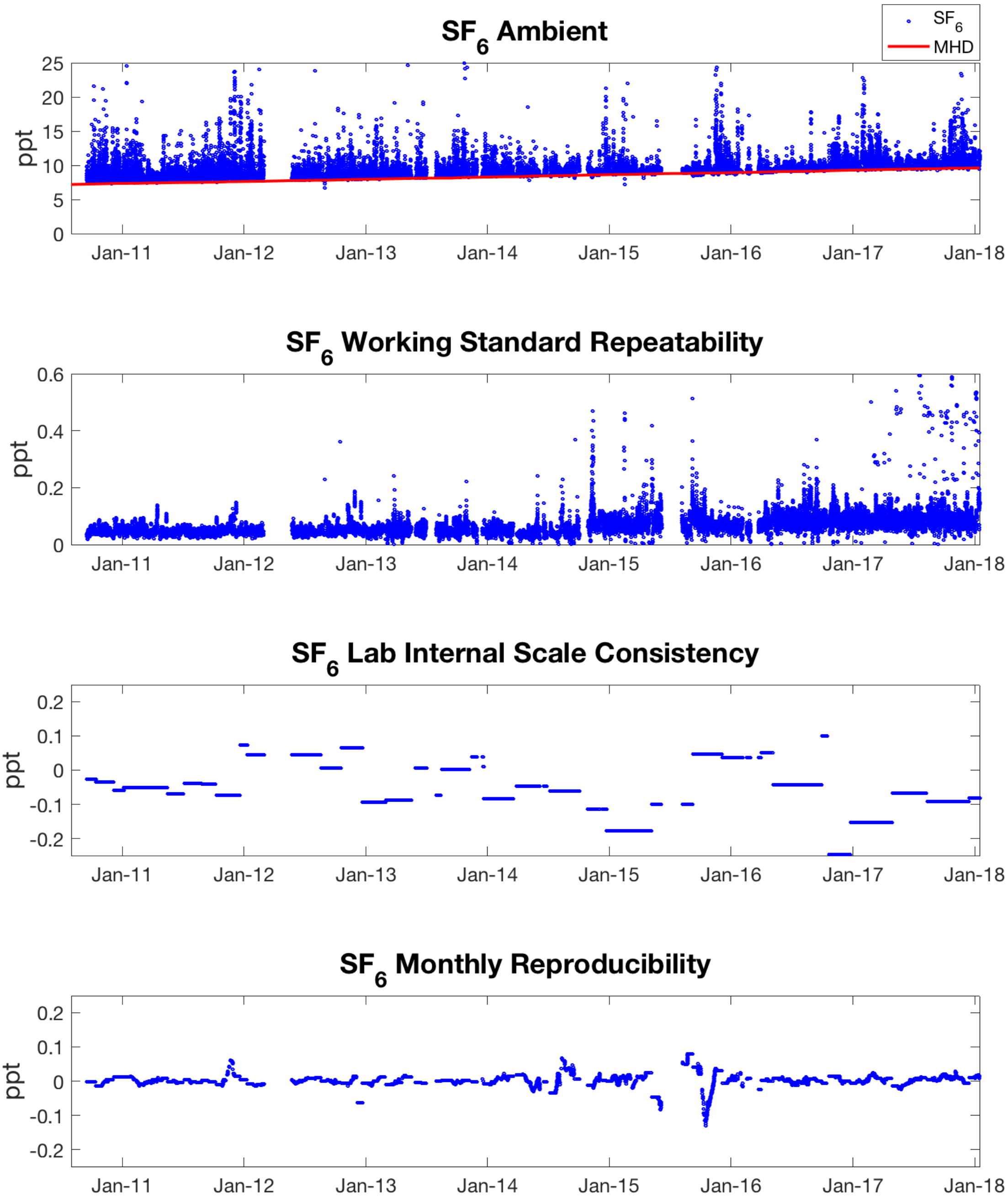

Fig. 9: Time series of continuous SF$_6$ ambient measurements at Ispra (Building 5) between September 2010 and December 2017 with associated uncertainties. SF$_6$ ambient concentrations are reported as hourly mean values of dry air mole fractions. Furthermore, monthly mean concentrations from the background station Mace Head (MHD) on the West coast of Ireland are also included (Mace Head data from Simon O'Doherty, University of Bristol).

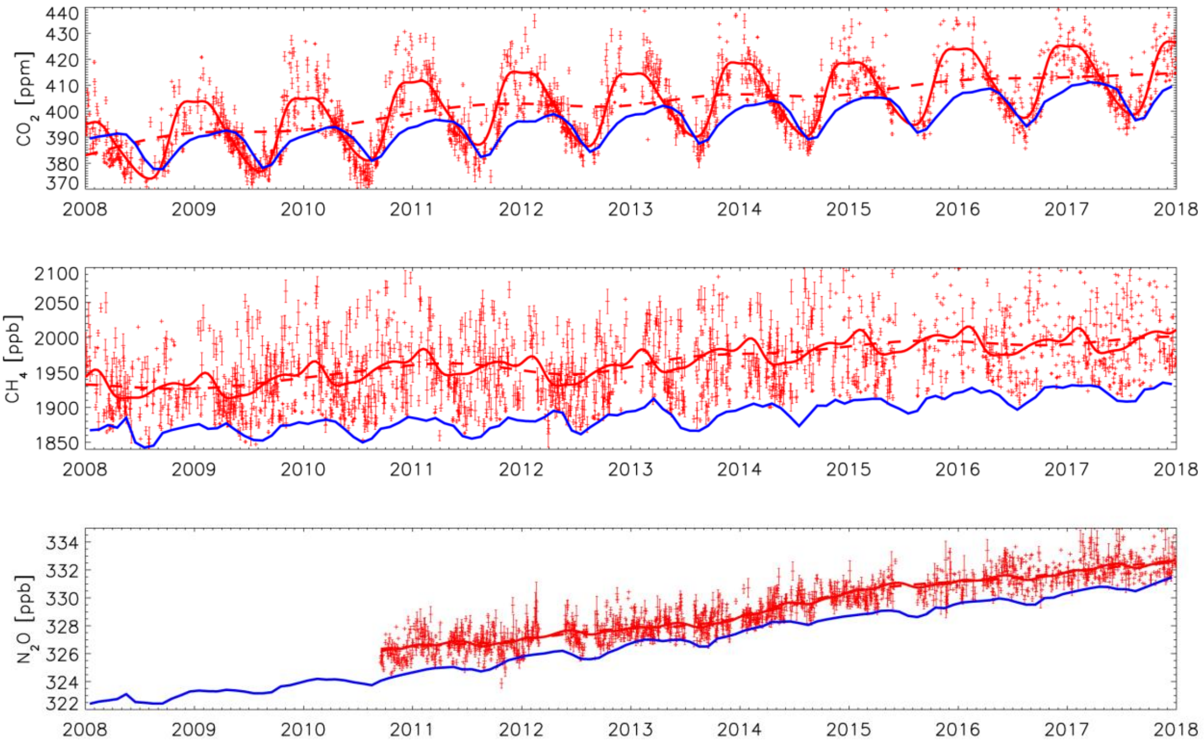

Fig. 10: Trends in atmospheric GHG concentrations. Top panel: CO_2; middle panel: CH_4; lower panel: N_2O. The figures show daily average values, using only daytime measurements (between 12:00 and 15:00 LT) and excluding GHG measurements under stagnant meteorological conditions (with wind speed below 0.5 ms^{-1}). Solid red line: fit to daily data (based on NOAA fitting procedure [Thoning et al., 1989]); dashed red line: trend derived from fitting procedure; blue solid line: baseline concentrations at Mace Head.

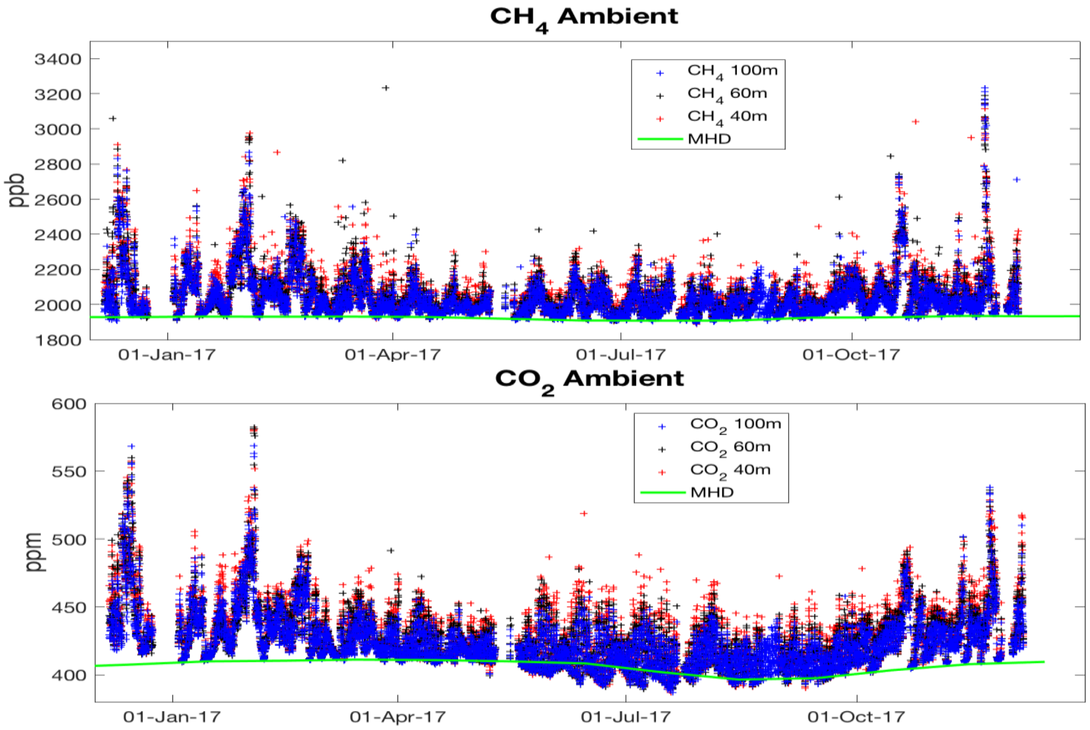

Fig. 11: Time series of continuous CH_4 and CO_2 ambient measurements at the Atmospheric Observatory (Bd 77r), sampled at three different heights (40m, 60m, 100m), between December 2016 and December 2017. Concentrations are reported as hourly mean values of dry air mole fractions. Furthermore, monthly mean concentrations from the background station Mace Head (MHD) on the West coast of Ireland are also included (Mace Head data from Simon O'Doherty, University of Bristol).

Fig. 10 shows the time series of daily average CO_2, CH_4, and N_2O dry air mole fractions, using only daytime measurements (between 12:00 and 15:00 LT) and excluding GHG measurements under stagnant meteorological conditions (with wind speeds below 0.5 m s^{-1}). In order to further analyse the trends and seasonal variations we applied the NOAA fitting procedure [*Thoning et al., 1989*]. For CH_4 we derive an average trend of 6.9 ppb yr^{-1} between 2008 and 2017, which is virtually identical to the observed global CH_4 trend of 6.9 ± 2.6 ppb yr^{-1} during this period (www.esrl.noaa.gov/gmd/ccgg/trends_ch4/). Also for N_2O, the derived trend at Ispra of 0.87 ppb yr^{-1} is close to the global trend of 0.93 ppb yr^{-1} during the last 10 years [*WMO, 2018*]. The very close correspondence of the trends in CH_4 and N_2O at Ispra with the global trends is also reflected in the almost constant (or only very small trends) in the offset between the average concentrations at Ispra and the Mace Head baseline. This suggests that the regional CH_4 and N_2O emissions in the catchment area of the Ispra station were almost constant during the analysis period 2008-2017 (for N_2O: 09/2010-2017).

For CO_2, we derive an average trend of 3.2 ppm yr^{-1} between 2008 and 2017, compared to a global trend of 2.2 ± 0.5 ppm yr^{-1} (https://www.esrl.noaa.gov/gmd/ccgg/trends/). The interpretation of the CO_2 trends at Ispra, however, is complicated by the large seasonal variation of the biospheric CO_2 fluxes. The larger CO_2 trend derived from the data at Ispra is largely driven by the relatively low summertime CO_2 values during 2008-2010, indicating a relatively strong biospheric CO_2 uptake in the catchment area of the Ispra station during these years.

Fig. 11 shows measurements of CH_4, CO_2, and CO at the Atmospheric Observatory (Building 77r) at three different heights above ground (100m, 60m and 40m) between December 2016 and December 2017. Monthly mean baseline data from Mace Head station is also plotted to illustrate the Atlantic background mixing ratios.

Typically the CH_4, CO_2, and CO concentrations show significant gradients during night (when the stable nocturnal boundary layers is developed), but are usually very close at all three heights during day (when tracers are usually well-mixed in the boundary layer).

Finally, Fig. 12 shows hourly mean ^{222}Radon activities measured in Building 77r at 100m level. These concentrations are significantly lower than the previously observed values in Building 5, mainly because of the different sampling height of the two sites.

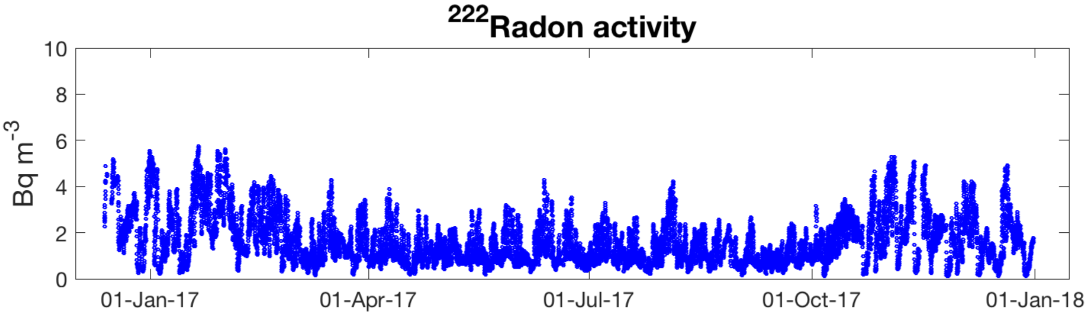

Fig. 12: ^{222}Rn measurements at Atmospheric Observatory (building 77r). The figure shows the time series of hourly mean ^{222}Radon activity, collected at 100m height, between December 2016 and December 2017.

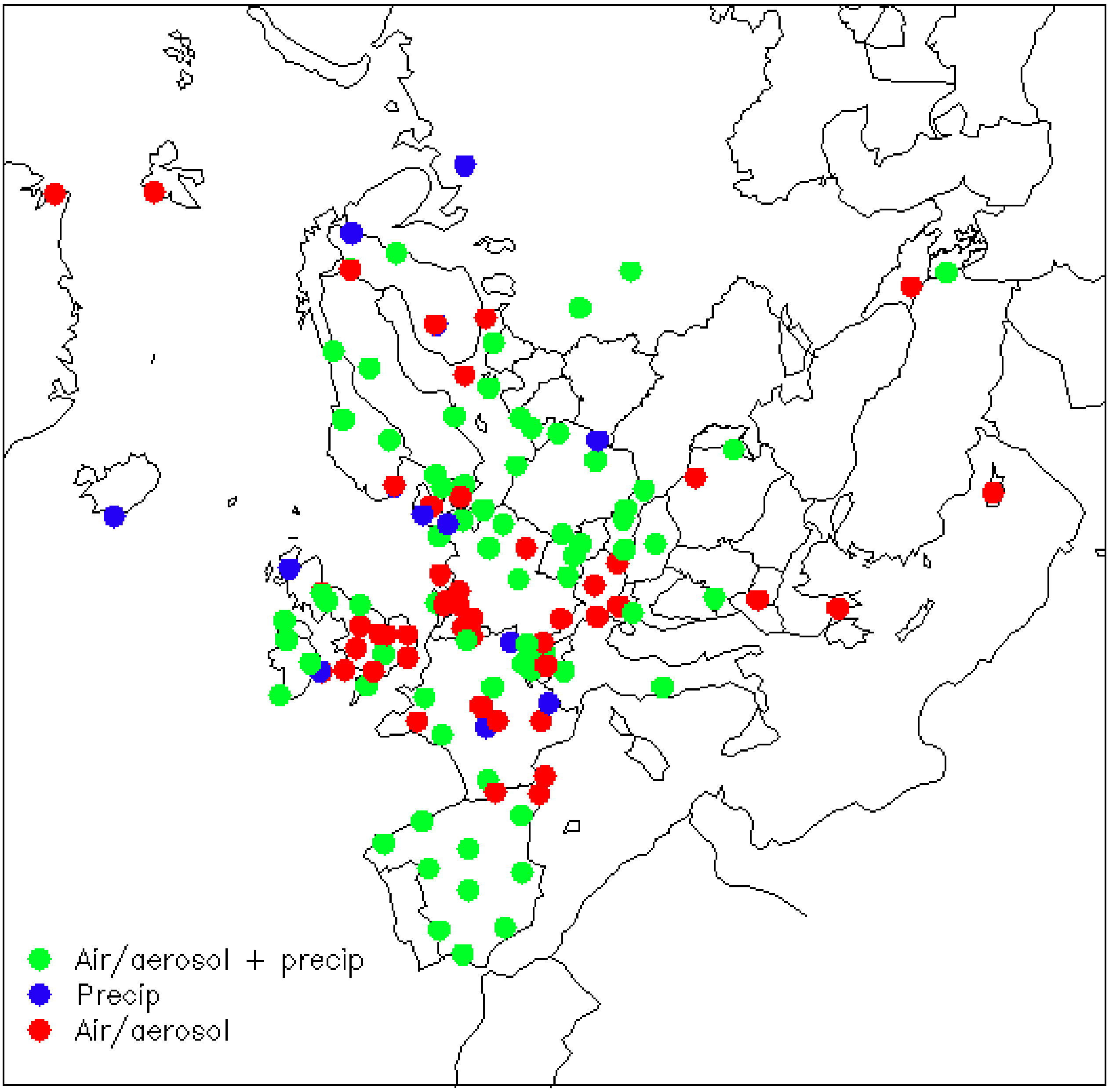

Fig. 13: most recent map of the EMEP stations across Europe (2014) made available by the Chemical co-ordinating Centre (CCC).

4 Short-lived atmospheric species at the JRC-Ispra site

4.1 Introduction

4.1.1 Location

Air pollution has been monitored since 1985 at the atmospheric observatory (45°48.881′N, 8°38.165′E, 209 m a.s.l.) located by the Northern fence of the JRC-Ispra site (see Fig. 1), situated in a semi-rural area at the NW edge of the Po valley in Italy. From the end of March 2013 until June 2017, the measurement of short-lived atmospheric species (Table 2) was performed at a provisional site (45°48.438′N, 8°37.582′E, 217 m a.s.l.), due to the reconstruction of the laboratory at the historical site (Fig. 1). However, gaseous pollutant measurements continued at the provisional site until December 2017 for comparison.

The nearest cities are Varese (20 km east), Novara (40 km south), Gallarate – Busto Arsizio (about 20 km south-east) and the Milan conurbation (60 km to the south-east). Busy roads and highways link these urban centres. Emissions of pollutants reported for the four industrial large point sources (CO_2 emissions > 1500 tons d^{-1}) located between 5 and 45 km NE to SE from Ispra also include 2 and 3 tons of CO per day, plus 3 and 5 tons of NOx (as NO_2) per day for the 2 closest ones (**PRTR emissions**, 2010).

4.1.2 Underpinning programmes

4.1.2.1 The EMEP programme (*http://www.emep.int/*)

Currently, about 50 countries and the European Community have ratified the **CLRTAP**. Lists of participating institutions and monitoring stations (Fig. 13) can be found at: ***http://www.nilu.no/projects/ccc/network/index.html***

The set-up and running of the JRC-Ispra EMEP station resulted from a proposal of the Directorate General for Environment of the European Commission in Brussels, in agreement with the Joint Research Centre, following the Council Resolution **N° 81/462/EEC**, article 9, to support the implementation of the EMEP programme.

The JRC-Ispra station has operated on a regular basis in the extended EMEP measurement programme since November 1985. Data are transmitted yearly to the EMEP Chemical Co-ordinating Centre (CCC) for data control and statistical evaluation, and available from the EBAS data bank (Emep Database, ***http://ebas.nilu.no/***).

4.1.2.2. The GAW programme (*http://www.wmo.int/web/arep/gaw/gaw_home.html*)

WMO's Global Atmosphere Watch (GAW) was established in 1989 with the scope of providing information on the physico-chemical composition of the atmosphere. These data provide a basis to improve our understanding of both atmospheric changes and atmosphere-biosphere interactions. GAW is one of WMO's most important contributions to the study of environmental issues, with about 80 countries participating in GAW's measurement programme. Since December 1999, the JRC-Ispra station is also part of the GAW coordinated network of regional stations. Data contributing to the GAW programme are also available via EBAS.

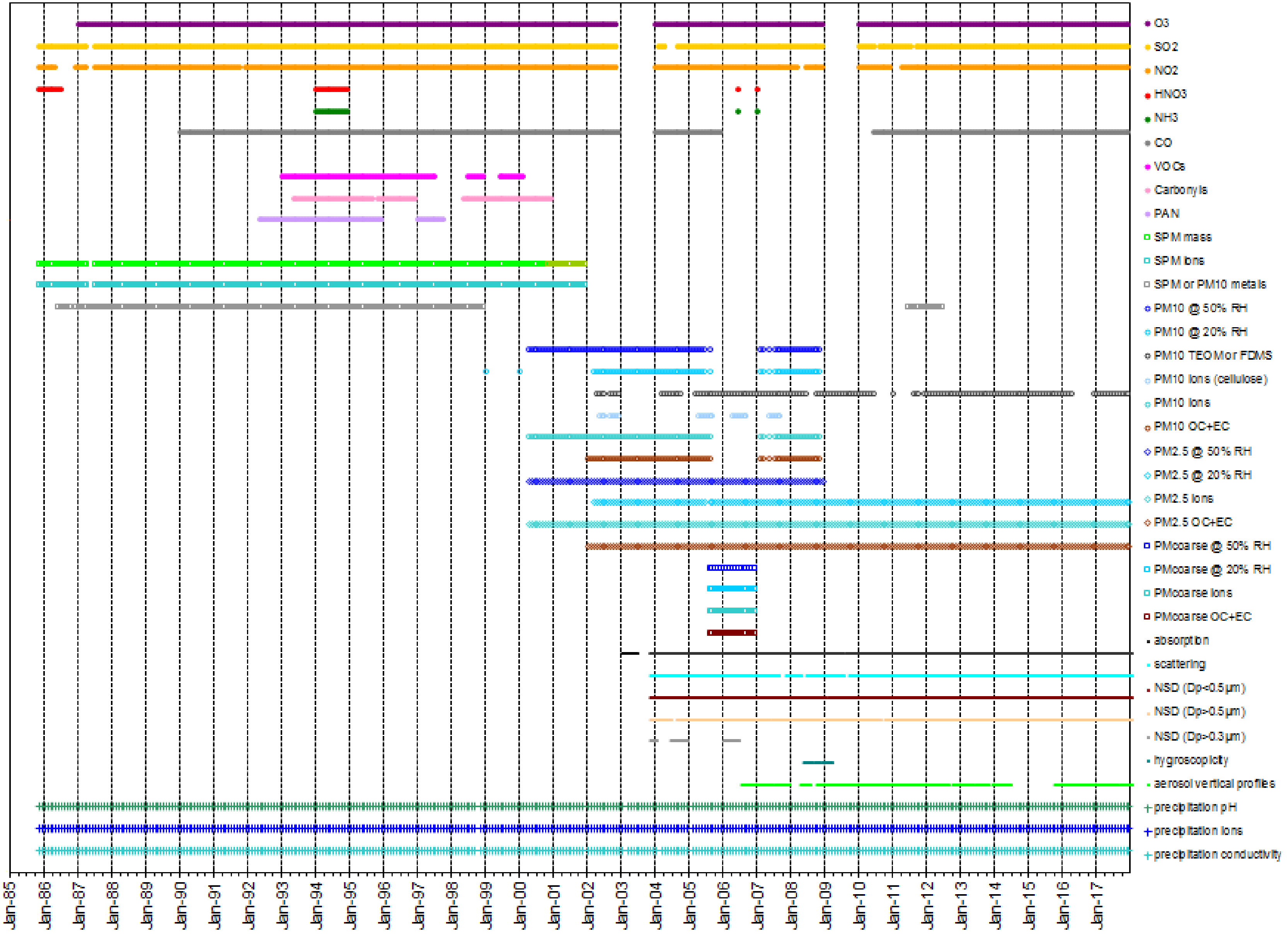

Fig. 14: Atmospheric short-lived species measurements performed at the JRC-Ispra atmospheric observatory since 1985.

.

4.1.2.3. The institutional programme (http:/ec.europa.eu/jrc/en/research-topic/air-quality)

Since 2002, the measurement programme of the air pollution monitoring station of JRC-Ispra has gradually been focused on short-lived climate forcers such as tropospheric ozone and aerosols and their precursors (Fig. 14). Concretely, more sensitive gas monitors were introduced, as well as a set of new measurements providing aerosol characteristics that are linked to radiative forcing. The station contributes to the "Ex-post analysis of transport emission standards" as listed in the JRC institutional project work plan 2018 (Project AIR, WP IACA, Deliverable 8).

The atmospheric observatory is also used for research and development purposes. Regarding particulate organic and elemental carbon, techniques developed by the Air and Climate unit in Ispra have been implemented and validated by international atmospheric research networks (EUSAAR, ACTRIS), recommended in the EMEP sampling and analytical procedure manual and adopted by the European Committee for Standardisation (CEN) as a standard method (EN16909:2017).

Currently, preliminary air pollution data obtained at the JRC-Ispra are visible and downloadable in real time from http://abc-is.jrc.ec.europa.eu. All validated data obtained at the JRC-Ispra station under the EMEP and the GAW programme, and other past and current international projects (EUSAAR, ACTRIS) can be retrieved from the EBAS database (*http://ebas.nilu.no/*), selecting "Ispra" as station of interest.

Additional information about the JRC-Ispra air monitoring station and other stations from the EMEP network can also be found in the following papers: Van Dingenen et al., 2004; Putaud et al., 2004; Mira-Salama et al., 2008; Putaud et al., 2010; Putaud et al., 2014; Cavalli et al.,2016.

Table 2: Variables related to short-lived pollutants and radiative forcers measured in 2017

METEOROLOGY	Pressure, temperature, humidity, wind, solar radiation
GAS PHASE	SO_2, NO, NO_X, O_3, CO
PARTICULATE PHASE	$PM_{2.5}$ mass, Cl^-, NO_3^-, SO_4^{2-}, $C_2O_4^{2-}$, Na^+, NH_4^+, K^+, Mg^{2+}, Ca^{2+}, OC, and EC contents Number size distribution (10 nm - 10 µm) Aerosol light absorption, scattering and back-scattering coefficients Altitude-resolved aerosol light back-scattering and extinction
WET DEPOSITION	Cl^-, NO_3^-, SO_4^{2-}, $C_2O_4^{2-}$, Na^+, NH_4^+, K^+, Mg^{2+}, Ca^{2+} pH, conductivity

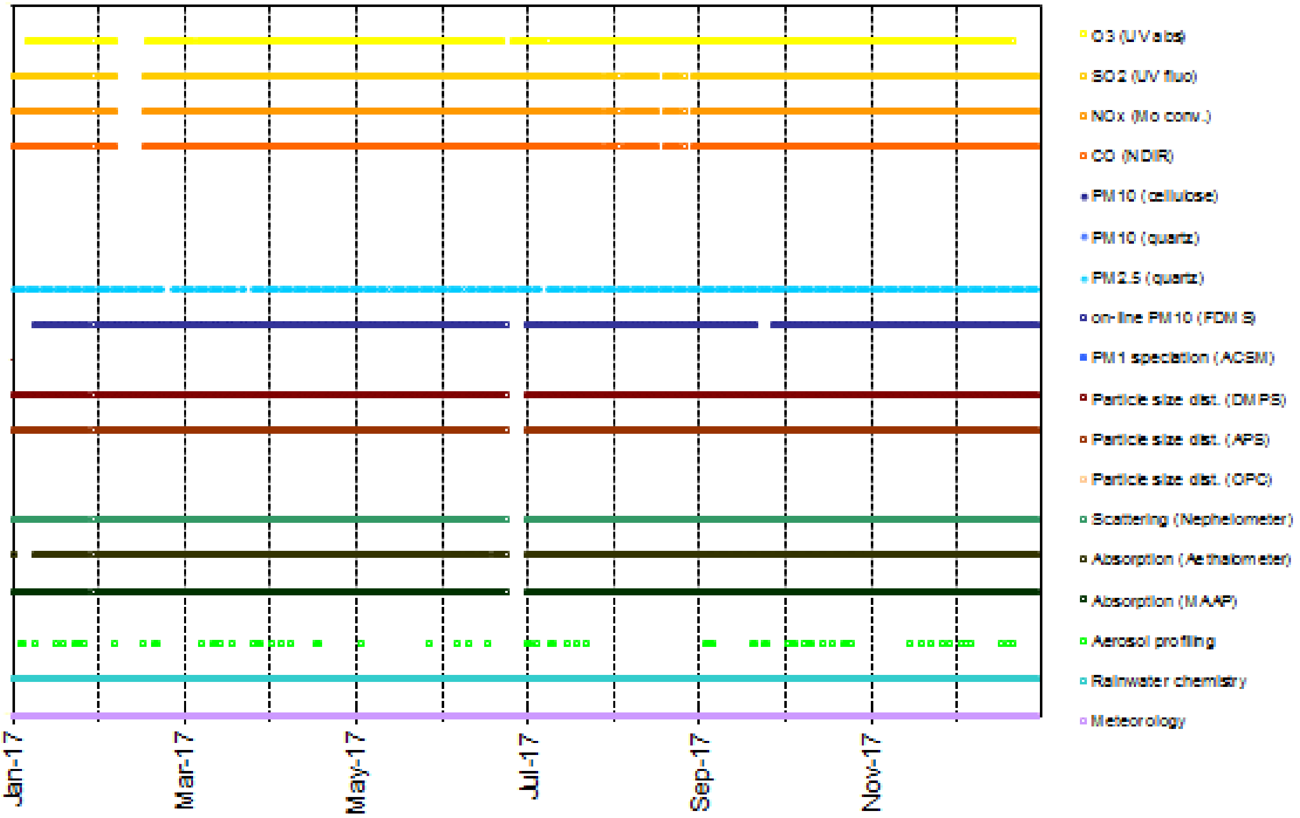

Fig. 15. Short-lived pollutants' data coverage for year 2017.

4.2 Measurements and data processing

4.2.1 Air pollutant and short-lived radiative forcer measurements at the JRC- Ispra station in 2017

Since 1985, the JRC-Ispra air monitoring station programme has evolved significantly (Fig. 14). The measurements performed at the JRC-Ispra in 2017 are listed in Table 2, and Fig. 15 shows the data coverage. Measurements were carried out at the provisional site till June and at the new atmospheric observatory from July.

Meteorological variables were measured continuously.

SO_2, O_3, NOx and CO were measured almost continuously during the year 2017, except for the period 7 – 16 Feb. due to annual revision of the mobile laboratory and maintenance/linearity checks of all analysers and for three 1 - 2 day gaps in July and August (x 3).

Daily particulate matter ($PM_{2.5}$) samples were collected and analysed for $PM_{2.5}$ mass (at 20% RH), main ions, OC (organic carbon) and EC (elemental carbon), for the whole of 2017, except for 10 days (sampler breakdowns).

On-line PM_{10} measurements (FDMS-TEOM, Filter Dynamics Measurement System - Tapered Element Oscillating Microbalance) were carried out only from Jan. 9th to Dec. 31st, except for 2 short periods of time due to the move to the new observatory (26 June – 2 July) and 24 – 28 Sept. (laboratory tests).

Particle number size distributions (10 nm < Dp < 10 µm), light scattering and light absorption coefficients were measured almost continuously (95 to 98% coverage) in 2017. The main gaps (26 June – 2 July) coincide with the move from the provisionalsite to the new atmospheric observatory.

The Raman LiDAR was operated according to the EARLINET schedule (Mon. at solar noon ±1 hr, at sunset -2,+3hr, Thu. at sunset -2,+3hr, and during the ESA satellite Calipso overpasses (± 1hr), weather and staff availability permitting.

Precipitation was collected throughout the year and analysed for pH, conductivity, and main ions (collected water volume permitting). Only a few major precipitation events were missed.

4.2.2 Measurement techniques

4.2.2.1 On-line monitoring

Meteorological Variables

Meteorological data and solar radiation were measured directly at the EMEP station with the instrumentation described below.

WXT510 (S/N: A1410010) at PS until 24.11.2017

WXT530 (S/N N2120878*) at AO from 11.10.2017*

Two WXT510 weather transmitters from Vaisala recorded the six weather variables temperature, pressure, relative humidity, precipitation and wind speed and direction from the top of a 10 m high mast at the provisional station, and from a 2 m mast on the terrace of the new observatory since Oct. 2017.

The wind data measurements utilise three equally spaced ultrasonic transducers that determine the wind speed and direction from the time it takes for ultrasound to travel from one transducer to the two others. Precipitation rate is measured with a piezoelectric sensor that detects the impact of individual raindrops and thus infers the accumulated rainfall. For the pressure, temperature and humidity measurements, separate sensors employing high precision RC oscillators are used.

Kipp and Zonen CMP 11 (S/N: 070289) at PS until 24.11.2017

Kipp and Zonen, SMP 11-V (S/N: 167256) *at AO from 11.10.2017*

To determine the total solar radiation, a Kipp and Zonen CMP11 Pyranometer has been installed in 2015, which measures the irradiance (in W/m^2) on a plane surface from direct solar radiation and diffuse radiation incident from the hemisphere above the device. The CMP11 that was installed on the top of the container (3 m above ground) was replaced by the SMP11 on the terrace of the new observatory in Oct. 2017. The measurement principle is based on a thermal detector. The radiant energy is absorbed by a black disc and the heat generated flows through a thermal resistance to a heat sink. The temperature difference across the thermal resistance is then converted into a voltage and precisely measured. The CMP11 features a fast response time of 12 s, a small non stability of +/-0.5 % and a small non linearity of +/-0.2 %.

Gas Phase Air Pollutants

Sampling

SO_2, NO, NO_x, O_3 and CO were measured from the mobile laboratory (plates number CM328CN), parked at the EMEP/GAW provisional station (PS) at JRC-Ispra (see Fig. 1) about 500 meters from the historical site until the end of December 2017, and simultaneously at the new atmospheric observatory (AO) at the same place as the historical site June 2017. Only data obtained at the PS across 2017 are reported here.

The sampling line at the mobile lab (inlet about 3.5 m above ground) consists of an inlet made of a stainless steel cylindrical cap (to prevent rain and bugs to enter the line), outside a stainless steel tube (diameter = about 4 cm), inside a Teflon tube (d = about 2.7 cm) and a "multi-channel distributor" tube, with ten ¼" connectors. This inlet is flushed by an about 45 L min^{-1} flow with a fan-coil (*measured with a gas-counter made by RITTER, sn. 11456*). Each instrument samples from the tube with its own pump through a 0.25 inch Teflon line and a 5 µm pore size 47 mm diameter Teflon filter (to eliminate particles from the sampled air). See also Fig. 16.

More details about the mobile lab and instruments (where exactly they were measuring and when) can be found in sections below.

SO_2: UV Fluorescent SO_2 Analyser

Thermo 43iTLE (S/N 1021443379): 01.01-31.12.2017, Provisional site, mobile lab.

At first, the air flow is scrubbed to eliminate aromatic hydrocarbons. The sample is then directed to a chamber where it is irradiated at 214 nm (UV), a wavelength where SO_2 molecules absorb. The fluorescence signal emitted by the excited SO_2 molecules going back to the ground state is filtered between 300 and 400 nm (specific of SO_2) and amplified by a photomultiplier tube. A microprocessor receives the electrical zero and fluorescence reaction intensity signals and calculates SO_2 based on a linear calibration curve.

Calibration was performed with a certified SO_2 standard at a known concentration in air (44 ppb, Air Liquide). Zero check was done, using a zero air gas cylinder from Air Liquide, Alphagaz 1, CnHm < 0.5 ppm).

The specificity of the trace level Thermo instrument (TEI 43i-TLE) is that it uses a pulsed lamp. The 43i-TLE's detection limit is 0.05 ppb (about 0.13 µg m^{-3}) over 300 second averaging time, according to the technical specifications.

For more details about the instruments, manuals are available at \\ies.jrc.it\H02\lLargefacilities\ABC-IS\Quality_management\Manuals

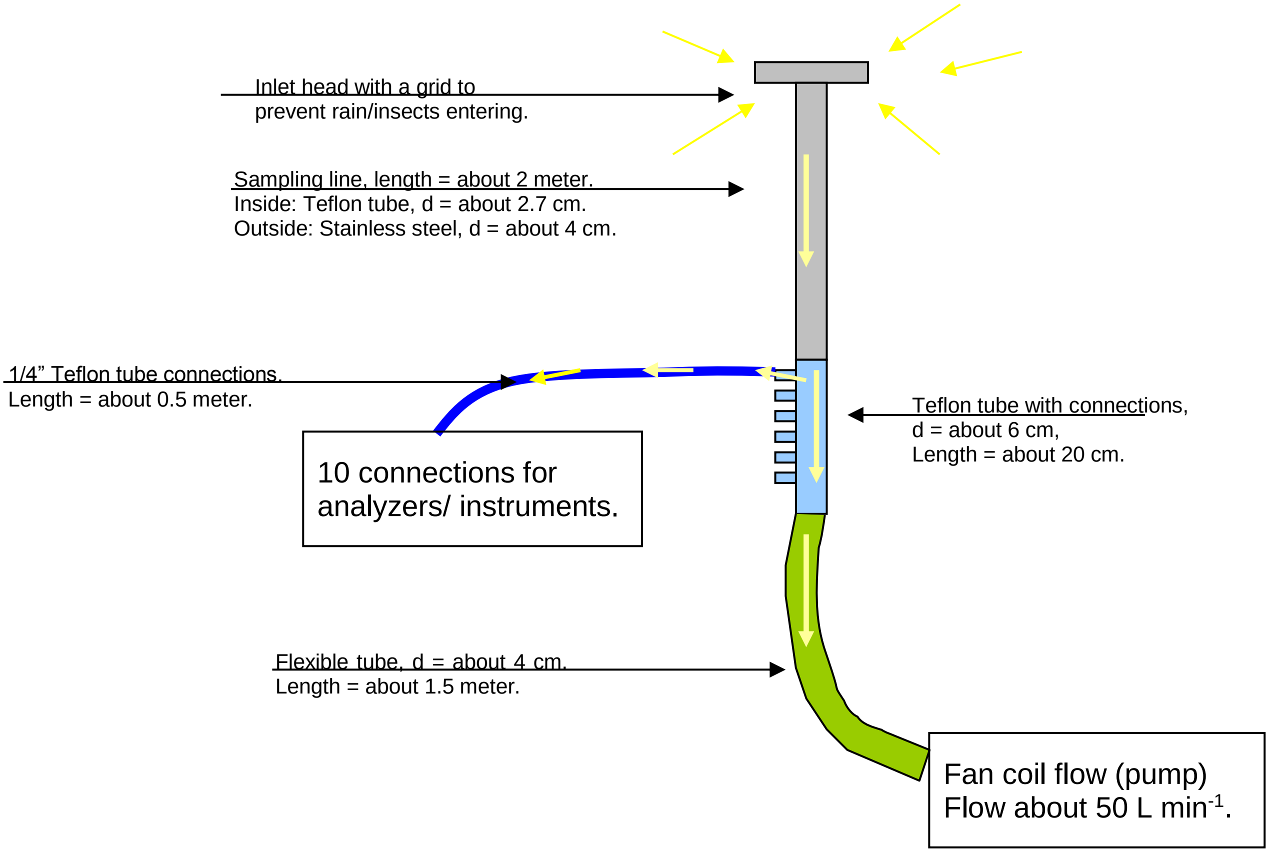

Fig. 16. Sampling inlet system for the gaseous air pollutant at the mobile lab. Inlet for the measurements is about 3.5 m above ground

NO + NO_X: Chemiluminescent Nitrogen Oxides Analyser (NO_2=NO_x-NO)

Thermo 42iTL (S/N 936539473): 01.01-31.12.2017: Provisional site, mobile lab.

This nitrogen oxide analyser is based on the principle that nitric oxide (NO) and ozone react to produce excited NO_2 molecules, which emit infrared photons when going back to lower energy states:

$$NO + O_3 \rightarrow [NO_2]^* + O_2 \rightarrow NO_2 + O_2 + hv$$

A stream of purified air (dried with a Nafion Dryer for 42iTL) passing through a silent discharge ozonator generates the ozone concentration needed for the chemiluminescent reaction. The specific luminescence signal intensity is therefore proportional to the NO concentration. A photomultiplier tube amplifies this signal.

NO_2 is detected as NO after reduction in a Mo converter heated at about 325 °C.

The ambient air sample is drawn into the analyser, flows through a capillary, and then to a valve, which routes the sample either straight to the reaction chamber (NO detection), or through the converter and then to the reaction chamber (NO_X detection). The calculated NO and NO_X concentrations are stored and used to calculate NO_2 concentrations ($NO_2 = NO_x - NO$), assuming that only NO_2 is reduced in the Mo converter.

Calibration was performed using a zero air gas cylinder (Air Liquide, Alphagaz 1, CnHm<0.5 ppm) and a NO span gas (85 ppb, Air Liquide). Calibration with a span gas was performed with a certified NO standard at a known concentration in N_2.

For more details about the instruments, the manuals are available on \\ies.jrc.it\H02\LargeFacilities\ABC-IS\Quality_management\Manuals

O_3: UV Photometric Ambient Analyser

Thermo 49C (S/N 0503110398): 01.01-31.12.2017: Provisional site, mobile lab.

The UV photometer determines ozone concentrations by measuring the absorption of O_3 molecules at a wavelength of 254 nm (UV light) in the absorption cell, followed by the use of Beer-Lambert law. The concentration of ozone is related to the magnitude of the absorption. The reference gas, generated by scrubbing ambient air, passes into one of the two absorption cells to establish a zero light intensity reading, I_0. Then the sample passes through the other absorption cell to establish a sample light intensity reading, I. This cycle is reproduced with inverted cells. The average ratio $R=I/I_0$ between 4 consecutive readings is directly related to the ozone concentration in the air sample through the Beer-Lambert law. Calibration is performed using externally generated zero air and external span gas. Zero air is taken from a gas cylinder (Air Liquide, Alphagaz 1, CnHm < 0.5 ppm). Span gas normally in the range 50 - 100 ppb is generated by a TEI 49C-PS transportable primary standard ozone generator (S/N 0503110396) calibrated/check by ERLAP (European Reference Laboratory of Air Pollution). A Nafion Dryer system is connected to the O_3 instrument.

For more details about the instruments, the manual is available on \\ies.jrc.it\H02\LargeFacilities\ABC-IS\Quality_management\Manuals

CO: Non-Dispersive Infrared Absorption CO Analyser

Horiba AMPA-370 (S/N WYHEOKSN) from 01.01 to 31.12.2017: Provisional site, mobile lab.

In 2017, carbon monoxide (CO) has been continuously monitored using a commercial Horiba AMPA-370 CO monitor based on the principle of non-dispersive infrared absorption (NDIR). The Horiba APMA-370 uses solenoid valve cross flow modulation applying the same air for both the sample and the reference, instead of the conventional technique to apply an optical chopper to obtain modulation signals. With this method the reference air is generated by passing the sample air over a heated oxidation catalyst to selectively remove CO which is then directly compared to the signal of the untreated sample air at a 1 Hz frequency. The result is a very low zero-drift and stable signal over long periods of time.

To reduce the interference from water vapour to about 1% the sample air was dried to a constant low relative humidity level of around 30% applying a Nafion dryer (Permapure MD-070-24P) in the inlet stream. The detection limit of the Horiba AMPA-370 is ~20 ppbv for a one minute sampling interval. The overall measurement uncertainty is estimated to be ± 7%.

For more details about the instrument, see the manual available from \\ies.jrc.it\H02\LargeFacilities\ABC-IS\Quality_management\Manuals

In 2017, the gas phase monitors were calibrated eleven times with suitable span gas cylinders and zero air (see text for more details). Sampling flow rates are as follow:

Compounds	Flow rates (L min^{-1})
SO_2	0.5
NO, NO_x	1.0/1.3
O_3	0.7
CO	1.5

Atmospheric Particles

Sampling Conditions

Since 2008, all instruments for the physical characterisation of aerosols (Multi-Angle Absorption Photometer, Aethalometer, Nephelometer, Aerodynamic Particle Sizer, Differential Mobility Particle Sizer) sample isokinetically from an Aluminium inlet pipe (diameter = 15 cm, length of horizontal part ~280 cm and vertical part ~220 cm) described in Jensen et al., 2010. The Tapered Element Oscillating Micro-balances (FDMS-TEOMs) used their own inlet systems. The MAAP sampled from the main inlet through Nafion dryers at a flow rate of 480 L hr^{-1} from Nov. 2016.

The size dependent particle losses along the pipe radius were determined by measuring the ambient aerosol size distribution with two DMPS at the sampling points P0 (close to the inlet) and P2 (close to the ned of the pipe) for different radial positions relative to the tube centre (0, 40 and 52 mm) at P2 (Gruening et al., 2009). Data show a small loss of particles towards the rim of the tube can be observed, but it stays below 15 %. The bigger deviation for particles smaller than 20 nm is again a result of very small particle number concentrations in this diameter range and thus rather big counting errors.

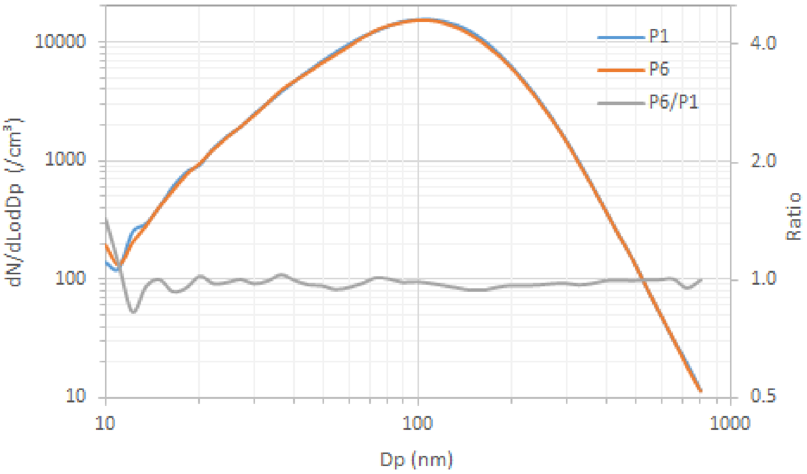

Fig. 17: particle number size distribution observed at both ends of the horizontal part of the aerosol manifold (Dec. 2017).

Particle losses in the aerosol manifold installed at the new Atmospheric Observatory have been measured using two inter-calibrated DMPS sampling close to the inlet (P1) and close to the outlet (P6) of the horizontal part of the manifold (Fig. 17). Losses at P6 compared to P1 were < 6% for all particle sizes between 20 and 800 nm (average 2%),which indicates no significant biases for the measurement of particle light absorption and scattering coefficient in the vicinity of P6.

PM_{10} Mass Concentration: Tapered Element Oscillating Mass balance (TEOM), Series 1400a

Thermo FDMS – TEOM (S/N 140AB233870012 & 140AB253620409)

The Series 1400a TEOM® monitor incorporates an inertial balance patented by Rupprecht & Patashnick, now Thermo Scientific. It measures the mass collected on an exchangeable filter cartridge by monitoring the frequency changes of a tapered element. The sample flow passes through the filter, where particulate matter is collected, and then continues through the hollow tapered element on its way to an electronic flow control system and vacuum pump. As more mass collects on the exchangeable filter, the tube's natural frequency of oscillation decreases. A *direct* relationship exists between the tube's change in frequency and mass on the filter. The TEOM mass transducer does not require recalibration because it is designed and constructed from non-fatiguing materials. However, calibration was verified on Dec. 9th, 2016 and Sept. 22nd, 2017 using a filter of known mass.

The instrument set-up includes a Sampling Equilibration System (SES) that allows a water strip-out without sample warm up by means of Nafion Dryers. In this way the air flow RH is reduced to < 30%, when TEOM® operates at 30°C only. The Filter Dynamic Measurement System (FDMS) is based on measuring changes of the TEOM filter mass when sampling alternatively ambient and filtered air. The changes in the TEOM filter mass while sampling filtered air is attributed to sampling (positive or negative) artefacts, and is used to correct changes in the TEOM filter mass observed while sampling ambient air.

Particle Number Size Distribution: Differential Mobility Particle Sizer (DMPS)

DMPS "B, DMA serial no. 158", CPC TSI 3772 (S/N 70847419 and 3772133103), neutraliser ^{85}Kr 10 mCi (2007)

The Differential Mobility Particle Sizer consists of a custom-made medium size (inner diameter 50 mm, outer diameter 67 mm and length 280 mm) Vienna-type Differential Mobility Analyser (DMA) and a Condensation Particle Counter (CPC), TSI 3772. Its setup follows the ACTRIS specifications for DMPS systems.

DMAs use the fact that electrically charged particles move in an electric field according to their electrical mobility. Electrical mobility depends mainly on particle size and electrical charge. Atmospheric particles are brought in the bipolar charge equilibrium in the bipolar diffusion charger (Eckert & Ziegler neutraliser with 370 MBq): a radioactive source (^{85}Kr) ionises the surrounding atmosphere into positive and negative ions. Particles carrying a high charge can discharge by capturing ions of opposite polarity. After a very short time, particles reach a charged equilibrium such that the aerosol carries the bipolar Fuchs-Boltzman charge distribution. A computer programme sets stepwise the voltage between the 2 DMA's electrodes (from 10 to 11500 V). Negatively charged particles are so selected according to their mobility. After a certain waiting time, the CPC measures the number concentration for each mobility bin. The result is a particle mobility distribution. The number size distribution is calculated from the mobility distribution by an inversion routine (from Stratmann and Wiedensohler, 1996) based on the bipolar charge distribution and the size dependent DMA transfer function. The DMPS measures aerosol particles in the range 10 - 800 nm with a 12 minute cycle. It records data using 45 size channels for high-resolution size information. This submicrometer particle sizer is capable of measuring concentrations in the range from 1 to 2.4 x 10^6 particles cm^{-3}. Instrumental parameters that are necessary for data evaluation such as flow rates, relative humidity, ambient pressure and temperature are measured and saved as well.

The CPC detection efficiency curve and the particle diffusion losses in the system are taken into account at the data processing stage.

Accessories include:

- FUG High voltage cassette power supplies Series HCN7E – 12500 Volts.

- Rotary vacuum pump vane-type (sampling aerosol at 1 LPM)
- Controlled blower (circulating dry sheath air)
- Nafion dryers for the sheath and sample air streams, implemented since October 2009.
- Mass flow meter and pressure transducer (to measure sheath air and sample flows).

Particle Number Size Distribution: Aerodynamic Particle Sizer (APS)

APS TSI 3321 (S/N 70535014 & S/N 1243)

The APS 3321 is a time-of-flight spectrometer that measures the velocity of particles in an accelerating air flow through a nozzle.

Ambient air is sampled at 1 L min^{-1}, sheath air (from the room) at 4 L min^{-1}. In the instrument, particles are confined to the centre-line of an accelerating flow by sheath air. They then pass through two broadly focused laser beams, scattering light as they do so. Side-scattered light is collected by an elliptical mirror that focuses the collected light onto a solid-state photodetector, which converts the light pulses to electrical pulses. By electronically timing the gap between the peaks of the pulses, the velocity can be calculated for each individual particle.

Velocity information is stored in 1024 time-of-flight bins. Using a polystyrene latex (PSL) sphere calibration, which is stored in non-volatile memory, the APS Model 3321 converts each time-of-flight measurement to an aerodynamic particle diameter. For convenience, this particle size is binned into 52 channels (on a logarithmic scale).

The particle range spanned by the APS is 0.5 - 20 μm in both aerodynamic size and light-scattering signal. Particles are also detected in the 0.3 to 0.5 μm range using light-scattering alone, and are binned together in one channel. The APS is also capable of storing correlated light-scattering-signal. *dN/dLogDp* data are averaged over 10 min.

Particle Scattering and Backscattering Coefficient

Integrating Nephelometer TSI 3563 (S/N 1081 & S/N 142101)

The integrating nephelometer is a high-sensitivity device capable of measuring the scattering properties of aerosol particles. The nephelometer measures the light scattered by the aerosol and then subtracts the light scattered by the walls of the measurement chamber, light scattered by the gas, and electronic noise inherent in the detectors.

Dried ambient air (since 18.11.2009) was sampled at 5.1 L min^{-1} (12 L min^{-1} from 14 Dec. 2016) from a PM10 inlet. .

The three-colour detection version of TSI nephelometer detects scattered light intensity at three wavelengths (450, 550, and 700 nm). Normally the scattered light is integrated over an angular range of 7–170° from the forward direction, but with the addition of the backscatter shutter feature to the Nephelometer, this range can be adjusted to either 7–170° or 90–170° to give total scatter and backscatter signals. A 75 Watt quartz-halogen white lamp, with a built-in elliptical reflector, provides illumination for the aerosol. The reflector focuses the light onto one end of an optical pipe where the light is carried into the internal cavity of the instrument. The optical pipe is used to thermally isolate the lamp from the sensing volume. The output end of the optical light pipe is an opal glass diffuser that acts as a *quasi*-cosine (Lambertian) light source. Within the measuring volume, the first aperture on the detection side of the instrument limits the light integration to angles greater than 7°, measured from the horizontal at the opal glass. On the other side, a shadow plate limits the light to angles less than 170°. The measurement volume is defined by the intersection of this light with a viewing volume cone defined by the second and fourth aperture plates on the detection side of the instrument. The fourth aperture plate incorporates a lens to collimate the light scattered by aerosol particles so that it can be split into separate wavelengths. The nephelometer uses a reference chopper to calibrate scattered signals. The chopper makes a full rotation 23 times per second. The chopper consists of three separate areas labelled "signal", "dark", and "calibrate". The "signal" section simply allows all light to pass through unaltered. The "dark" section is a very black background that blocks all light. This section provides a measurement of the photomultiplier tube (PMT) background noise. The third section is directly illuminated to provide a measure of lamp stability over time. To reduce the lamp intensity to a level that will not saturate the photomultiplier tubes, the "calibrate" section incorporates a neutral density filter that blocks approximately 99.9 % of the incident light. To subtract the light scattered by the gas portion of the aerosol, a high-efficiency particulate air (HEPA) filter is switched in line with the inlet for 300 s every day at 08:00 UTC. This allows compensation for changes in the background scattering of the nephelometer, and in gas composition that will affect Rayleigh scattering of air molecules with time. When the HEPA filter is not in line with the inlet, a small amount of filtered air leaks through the light trap to keep the apertures and light trap free of particles. A smaller HEPA filter allows a small amount of clean air to leak into the sensor end of the chamber between the lens and second aperture. This keeps the lens clean and confines the aerosol light scatter to the measurement volume only.

Nephelometer data are corrected for angular non-idealities and truncation errors according to Anderson and Ogren, 1998. A Nafion dryer has been installed (18.11.2009) at the inlet to measure light scattering by dry aerosols. Internal RH generally ranges from 0 to 40 % (average 31%, 70th percentile 40% in 2017). At 40% RH, aerosol scattering would be on average increased by about 15% compared to 0% RH in Ispra (Adam et al., 2012). However, aerosol particle scattering coefficients presented in this report are **not** corrected for RH effects, except when specified.

Particle Absorption Coefficient

Aethalometer Magee AE-31 ('A' S/N 408:0303 & 'B' S/N 740:0609)

The principle of the Aethalometer is to measure the attenuation of a beam of light transmitted through a filter, while the filter is continuously collecting an aerosol sample. Suction is provided by an internally-mounted pump. Attenuation measurements are made at successive regular intervals of a time-base period. The objectives of the Aethalometer hardware and software systems are as follows:

(a) to collect the aerosol sample with as few losses as possible on a suitable filter material;

(b) to measure the optical attenuation of the collected aerosol deposit as accurately as possible;

(c) to calculate the rate of increase of the equivalent black carbon (EBC) component of the aerosol deposit and to interpret this as an EBC concentration in the air stream;

(d) to display and record the data, and to perform necessary instrument control and diagnostic functions.

The optical attenuation of the aerosol deposit on the filter is measured by detecting the intensity of light transmitted through the spot on the filter. In the AE-31, light sources emitting at different wavelengths (370, 470, 520, 590, 660, 880 and 950 nm) are also installed in the source assembly. The light shines through the lucite aerosol inlet onto the aerosol deposit spot on the filter. The filter rests on a stainless steel mesh grid, through which the pumping suction is applied. Light penetrating the diffuse mat of filter fibres can also pass through the spaces in the support mesh. This light is then detected by a photodiode placed directly underneath the filter support mesh. As the EBC content of the aerosol spot increases, the amount of light detected by the photodiode will diminish.

For better accuracy, additional measurements are necessary: the amount of light penetrating the combination of filter and support mesh is relatively small, and a correction is needed for the 'dark response signal' of the overall system. This is the electronics' output when the lamps are off: typically, it may be a fraction of a percent of the response when the lamps are on. To eliminate the effect of the dark response, we take 'zero' readings of the system response with the lamps turned off, and subtract this 'zero' level from the response when the lamps are on.

The other measurement necessary is a 'reference beam' measurement to correct for any small changes in the light intensity output of the source. This is achieved by a second photodiode placed under a different portion of the filter that is not collecting the aerosol, on the left-hand side where the fresh tape enters. This area is illuminated by the same lamps. If the light intensity output of the lamps changes slightly, the response of this detector is used to correct mathematically the 'sensing' signal. The reference signal is also corrected for the dark response 'zero' as described above.

The algorithm in the software (see below) can account for changes in the lamp intensity output by always using the ratio quantity [Sensing]/[Reference]. As the filter deposit accumulates EBC, this ratio will diminish.

In practice, the algorithm can account for lamp intensity fluctuations to first order, but we find a residual effect when operating at the highest sensitivities. To minimise this effect and to realise the full potential of the instrument, it is desirable for the lamps' light output intensity to remain as constant as possible from one cycle to the next, even though the lamps are turned on and off again. The software monitors the repeatability of the reference signal, and issues a warning message if the fluctuations are considered unacceptable. When operating properly, the system can achieve a reference beam repeatability of better than 1 part in 10000 from one cycle to the next. The electronics circuit board converts the optical signals directly from small photocurrents into digital data, and passes it to the computer for calculation. A mass flow meter monitors the sampled air flow rate. These data and the result of the EBC calculation are written to disk and displayed on the front panel of the instrument.

Aethalometer data can be corrected for the shadowing effect and for multiple-scattering in the filter to derive the aerosol absorption coefficient (Arnott et al., 2005) with a correction factor C = 3.60, 3.65, and 3.95 for 470, 520 and 660 nm, respectively. Note that ACTRIS provisionally recommends the use of a constant conversion factor C_0 = 3.5 for all wavelengths (Mueller, 2015).

Multi Angle Absorption Photometer (S/N 4254515)

A Multi Angle Absorption Photometer (MAAP) model 5012 from Thermo Scientific was installed at the EMEP station in September 2008 and provides equivalent black carbon concentrations (EBC) and aerosol absorption (α) data at a nominal wavelength of 670 nm. Note that during a EUSAAR workshop (www.eusaar.org) in 2007 it has been observed that the operating wavelength of all MAAP instruments present at that workshop was 637 nm with a line width of 18 nm (full width at half maximum). The operating wavelength of this MAAP instrument has not been measured yet, therefore it is assumed to work at 670 nm as stated by the manufacturer.

The MAAP is based on the principle of aerosol-related light absorption and the corresponding atmospheric equivalent black carbon (EBC) mass concentration. Model 5012 uses a multi angle absorption photometer to analyse the modification of scattering and absorption in the forward and backward hemisphere of a glass-fibre filter caused by deposited particles. The internal data inversion algorithm of the instrument is based on a radiation transfer model and explicitly takes into account multiple scattering processes inside the deposited aerosol and between the aerosol layer and the filter matrix (see Petzold et al., 2004).

The sample air is drawn into the MAAP and aerosols are deposited onto the glass fibre filter tape. The filter tape accumulates the aerosol sample until a threshold value is reached, then the tape is automatically advanced. Inside the detection chamber (Fig. 18), a 670-nanometer light emitting diode is aimed towards the deposited aerosol and filter tape matrix. The light transmitted into the forward hemisphere and reflected into the back hemisphere is measured by a total of five photo-detectors. During sample accumulation, the light intensities at the different photo-detectors change compared to a clean filter spot. The reduction of light transmission, change in reflection intensities under different angles and the air sample volume are continuously measured during the sample period. With these data and using its proprietary radiation transfer scheme, the MAAP calculates the equivalent black carbon concentration (EBC) as the instruments measurement result.

Using the specific absorption cross section $\sigma_{\square BC}$ = 6.6 m^2/g of equivalent black carbon at the operation wavelength of 670 nm, the aerosol absorption (α) at that wavelength can be readily calculated as:

$$\alpha = EBC \times \sigma_{BC} \qquad \textit{Eq. 1}$$

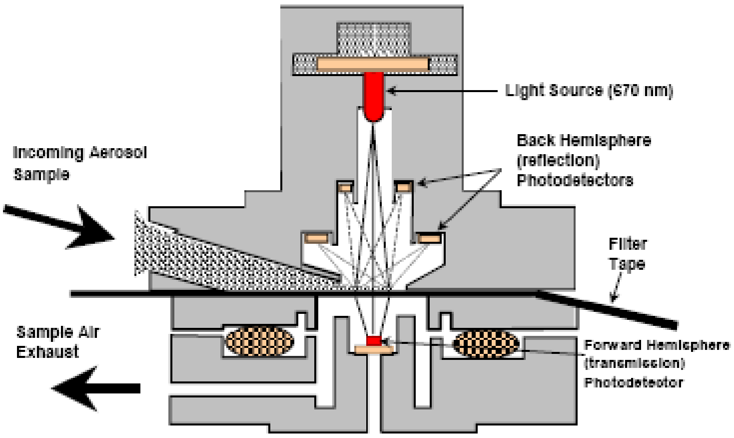

Fig. 18: MAAP detection chamber (sketch from the manual of the instrument).

Range-Resolved Aerosol Light Backscattering and Extinction

Raymetrics Aerosol Raman Lidar (S/N 400-1-12, QUANTEL Brilliant B Laser and cooler S/N 120059004 and S/N 120034401, LICEL Transient Recorder & Hi Voltage Supply S/N BS3245 and BS3245b, industrial PC S/N TPL-1571H-D3AE)

LiDAR measurements are based on the time-resolved detection of the backscattered signal of a short laser pulse that is sent into the atmosphere (for an introduction see Weitkamp, 2005). Using the speed of light, time is converted to the altitude where the backscattering takes place. Using the particle-free range of the atmosphere for calibration (where Rayleigh scattering from the air molecules is known), aerosol backscattering and extinction coefficients as well as aerosol optical thickness can be derived using the LIDAR equation. The received power P of the detector is therein given as a function of distance and wavelength by *Eq. 2*:

$$P(R,\lambda) = P_0 \, {}^{c\tau}\!/_{2} \, A\eta \frac{O(R)}{R^2} \beta(R,\lambda) \exp\left(-2\int_0^R \alpha(r,\lambda)dr\right)$$

Eq. 2: P_0: Power of the laser pulse, c: speed of light, τ: laser pulse length, A: area of the telescope, η: system efficiency, R: distance, O: overlap function (between laser beam and receiving optics field of view), λ: wavelength, β: backscatter coefficient, α: absorption coefficient

The instrument itself was installed on October 8-11th, 2012, and accessories (including radar) on December 11-13, 2012. This lidar emits at 3 wavelengths from IR to UV (1064 nm, polarised-532 nm, 355 nm) and records at 5 wavelengths, namely the emission wavelengths and two vibrational Raman channels at 387 and 607 nm. Measurements at 1064 nm, 532 nm, and 355 nm provide aerosol backscatter profiles, while measurements at 687 nm, and 387 nm provide aerosol extinction profiles during the dark hours of the day. The depolarisation of the 532 nm light beam is also measured. After the re-installation of the laser in Nov. 2015, the instrument was run in 2017 with a 5 min integration time during time slots covering noon (Mondays) and sunset (Mondays and Thursdays) according to the ACTRIS schedule, and during Calipso overpasses (about once every 8 days at 01:40 or 12:30). Data are inverted using the online Single Calculus Chain developed by EARLINET, after pre-processing to cope with new requirements for submitting data to the ACTRIS-EARLINET data bank.

4.2.2.2 Sampling and off-line analyses

Particulate Matter

Particle sampler: Partisol 2025 S/N 2025B22156220203
Micro-balance: MC5 S/N 50208287
Ion Chromatographs: ICS 2000 S/N 07101404 and 07101405 and DX-120 (Jan.-Feb.)
OC-EC analyser: Sunset Lab OCEC analyser S/N 173.

$PM_{2.5}$ was continuously sampled at 16.7 L min^{-1} on quartz fibre filters with a Partisol sampler equipped with a carbon honeycomb denuder. The sampled area is 42 mm Ø. Filters were from PALL Life Sciences (type TISSUEQUARTZ 2500QAT-UP). Filter changes occurred daily at 08:00 UTC.

Filters were weighed at 20 % RH before and after sampling with a microbalance Sartorius MC5 placed in a controlled (dried or moisture added and scrubbed) atmosphere glove box. They were stored at 4 °C until analysis.

Main ions (Cl^-, NO_3^-, SO_4^{2-}, $C_2O_4^{2-}$, Na^+, NH_4^+, K^+, Mg^{2+}, Ca^{2+}) were analysed by ion chromatography with electrochemical eluent suppression (ICS2000) after extraction of the soluble species from an aliquot of 16 mm Ø in 10 ml 18.2 MOhm cm resistivity water (Millipore mQ).

Organic and elemental carbon (OC+EC) were analysed using a Sunset Dual-optical Lab Thermal-Optical Carbon Aerosol Analyser (S/N 173-5). $PM_{2.5}$ samples were analysed using the EUSAAR-2 thermal protocol according to EN 16909. It has been developed to minimise biases inherent to thermo-optical analysis of OC and EC (Cavalli et al., 2010), and is described in Table 3 below.

No measurement of PM_{10} or PM_{coarse} was performed in 2017.

Table 3: Parameters of the EUSAAR-2 analytical protocol

Fraction Name	Plateau Temperature (°C)	Duration (s)	Carrier Gas
OC 1	200	120	He 100%
OC 2	300	150	He 100%
OC 3	450	180	He 100%
OC 4	650	180	He 100%
cool down		30	He 100%
EC1	500	120	He:O_2 98:2
EC2	550	120	He:O_2 98:2
EC3	700	70	He:O_2 98:2
EC4	850	110	He:O_2 98:2

Wet-only deposition

Precipitation sampler: Eigenbrodt Model NSA 181/KS S/N 3313 and 3312
Conductimeter and pH-meter: Sartorius Professional Meter PP-50 S/N 16350322.
Ion Chromatographs: ICS 2000 S/N 07101404 and 07101405

For precipitation collection, two wet-only samplers were used that automatically collect the rainfall in a 1 L polyethylene container. The collection surface is 550 cm^2. 24-hr integrated precipitation samples (if any) are collected every day starting at 8:00 UTC. All collected precipitation samples were stored at 4 °C until analyses (ca. every 3 months).Analyses include the determinations of pH and conductivity at 25 °C and principal ion concentrations (Cl^-, NO_3^-, SO_4^{2-}, $C_2O_4^{2-}$, Na^+, NH_4^+, K^+, Mg^{2+}, Ca^{2+}) by ion chromatography with electrochemical eluent suppression.

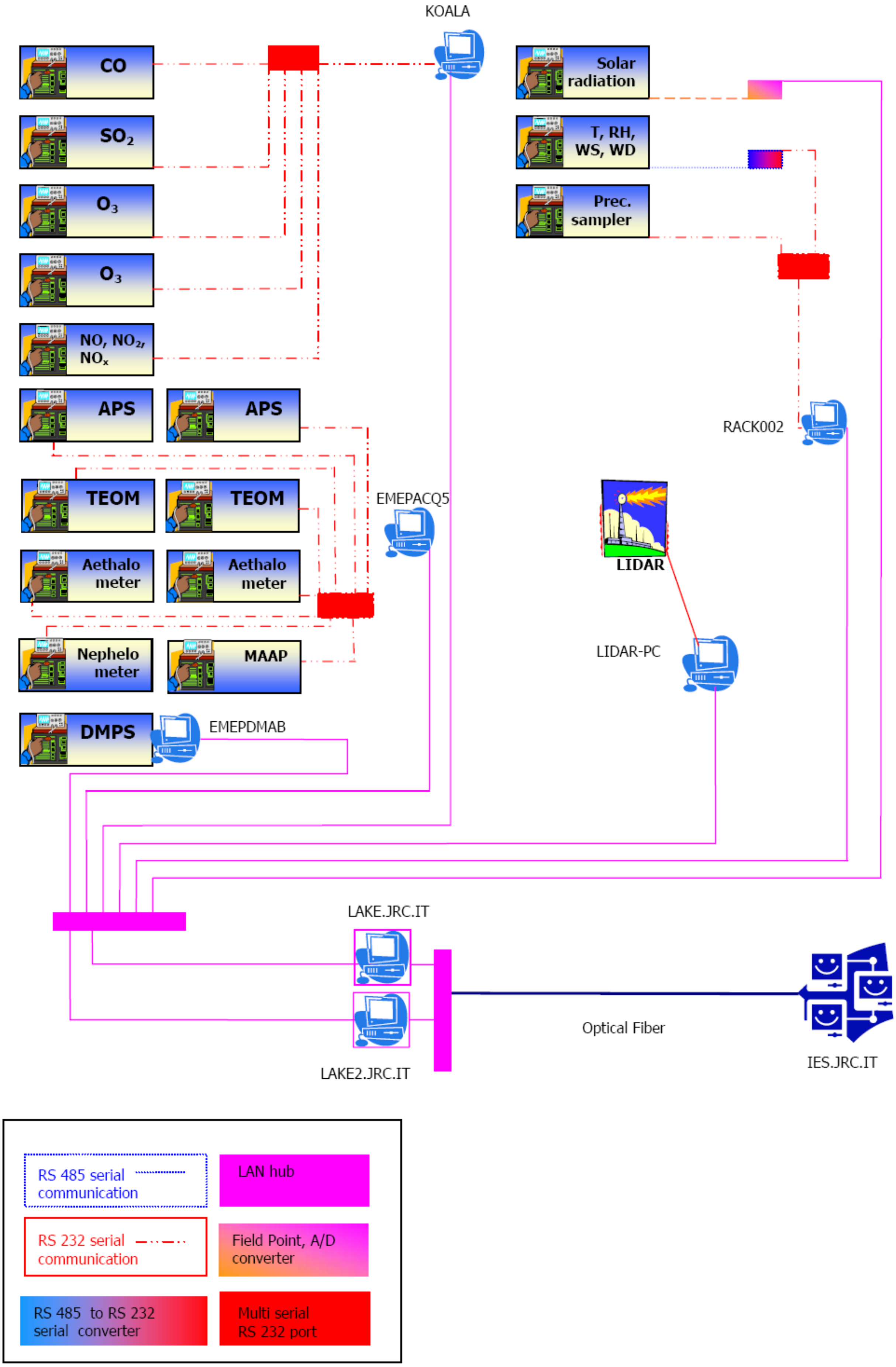

Fig. 19: Set-up of the EMEP- GAW station Data Acquisition System.

4.2.3 On-line data acquisition system/data management

The JRC EMEP-GAW station Data Acquisition System (DAS) is a specifically tailored set of hardware and software (developed by the Air and Climate unit, in collaboration with NOS Sistemi s.r.l), designed to operate instruments, acquire both analogue and digital output from instruments and store pre-processed measurement data into a database for further off-line evaluation. The DAS operated and controlled the instrumentation during 2017. No updates were implemented.

The software environment of the DAS is Labview 7.1 from National Instruments and the database engine for data storage is Microsoft SQL Server 2008.

The DAS is designed to continuously run the following tasks:

- Start of the data acquisition at a defined time (must be full hour);
- Choose the instruments that have to be handled;
- Define the database path where data will be stored (primary in the network, secondary local on the acquisition machine);
- Define the period (10 minutes currently used) for storing averaged data, this is the data acquisition cycle time;
- Obtain data (every 10 seconds currently set) for selected instruments within the data acquisition cycle:
  - For analogue instruments (i.e. the CMP11 Pyranometer until end of Nov. 2017), apply the calibration constants to translate the readings (voltages or currents) into analytical values;
  - Send commands to query instruments for data or keep listening the ports for instruments that have self-defined output timing;
  - Scan instruments outputs to pick out the necessary data;
- Calculate average values and standard deviations for the cycle period;
- Query instruments for diagnostic data (when available), once every 10 minutes;
- Store all data in a database
  - With a single timestamp for the gas analysers, FDMS-TEOM and Nephelometer
  - With the timestamp of their respective measurement for all other instruments.

The following instruments are managed with the DAS (Fig. 19), using three PCs (currently called Emepacq5, Koala and Rack002):

Emepacq5:

- Number size distribution for particles diameter >0.500 µm, APS
- On-line FDMS-TEOMs
- Aerosol light absorption, Aethalometer
- Aerosol light absorption, MAAP
- Aerosol light scattering, Nephelometer

Koala:

- Reactive gases: CO, SO2, NO, NO_2, NO_x, O_3

Rack002:

- Solar radiation
- Weather transmitter (temperature, pressure, relative humidity, wind speed and direction, precipitation)

- Precipitation data

The data acquired are stored in a Microsoft SQL Server 2008 database on the central database ***emep_db*** hosted on the pc **Lake2.jrc.it**. If the local network is not available, data are stored in a local database on the acquisition pc itself. Each pc also has software for the synchronisation of **emep_db** with **local db.**

The PC "**Lake.jrc.it**" connects the laboratory to the JRC network (*ies.jrc.it* domain) via optical lines. The schematic setup of the data acquisition system is shown in Fig. 19.

The acquisition time is locally synchronised for all PCs via a network time server running on lake and is kept at UTC, without adjustment for summer/winter time. Data are collected in a data base called ***emep_db*** that runs on "**Lake2.jrc.it**".

Lake is the user gateway for the Station user, to allow granted staff to remotely access the acquisition computers. This PC is also used to share information (life cycle sheets, lidar data) between IES domain and the Station network.

In the web site the projects to which ABC-IS contributes and contact persons can also be retrieved.

The station web site (http://abc-is.jrc.ec.europa.eu/, not optimised under Internet Explorer) runs over two machines. The first is the web server, **ccuprod2**, in the DMZ (demilitarised zone), where the web page code runs and is managed by the Air and Climate Unit IT staff. The development environment was Python and Ajax. The second computer, **emepimag.jrc.it,** in the JRC network, queries the database for data, generate plots and store plots in a folder in ccuprod2, to make them available to the internet. This second machine is managed by ABC-IS data management team and the software has been developed in C-sharp.

4.2.4 Data evaluation

The structured data evaluation system (EMEP_Main.m) with a graphic user interface (see Fig. 20) has been used with Matlab Release R2007b (www.mathworks.com) as the programming environment.

The data evaluation is now done with the "EMEP_Data_Handling L0 to L2" v. 1.9.8.8 - Nov 2017. The not evaluated 10 min data (flagged 3) is now exported to several excel sheets.

After a preliminary data analysis, these data are flagged according to the flags listed below. These files including flags are then imported into the database (level 1 data, 10 min corrected). Finally the hourly and the daily data averages are calculated taking into account the flagging.

0	Good data – used
1	Good data – not used
2	Calibration
3	Not evaluated
5	questionable
6	Local contamination
7	Erroneous data
9	No data

Only the evaluation of gas phase data has an automatic removal algorithm for outliers / spikes implemented: d_i = 10 minute average value at time i, std_i = standard deviation for the 10 minute average (both saved in the raw data)

if $std_i > 100 \cdot \overline{std}$ and $|d_i - d_{i\pm1}| > 10 \cdot \overline{std}$

$\Rightarrow d_i = 1/2\left(d_{i-1} + d_{i+1}\right)$ for d_{i-1} **and** d_{i+1} **no** outliers,

otherwise $d_i = missig\ data$.

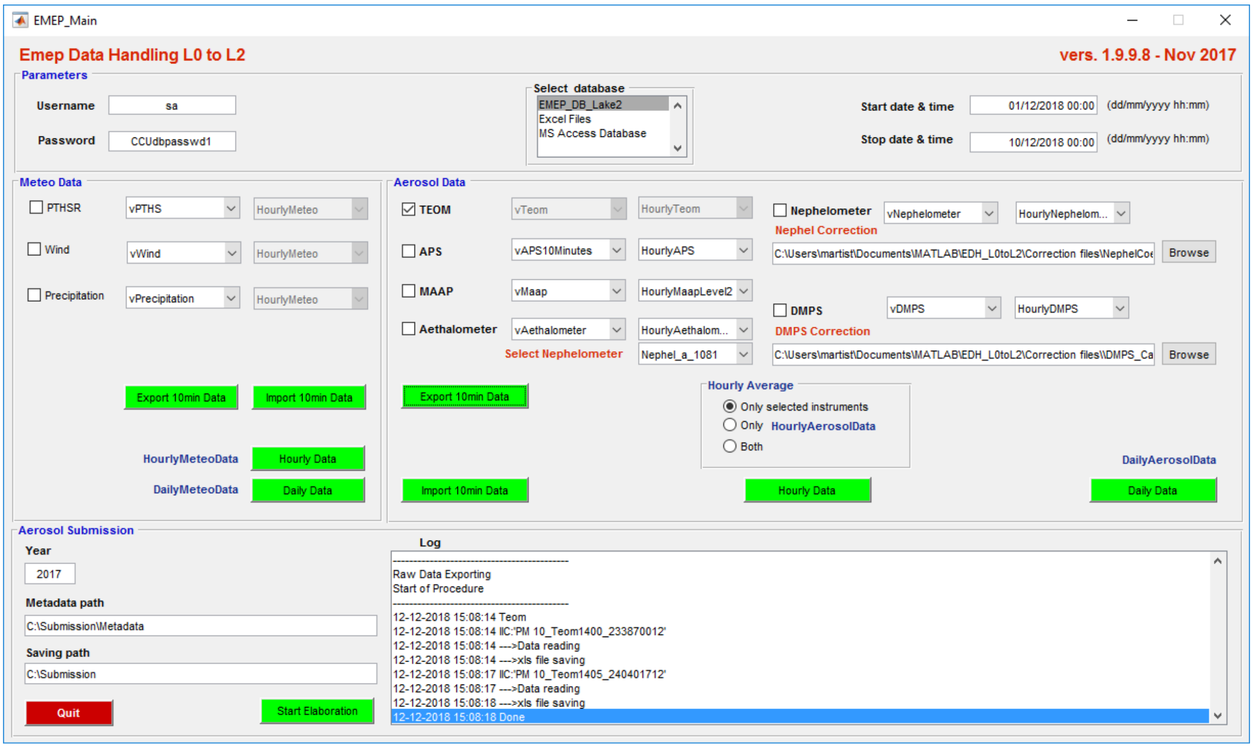
EMEP_Main

Emep Data Handling L0 to L2 vers. 1.9.9.8 - Nov 2017

Parameters

Username: sa
Password: CCUdbpasswd1
Select database: EMEP_DB_Lake2
Start date & time: 01/12/2018 00:00 (dd/mm/yyyy hh:mm)
Stop date & time: 10/12/2018 00:00 (dd/mm/yyyy hh:mm)

Meteo Data

☐ PTHSR vPTHS HourlyMeteo
☐ Wind vWind HourlyMeteo
☐ Precipitation vPrecipitation HourlyMeteo

Aerosol Data

☑ TEOM vTeom HourlyTeom
☐ APS vAPS10Minutes HourlyAPS
☐ MAAP vMaap HourlyMaapLevel2
☐ Aethalometer vAethalometer HourlyAethalom...
Select Nephelometer: Nephel_a_1081
☐ Nephelometer vNephelometer HourlyNephelom...
Nephel Correction: C:\Users\martist\Documents\MATLAB\EDH_L0toL2\Correction files\NephelCoe
☐ DMPS vDMPS HourlyDMPS
DMPS Correction: C:\Users\martist\Documents\MATLAB\EDH_L0toL2\Correction files\\DMPS_Ca

Hourly Average:
● Only selected instruments
○ Only HourlyAerosolData
○ Both

Aerosol Submission

Year: 2017
Metadata path: C:\Submission\Metadata
Saving path: C:\Submission

Log

```
---------------------------------------------
Raw Data Exporting
Start of Procedure
---------------------------------------------
12-12-2018 15:08:14 Teom
12-12-2018 15:08:14 IIC:'PM 10_Teom1400_233870012'
12-12-2018 15:08:14 --->Data reading
12-12-2018 15:08:14 --->xls file saving
12-12-2018 15:08:17 IIC:'PM 10_Teom1405_240401712'
12-12-2018 15:08:17 --->Data reading
12-12-2018 15:08:18 --->xls file saving
12-12-2018 15:08:18 Done
```

Fig. 20: Graphic user interface of the EMEP-GAW station data evaluation.

This algorithm corrects for single point outliers and removes double point outliers. All other situations are considered correct data. To check these data and to exclude outliers for all other measurements, a visual inspection of the 10 min data needs to be performed.

In addition, quick looks of evaluated data for selected time periods can be produced as well as printed timelines in the pdf-format for the evaluated data. All database connections are implemented via ODBC calls (Open DataBase Connectivity) to the corresponding Microsoft SQL server 2008.

Daily averages (8:00 < t ≤ 8:00 +1 day) of all variables and parameters stored in the hourly averages database can be calculated and are subsequently stored in a separate Microsoft SQL Server 2008 database.

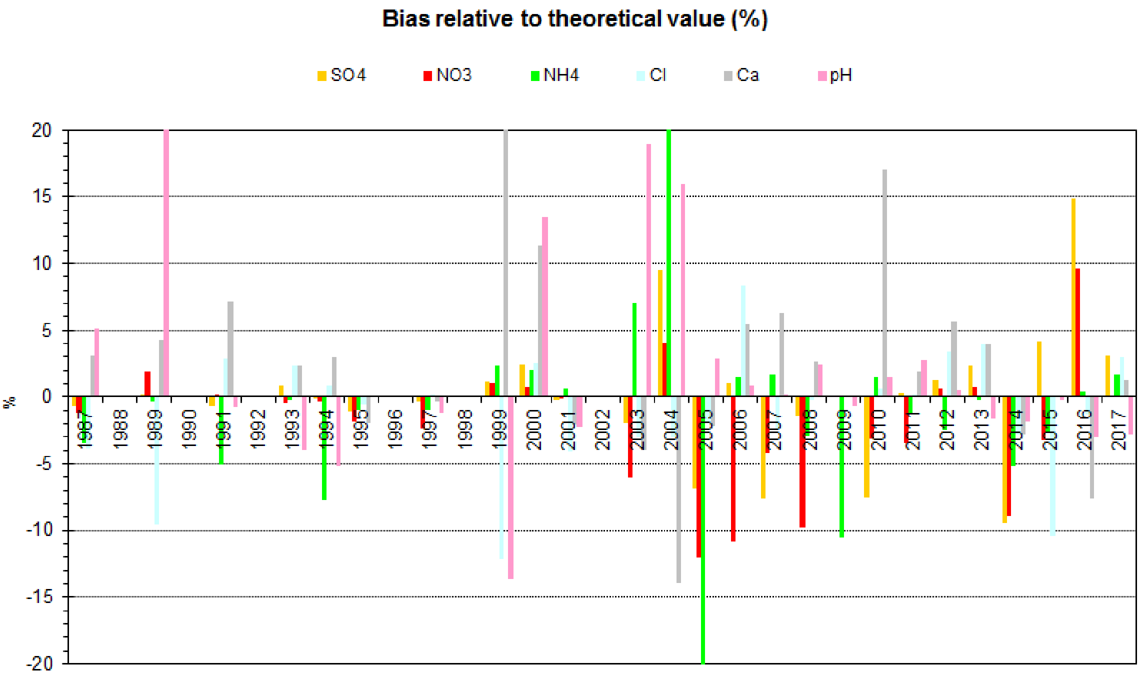

Fig. 21. EMEP inter-laboratory comparisons for rainwater analyses (1987-2017): JRC-Ispra results.

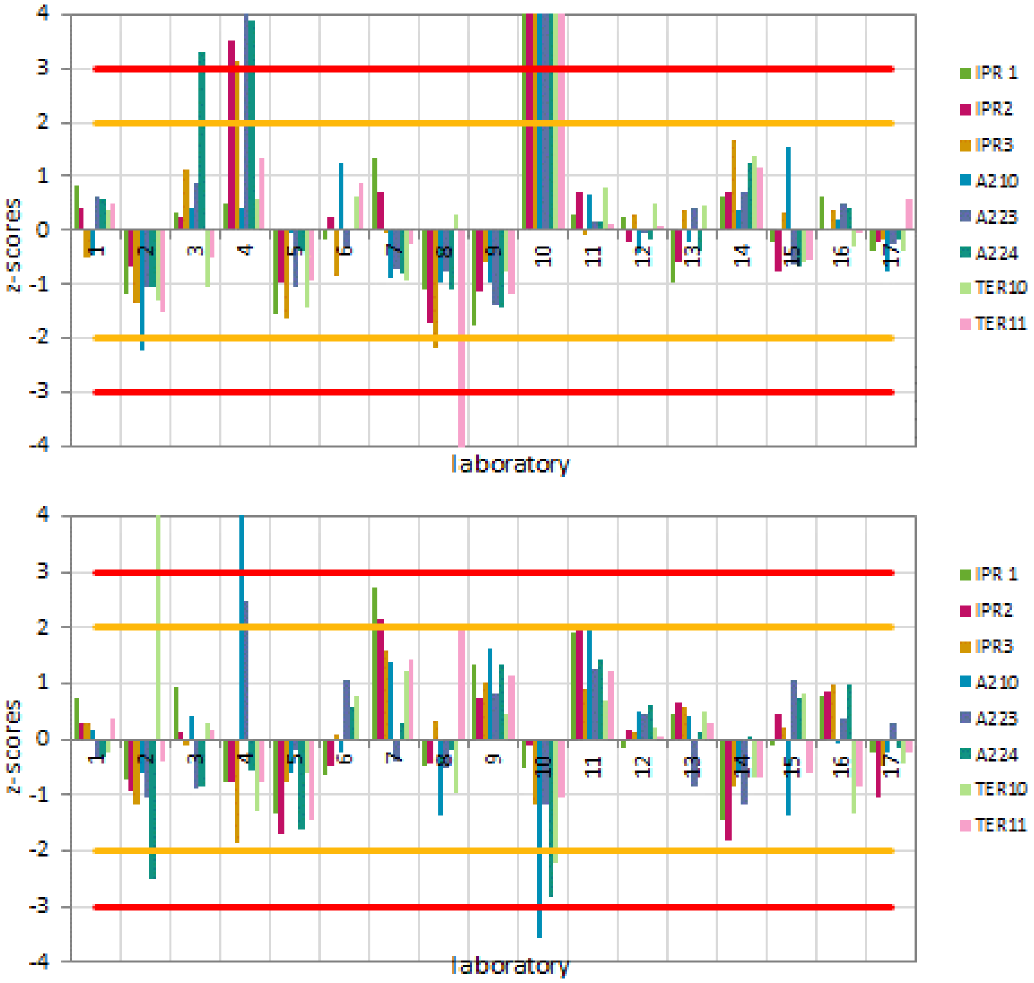

Fig. 22. JRC-Ispra instrument's (#17) performance for the determination of (top) total carbon (TC) and (bottom) elemental carbon (EC/TC ratio) during the ACTRIS inter-laboratory comparison 2017-1 (ACTRIS).

4.3 Quality assurance

At JRC level the quality system is based on the Total Quality Management philosophy, the implementation of which started at the Air and Climate Unit in December 1999. We have been working under ISO 9001 and ISO 14001 since 2010 (more information about our QMS system can also be found in the chapter "Quality management system").

Lacking personnel to specifically follow this business, the JRC-Ispra station for atmospheric research did not renew the accreditation for the monitoring of SO_2, NO, NO_2 and O_3 under EN 45001 obtained in 1999. However, measurements and standardised operating procedures are based on recommendations of the EMEP manual (1995, revised 1996; 2001; 2002; 2014), WMO/GAW 227, ISO and CEN standards. Moreover, the JRC-Ispra gas monitors and standards are checked by the European Reference Laboratory for Air Pollution (ERLAP) regularly. This includes annual preventive maintenance, linearity check and Gas Phase Titration (for NO_x).

For on-line aerosol measurements, ACTRIS Standard Operating Procedures and QA/QC requirements are followed. Those involve station audits, side by side instrument comparisons at the world calibration centre for aerosol physics (WCCAP) in Leipzig (DE), and specific QC measurements. The station was favourably audited by Dr. T. Tuch (WCCAP) on 22-24 March 2010 under the EUSAAR project (www.eusaar.net), as described in a specific report. JRC's integrating nephelometer (see report) and absorption spectrometers (see reports) successfully took part in side by side comparisons at the Wold Calibration Centre for Atmospheric Physics in Leipzig in Sept. 2017. The Differential Mobility Particle Sizer was successfully checked at the WCCAP in Jan 25-29th, 2016 (see report).

Ion analysis quality was checked through the 35th annual EMEP inter-laboratory comparison (Fig. 21). In this exercise, all ion measurements in the rain water synthetic samples provided by NILU passed the quality test. The data quality objective within EMEP is 10% accuracy or better for NO_3^- and SO_4^{2-} and 15% accuracy or better for other components for each sample. pH measurements were on average accurate but the deviation to the assigned value ranged between -0.17 and +0.25.

The inter-laboratory comparison for organic and elemental carbon analyses organised under the competitive project ACTRIS-2 in 2017 indicates no systematic bias for the determination of total carbon and elemental carbon compared to the robust average among the participants (Fig. 22).

Quality check measurements are reported at least once a year to the ACTRIS Lidar Calibration Centre, which produces a detailed report on the instrument performance.

Data quality for all measurements is also checked whenever possible through comparison among different instruments, mass closure (for PM) and ion balance (for precipitation) exercises (see specific sections).

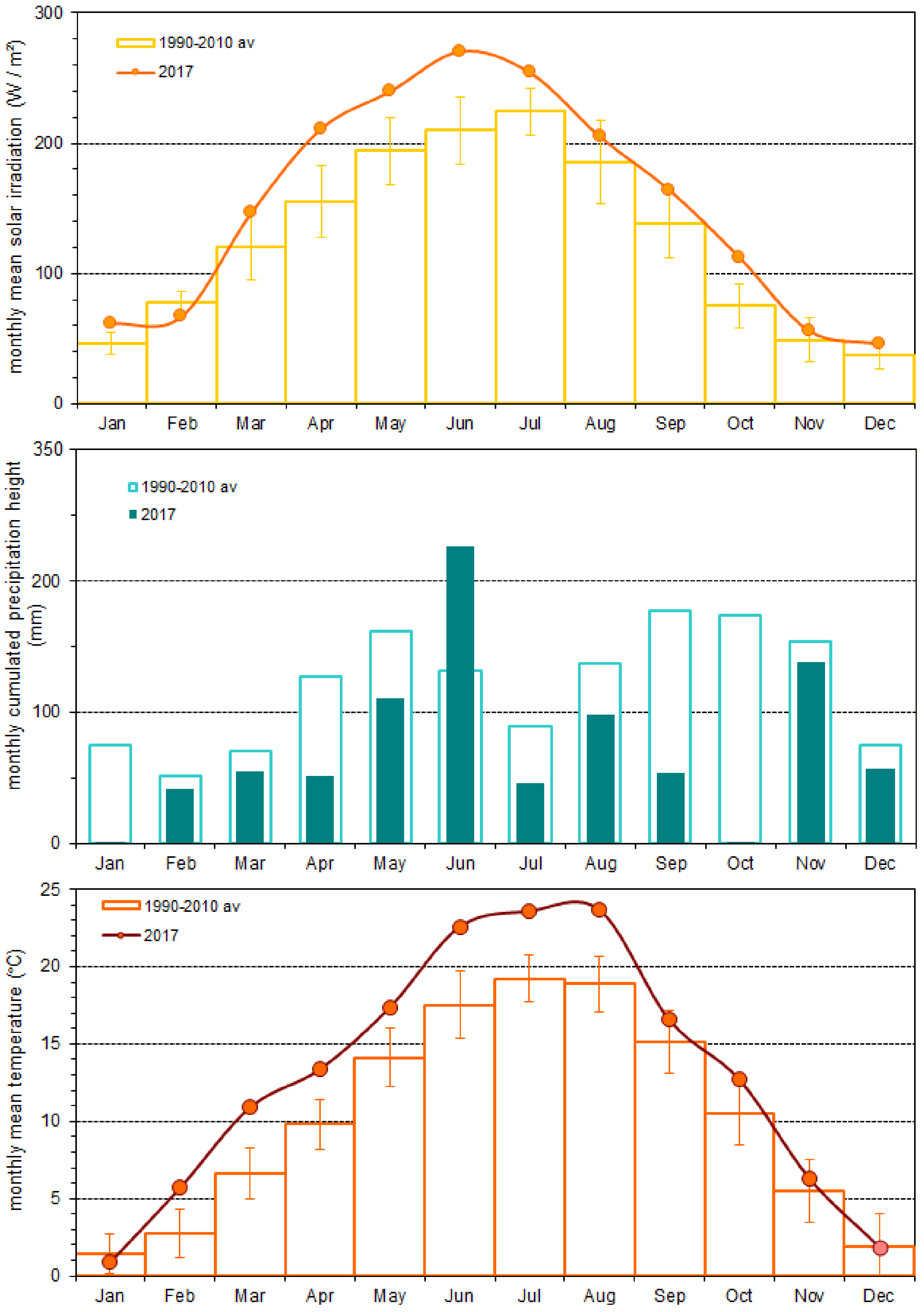

Fig. 23. Solar global irradiation, precipitation amount, and temperature monthly values observed at JRC-Ispra in 2017, compared to the 1990-1999 period ± standard deviations.

4.4 Results for the year 2017

4.4.1 Meteorology

Meteorological data were acquired at using a Pyranometer (solar radiation) and a weather transmitter (T, P, RH, precipitation) located at 5 and 9 m above the ground at the provisional site and the new observatory, respectively. Meteorological data cover the whole of 2017. In Fig. 23, monthly values of these meteorological variables for 2017 are compared to the 1990-1999 average used as reference period.

The monthly mean solar radiation was significantly greater than average in April – July and October. Year 2017 was also warmer compared to the reference period from Feb. to August.

January and October were particularly dry, while June was wetter than usual. The total yearly rainfall was 996 mm, i.e. very little compared to the 1990-1999 average (1484 mm).

4.4.2 Gas phase air pollutants

SO_2, CO, NOx and O_3 were measured at the provisional site almost continuously during the year 2017, except for 10 days in February due to annual revision of the mobile laboratory and maintenance/linearity checks of all analysers, and for a total of 9 days in July and August due to the move from the provisional site to the new observatory (annual data coverage 95 %). In addition, O_3 data are available from Jan. 8th onwards. Expanded uncertainties were calculated to be 8% for SO_2, 7% for CO, 12% + 1.0 ppb for NO, 9% +1.4 ppb for NO_2 and 7% for O_3, which is in line with the *European Directive 2008/50/EC* (less than 15 % at the limit value). To render the time series comparable to the historical data acquired at the EMEP-GAW site at Bd 77p, *10 min SO_2, NOx and CO data were flagged for local contamination (1-8% of the data points), and hourly (and daily) averages were computed excluding the data points for which local contamination was identified*.

In 2017, the seasonal variations in SO_2, NO, NO_2, NO_x and O_3 were similar to those observed over the 1990-1999 period (Fig. 24). Concentrations are generally highest during wintertime for primary pollutants (SO_2, CO, NO_x), and in summertime for O_3. Higher concentrations of SO_2, CO, NO_x in winter result mainly from a least dispersion of pollutant during cold months (low boundary layer height and stagnant conditions), whereas the high concentration of O_3 during summer is due to enhanced photochemical production.

SO_2 concentrations (average = 0.8 µg/m³) were slightly greater than 2016 values, and about 6 times less compared to the reference period (1990-1999).

Daily mean CO concentrations ranged from 0.12 to 1.3 mg m^{-3} (0.1 – 1.1 ppmv), which are typical values in a regional background station like the atmospheric observatory in Ispra, and close to half of the values observed in the 1990's. The lowest values were observed in very clean air masses during Föhn events and windy summer days, and the highest values during cold winter nights.

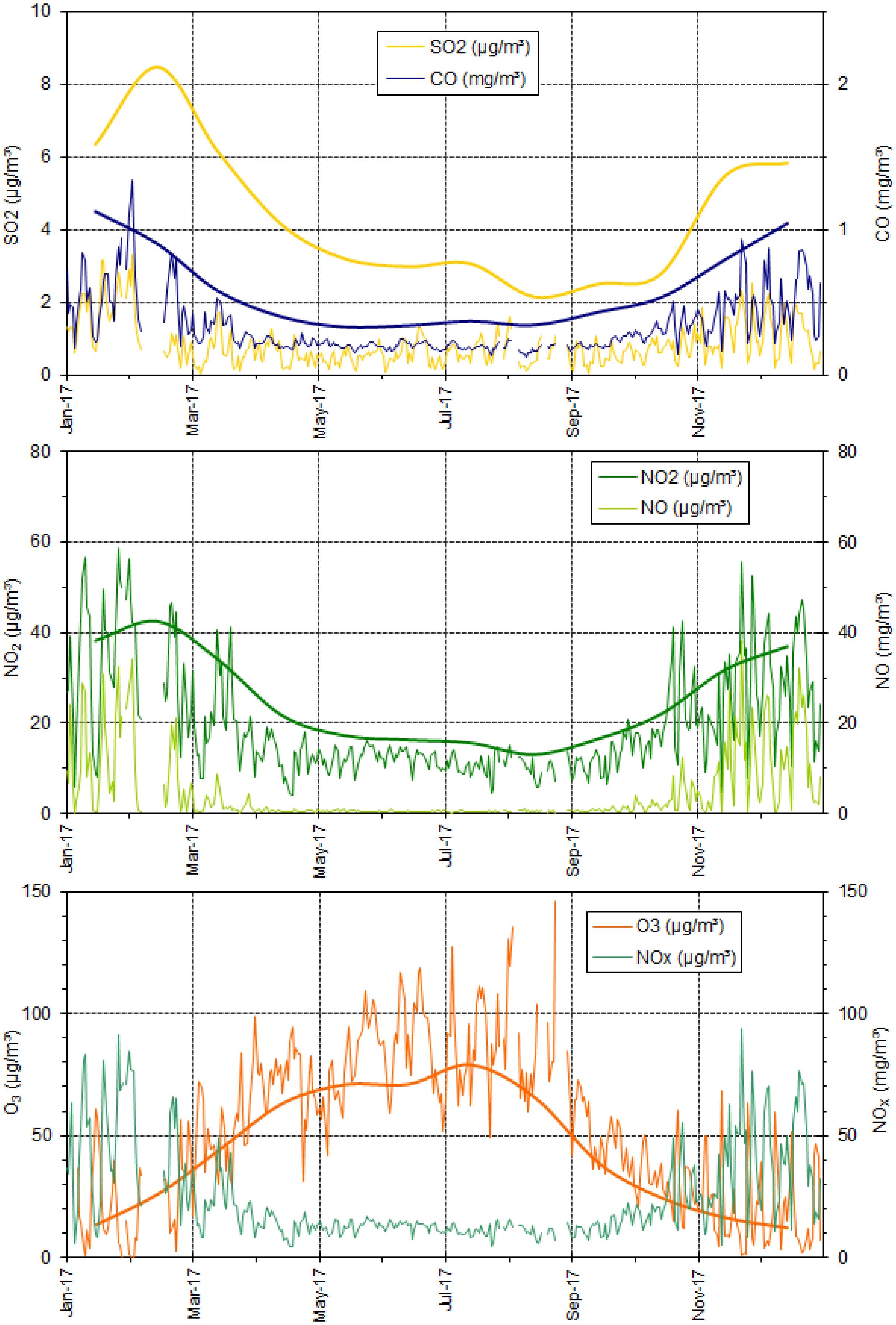

Fig. 24. Seasonal variations of the 24 hr averaged concentrations of SO_2, CO, NO_2, NO, O_3 and NO_x in 2017 (thin lines) and 1990-1999 monthly averages (thick lines: yellow=SO_2, blue=CO, green=NO_2, orange=O_3).

NO_2 concentrations (annual average = 19.5 µg m^{-3}) were on average only 25% less than during 1990-1999 and 10% greater than the 2016 levels, i.e. similar to the 2015 values. NO concentrations (annual average = 4.5 µg m^{-3}) were 35% less than in 2016, and similar to 2014 and 2015. Due to the short atmospheric lifetime of NO, NO concentrations are much sensitive to the filtering for local contamination.

The temporal coverage for O_3 measurements was 93% in 2017, and a total of 9 measurement days are lacking in July and August. (Fig. 15), when high levels occur (Fig. 24). O_3 indices for 2017 are therefore **lower limits**. The annual average O_3 concentration in 2017 (53 µg m^{-3}, 26 ppb) was 10% greater than in 2016, and confirmed the relatively high O_3 concentrations observed since the early 2010's. The high O_3 mean concentration can probably be partly explained by both the average insolation and temperature being greater than average in 2017.

The vegetation exposure to above the ozone threshold of 40 ppb (AOT 40 = Accumulated dose of ozone Over a Threshold of 40 ppb, normally used for "crops exposure to ozone") was 29000 ppb h, i.e. 25% more than in 2016 and slightly more than in 2015.

For quantification of the health impacts (population exposure), the World Health Organisation uses the SOMO35 indicator (Sum of Ozone Means over 35 ppb, where means stands for maximum 8-hour mean over day), i.e. the accumulated ozone concentrations dose over a threshold of 35 ppb (WHO, 2008). In 2017, SOMO35 was 5940 ppb day (Fig. 25), i.e. 75% more than in 2016 (3360), 50% more than in 2015 (4030), and twice as much as in 2014 (2950) when the summer was exceptionally rainy. In contrast, no extreme O_3 concentration events (>180 µg m^{-3} over 1 hour) were observed in 2017, to be compared to 8, 18, 2, 17, and 8 extreme events in 2012, 2013, 2014, 2015 and 2016, respectively. The value 180 µg m^{-3} over 1 hour corresponds to the threshold above which authorities have to inform the public (European Directive 2008/50/EC on ambient air quality and cleaner air for Europe).

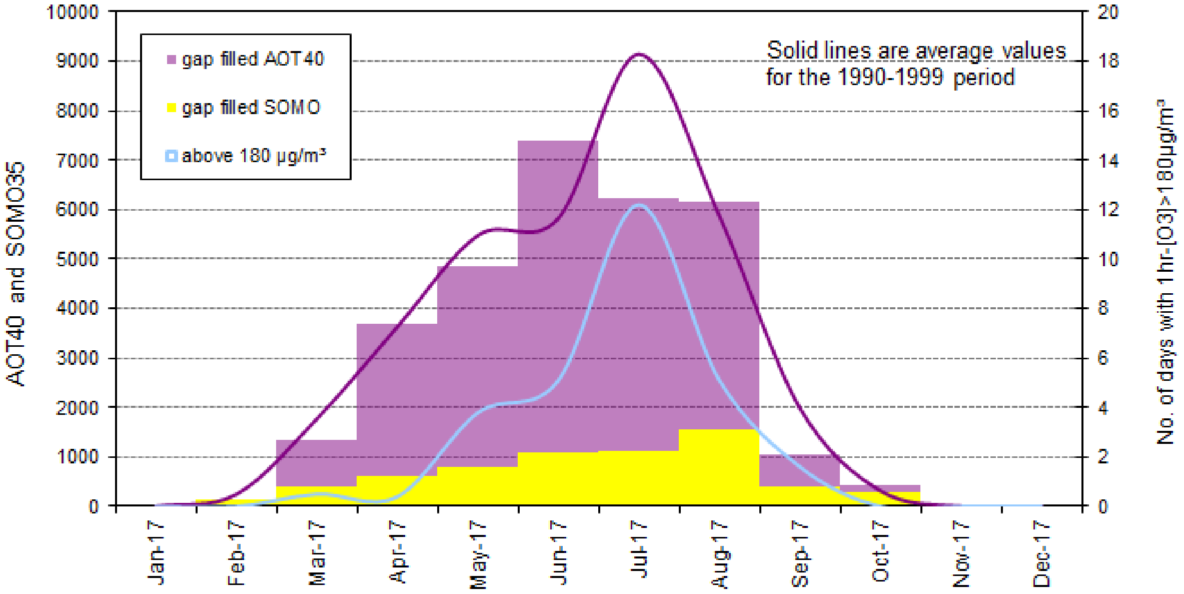

Fig. 25: AOT 40 (ppb h) and SOMO35 (ppb day) in 2017 (bars). No exceedance of the 1-hour averaged 180 µg/m³ threshold value was observed in 2017. Lines show values for the reference period 1990-1999.

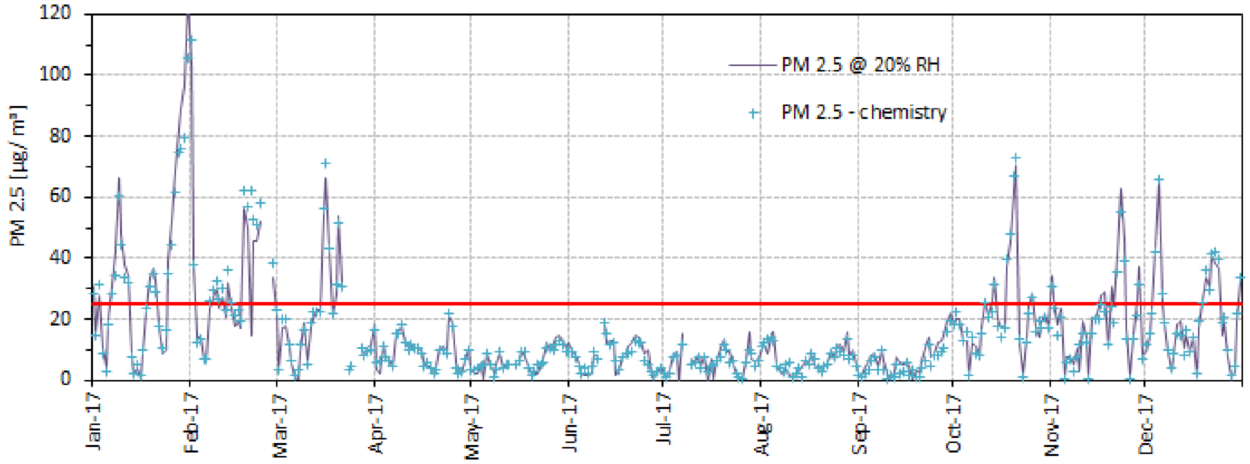

Fig. 26: 24hr-integrated $PM_{2.5}$ mass concentrations from off-line gravimetric measurements at 20 % RH and chemical determination of main constituents in 2017.The red line indicates the annual limit value of 25 µg/m^3 to be reached by 2015 (European directive 2008/50/EC).

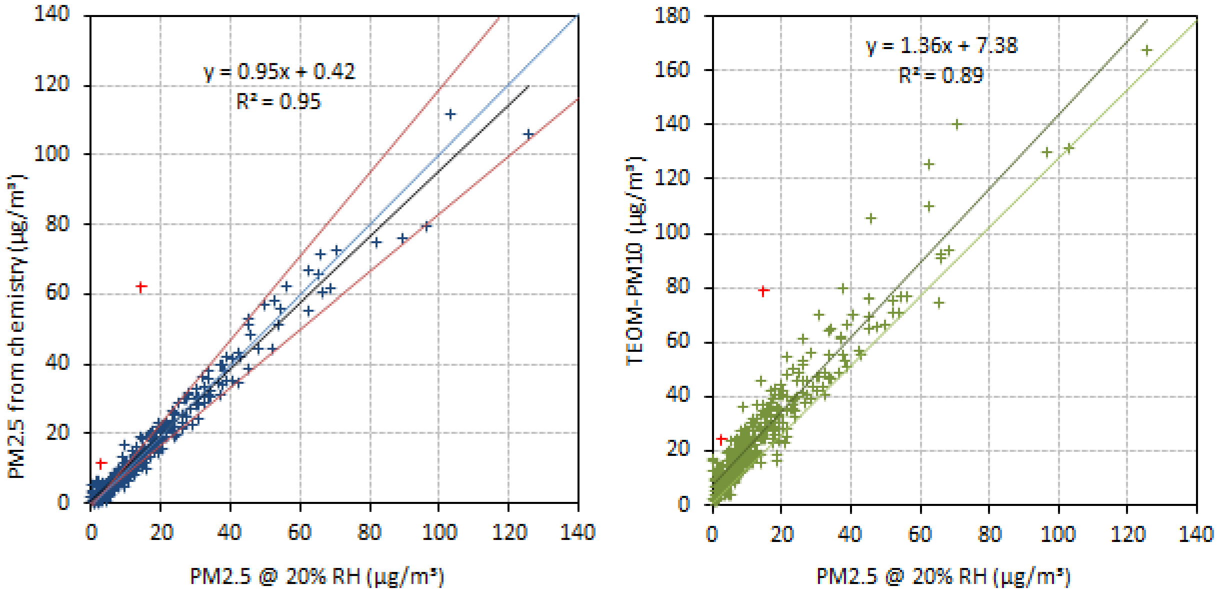

Fig. 27. Regressions between the gravimetric $PM_{2.5}$ measurements at 20 % RH and the sum of the $PM_{2.5}$ chemical constituents (left), and the FDMS-TEOM PM10 measurements (right) in 2017.

During the reference period 1990-1999, the information level of 180 µg m^{-3} had been exceeded 29 times per year on average. The other "protection of human health factor" mentioned by the European Directive 2008/50/EC (120 µg m^{-3} as maximum daily 8-hour average) was exceeded only 5 times in 2017 (vs 77 times in 2016), leading to a 3-year average of 53 exceedances per year, well above the Directive threshold (25 exceedances per year).

4.4.3 Particulate phase

4.4.3.1 Particulate matter mass concentrations

$PM_{2.5}$ concentrations (Fig. 26) measured gravimetrically at 20 % relative humidity (RH) averaged 15.5 µg m^{-3} over 2017 (data coverage = 97%). This was amongst the lowest values observed since this measurement was started in 2002 (lowest = 13.1 µg m^{-3} in 2014), well below the European annual limit value of 25 µg m^{-3} to be reached by 2015 (European directive 2008/50/EC). Gravimetric measurements of $PM_{2.5}$ mass at 20% RH and the sum of $PM_{2.5}$ mass constituents determined from chemical analyses are well correlated (Fig. 27), with relative differences below 20% for mass concentrations > 20 µg/m³.

The correlation between PM_{10} FDMS-TEOM and gravimetric $PM_{2.5}$ measurements for 2017 (Fig. 27) is not that good (and worse than in 2016), partly due to the variability in the PM_{coarse} fraction. The intercept of 7 µg/m³ suggests an offset in FDMS-TEOM measurements, negative sampling artefacts related to the quartz fibre filters used to collect PM, or a combination of both. In 2017, the annual data coverage for the FDMS-TEOM measurements of PM_{10} was 94%. The number of exceedances of the 24-hr limit value (50 µg m^{-3}) observed in 2017 (43) was greater than the threshold (35) indicated in the European directive 2008/50/EC. It is larger than the 21, 16, and 38 exceedances observed in 2015, 2014, and 2013, respectively (data coverage was only 31% in 2016). However, the 2017 annual PM_{10} average (28.5 µg m^{-3}) was similar to 2016, well below the annual limit value of 40 µg/m³ of the European directive 2008/50/EC.

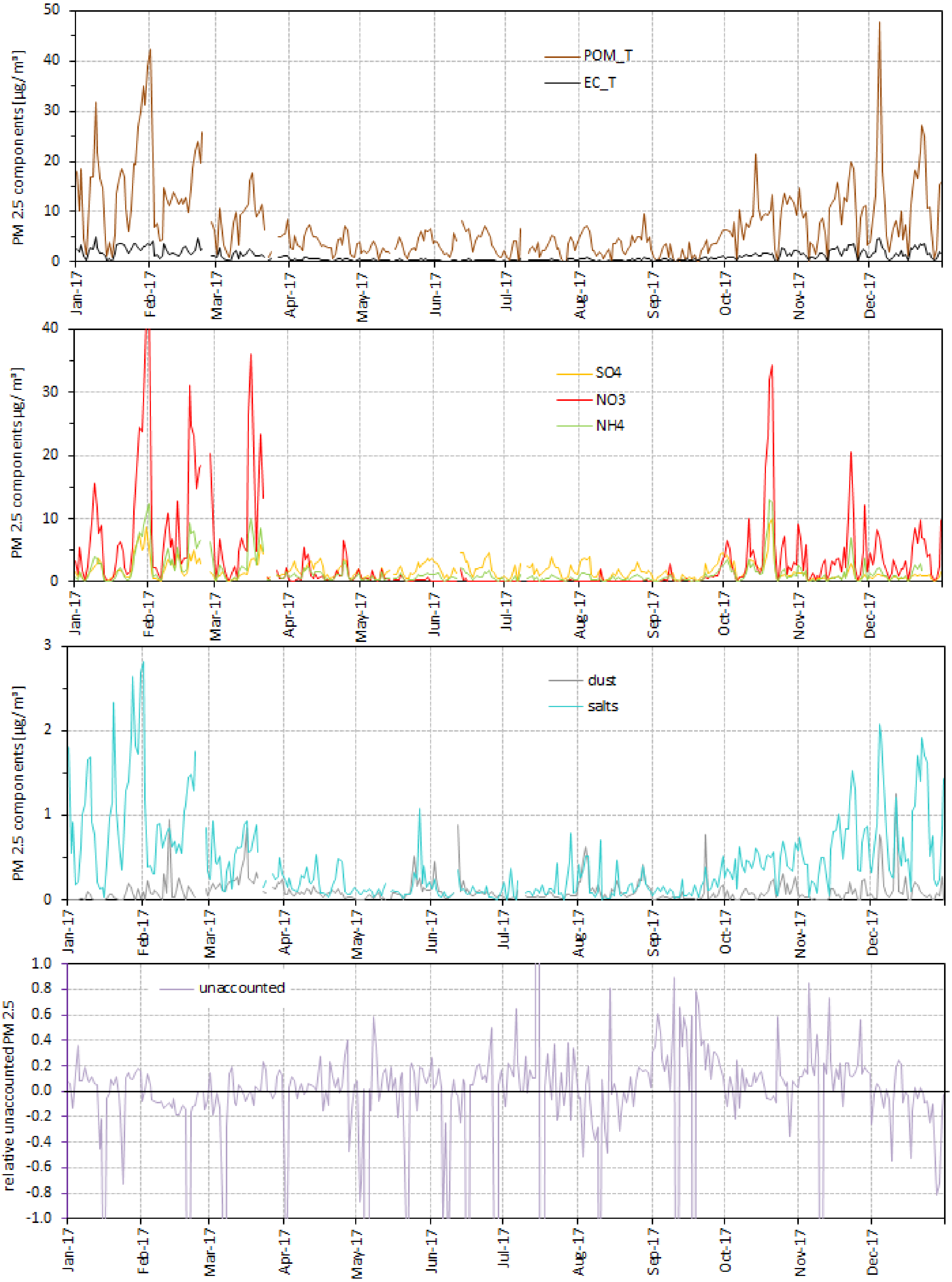

Fig. 28. 24-hr integrated concentrations of the main $PM_{2.5}$ constituents in 2017, and the relative unaccounted mass.

4.4.3.2 $PM_{2.5}$ chemical composition

Main ions (Cl^-, NO_3^-, SO_4^{2-}, $C_2O_4^{2-}$, Na^+, NH_4^+, K^+, Mg^{2+}, and Ca^{2+}), OC and EC were determined from the quartz fibre filters collected for PM mass concentration measurements for the whole of 2017 (data coverage = 97%).

Fig. 28 shows the temporal variations in the $PM_{2.5}$ main components derived from these measurements. Particulate organic matter (POM) is calculated by multiplying OC (organic carbon) values by the 1.4 conversion factor to account for non-C atoms contained in POM (Russell et al., 2003). "Salts" include Na^+, K^+, Mg^{2+}, and Ca^{2+}. Dust is calculated from Ca^{2+} concentrations and the regression (slope = 4.5) found between ash and Ca^{2+} in the analyses of ash-less cellulose filters (Whatman 40) in previous years. Most components show seasonal variations with higher concentrations in autumn and winter, and lower concentrations in summer, like $PM_{2.5}$ mass concentration. This is mainly due to changes in pollutant horizontal and vertical dispersion, related to seasonal variations in meteorology (e.g. lower boundary layer in winter). The amplitude of the POM, NH_4^+ and NO_3^- seasonal cycles may be enhanced due to equilibrium shifts towards the gas phase, and/or to enhanced losses (negative sampling artefact) from quartz fibre filters during warmer months. Indeed, historical data (May – Sept. 2013) show that the concentration of NH_4NO_3 in $PM_{2.5}$ determined from filters can be 1/5 of the concentration measured in the submicron aerosol with an ACSM (see 2013 annual report).

NH_4^+ follows NO_3^- + SO_4^{2-} very well as indicated by the regression shown in Fig. 29. This correlation results from the atmospheric reaction between NH_3 and the secondary pollutants H_2SO_4 and HNO_3 produced from the oxidation of SO_2 and NO_x, respectively. The ratio between NO_3^- + SO_4^{2-} and NH_4^+ is close to 1 (which means that sufficient NH_3 was available in the atmosphere to neutralise both H_2SO_4 and HNO_3), except for values > 0.45 µeq/m³, which had not been observed for several years. In these cases, $PM_{2.5}$ aerosol was probably quite acidic.

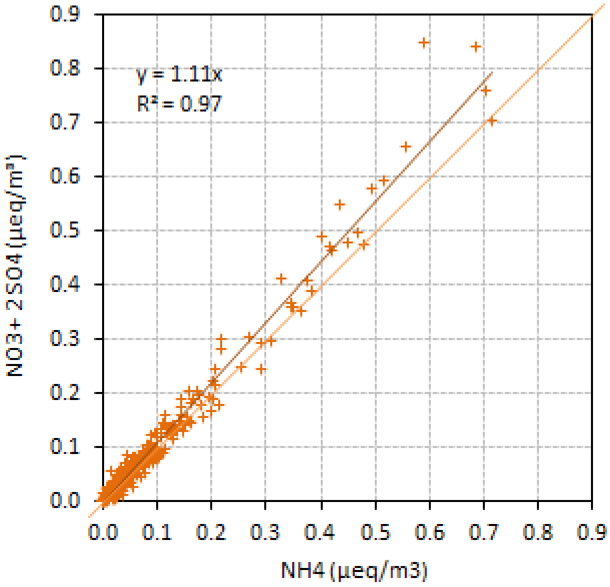

Fig. 29. SO_4^{2-} + NO_3^- vs. NH_4^+ (µeq/m³) in $PM_{2.5}$ for 2017

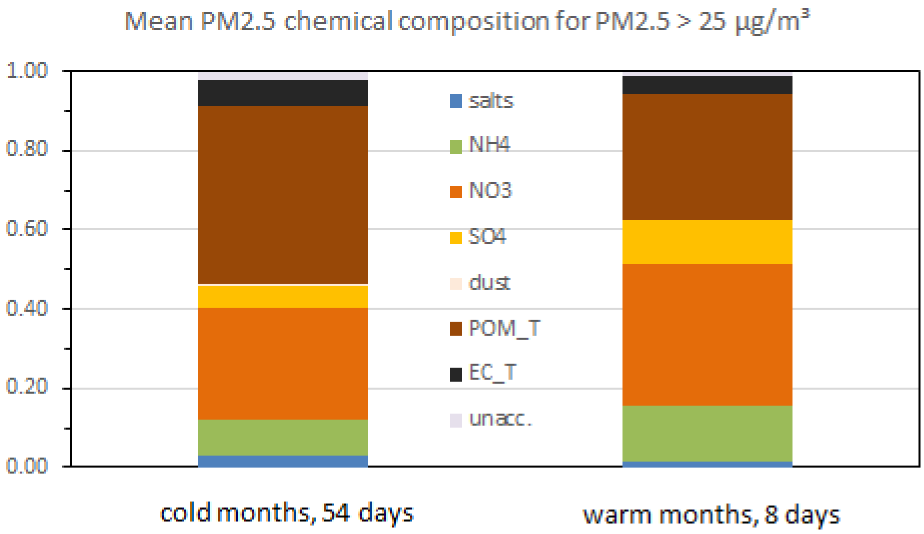

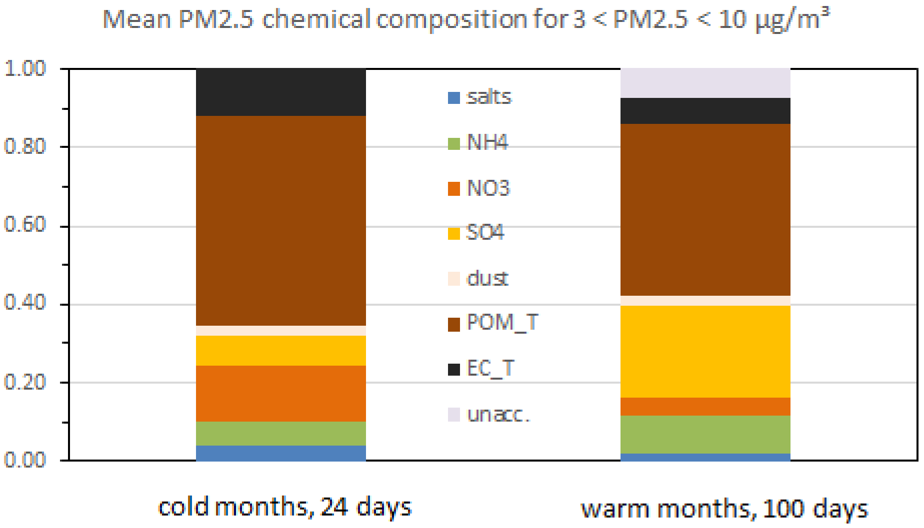

Fig. 30: Average composition of $PM_{2.5}$ in 2017 for days on which $PM_{2.5}$ > 25 µg/m³ (top) and 3 < $PM_{2.5}$ < 10 µg/m³ (bottom), over cold (Jan., Feb., Mar., Nov., Dec.) and warm (Apr. – Oct.) months.

4.4.3.3 Contribution of the main aerosol constituents to $PM_{2.5}$

The contributions of the main aerosol components to $PM_{2.5}$ are presented in Table 4 (annual averages) and in Fig. 30 (a) for days on which the "24-hr limit value for $PM_{2.5}$ of >25 µg/m³ was exceeded" during the cold months (Jan., Feb., March, Nov. and Dec., 57 cases) and the warm months (Apr. to Oct, 2 cases) and (b) for days on which 24-hr integrated $PM_{2.5}$ concentration was below 10 µg / m³ but above 3 µg / m³ during cold (36 cases) and warm months (139 cases).

These $PM_{2.5}$ compositions may not always represent accurately the actual composition of particulate matter in the atmosphere (mainly due to possible negative sampling artefacts), but are useful to assess which components contributed to the $PM_{2.5}$ mass collected by a quartz fibre filter downstream of a 20 cm-long carbon monolith denuder.

Over the whole year 2017, carbonaceous species accounted for 53% of $PM_{2.5}$ (EC: 7%, POM: 46%), and secondary inorganics for 37% (NH_4: 9%, NO_3: 14%, and SO_4: 15%). In both the cold and the warm seasons, particulate air pollution days are characterised by a strong increase in NO_3^- contribution. Considering low $PM_{2.5}$ concentration days, summertime is characterised by higher SO_4^{2-} concentrations (faster SO_2 photochemical conversion) and lower NO_3^- concentrations (equilibrium shifted towards the gas phase as temperatures increase). Dust and salts do not contribute significantly to the $PM_{2.5}$ mass, but their contribution is larger on cleanest days compared to most polluted days.

Table 4: Annual mean concentrations and contributions of major $PM_{2.5}$ constituents in 2016

constituent	salts Cl^-, Na^+, K^+, Mg^{2+}, and Ca^{2+}	NH_4^+	NO_3^-	SO_4^{2-}	POM	EC	dust	unaccounted
Mean concentration (µg m^{-3})	0.43	1.45	3.39	1.66	6.98	1.06	0.10	
Mean contribution (%)	2.7	8.8	13.7	14.8	46.0	7.4	1.0	5.7

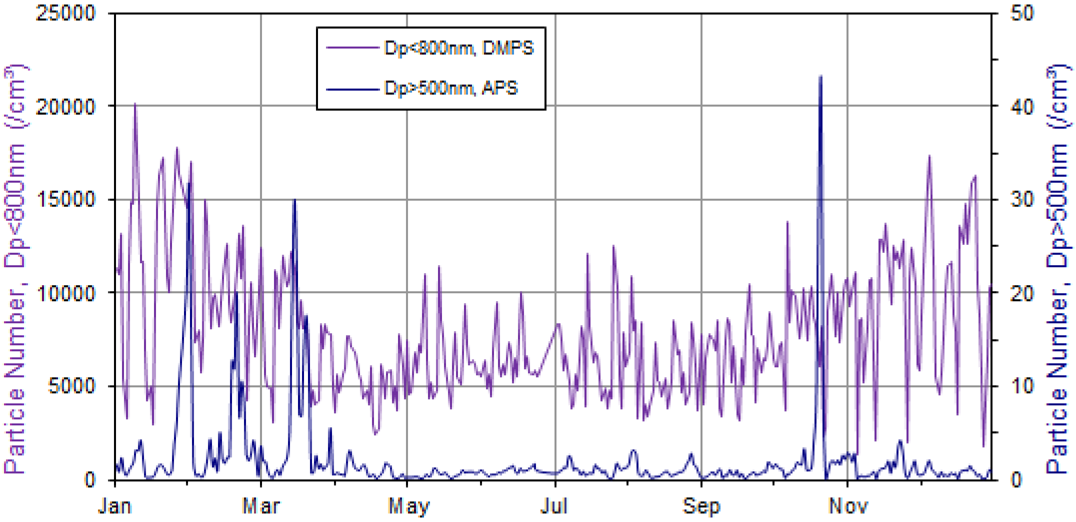

Fig. 31. 24 hr – mean particle number concentrations for Dp < 600 nm and Dp >500 nm.

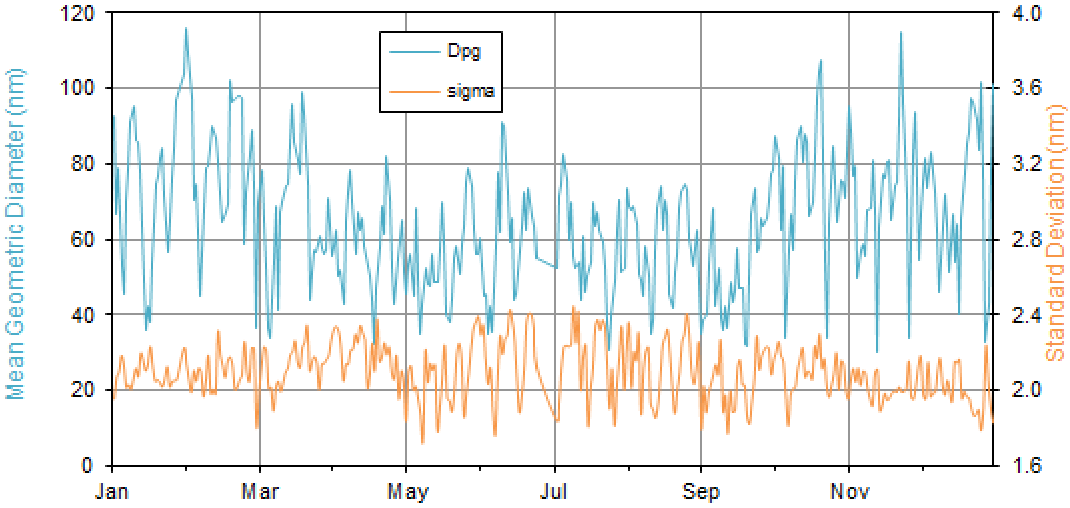

Fig. 32. 24 hr - averaged particle geometric mean mobility diameter (from the DMPS) and standard deviation

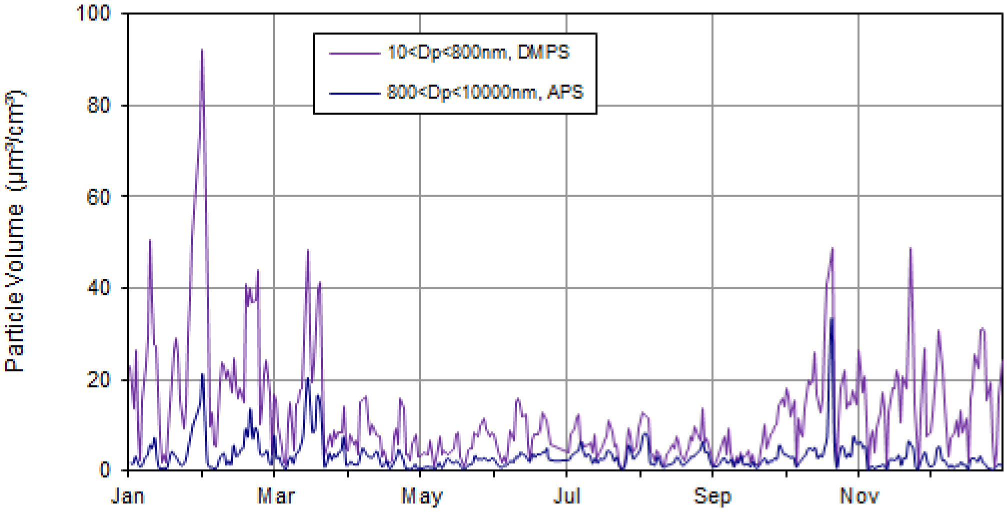

Fig. 33. 24 hr - averaged particle volume concentrations for Dp< 800 nm and Dp > 800 nm.

4.4.3.4 Aerosol micro-physical properties

Measurements of the number size distribution of particles smaller than 800 nm diameter were carried out using a Differential Mobility Particle Sizer almost continuously in 2017, except for a 7-day gap corresponding to the move from the provisional site to the new atmospheric observatory (27 June -2 July) and a few short breakdowns, resulting in a data coverage of 98%. The DMPS data presented here have been corrected for inlet diffusion losses and CPC efficiency.

Particle number concentrations averaged over 24 hr (from 08:00 to 08:00 UTC) ranged from 1360 to 20200 cm^{-3} (average: 7900 cm^{-3}) and followed a seasonal cycle similar to that of PM mass concentrations, with maxima in winter and minima in summer (Fig. 31). The vicinity of internal and external roads led to numerous episodes of local contamination, which were flagged during the data analysis process. Excluding the data points affected by local contamination (10% of the data), the annual mean particle number drops by 8%.

The mean mode diameter at RH < 30 % ranged between 30 and 116 nm (average = 65 nm) in 2017. These metrics are rather constant from year to year. However, the variations in particle size distribution characteristics (Fig. 32) show seasonal patterns as well: the mean geometric diameter is generally larger in winter (about 40-100 nm) than in summer (about 30- 80 nm), whereas the standard deviation of the distribution follows an opposite trend (with a larger variability in summer compared to winter).

The size distribution of particles larger than 500 nm was measured using an Aerodynamic Particle Sizer almost continuously over 2017 (data coverage: 98%, same gap as for the DMPS). Aerodynamic diameters were converted to geometric diameter assuming a particle density of 1.50. As previously observed, particles larger than 500 nm generally (90th percentile) accounted for <0.04% of the total particle number only (Fig. 31), but for more than 30 % of the total particle volume on average (Fig. 33). The seasonal variations in particle volume concentration reflect the changes in particle number and mean geometric diameter, with larger volumes in winter than in summer.

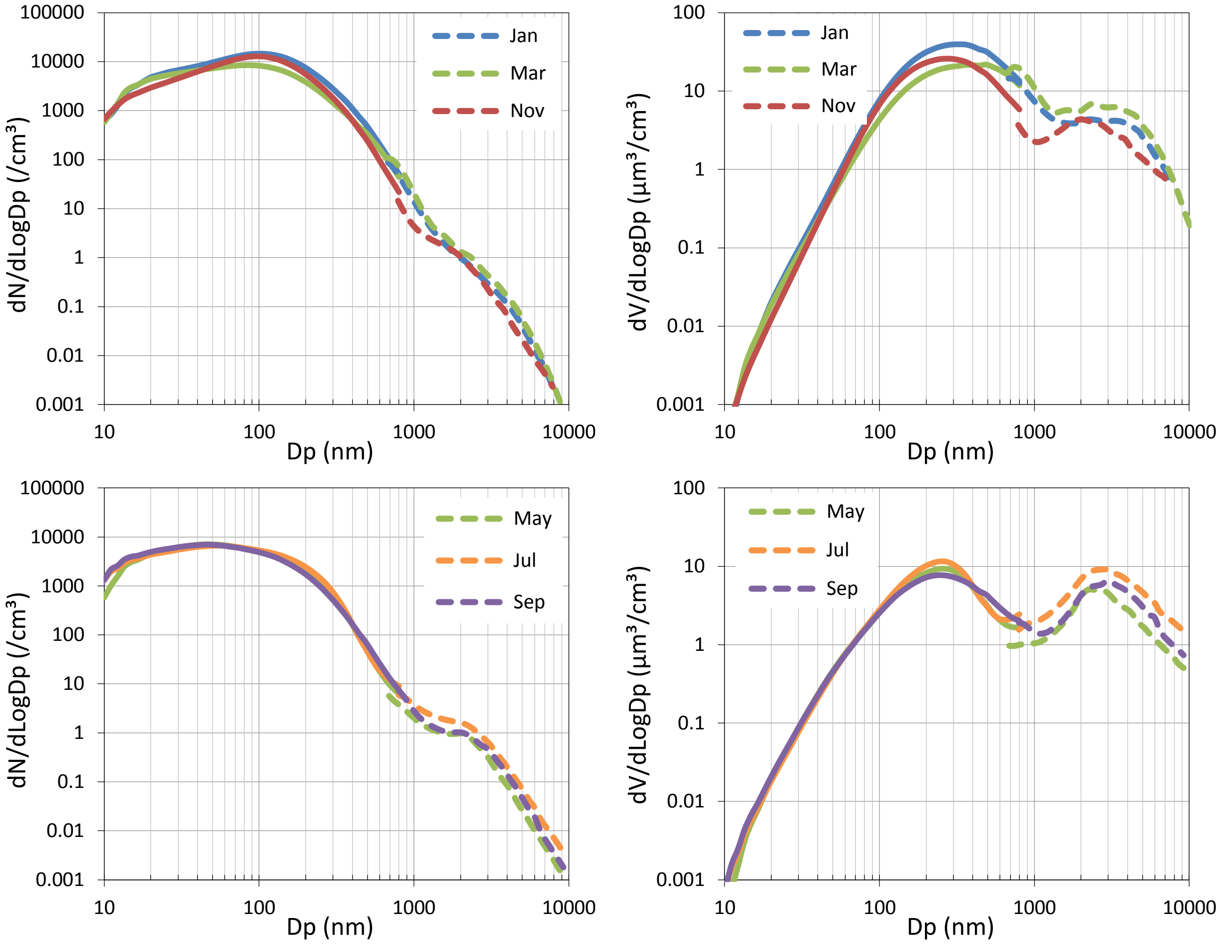

*Fig. 34. Monthly mean particle number (left) and volume (right) size distributions measured in 2017 with a DMPS (10-800 nm, solid lines) and an APS (0.85-10 µm, dashed lines). Particle densities of **1.5 g cm^{-3}** for cold months and **1.1 g cm^{-3}** for warm months (May –Sept.) were used to convert aerodynamic to geometric diameters.*

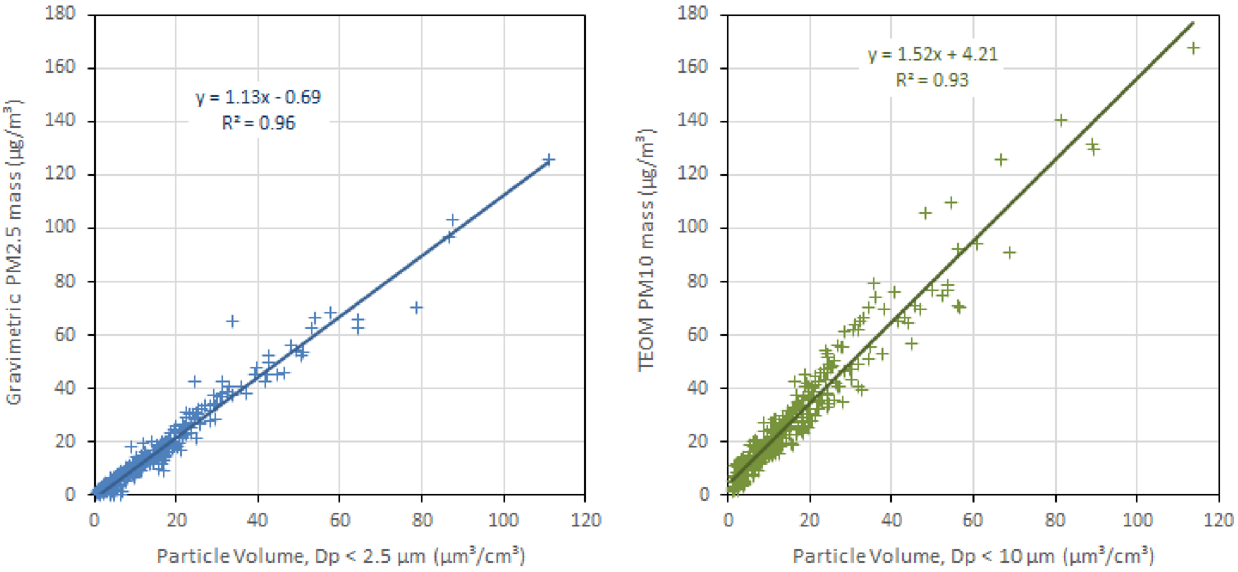

Fig. 35. 2017 regressions between (left) PM$_{2.5}$ mass concentrations determined from gravimetric measurements at 20% RH and particle volume (Dp < 2.5 µm) calculated from DMPS and APS measurements (<40% RH), and (right) between PM$_{10}$ mass concentrations measured with the TEOM-FDMS at 30 % RH and particle volume (Dp < 10 µm) at <40% RH.

Fig. 34 illustrates the large domination of sub-µm particles in the particle number size distribution. Even particle volume (and therefore PM mass) is dominated by sub-µm particles (almost half of the particle volume actually sits in particles < 300 nm). The apparent good agreement between particle number size distributions (Fig. 34) measured with the DMPS and the APS was obtained by using an aerosol density of 1.25 g cm^{-3}) to convert aerodynamic diameters (measured by the APS) to mobility diameters (measured by the DMPS) for all months, except June-Sept. where 1.5 fits better, to be compared with the range (1.6 ± 0.1 g cm^{-3}) expected for atmospheric particles (McMurry et al., 2002). Assuming that the DMSP is as accurate as it was during the calibration workshop in Jan. 2016 at the WCCAP (see report), this could be explained only by variations in the APS counting and/or sizing accuracy.

Both comparisons between PM mass and aerosol particle volume concentrations show a good correlation (Fig. 35), considering that possible variations in the aerosol density play a role in such regressions. The slope of the regression between $PM_{2.5}$ at 20 % RH and particle volume suggests a mean aerosol density of 1.13 (to be compared to 1.12, 1.16, 1.24, 1.20, 1.31, 1.38 and 1.37 in 2016, 2015, 2014, 2013, 2012, 2011 and 2010, respectively), while the regression between PM_{10} mass and aerosol volume concentration (for Dp < 10 µm) suggests a density of 1.52, in good agreement with the nominal value of 1.5 g cm^{-3} assumed to convert aerodynamic diameters to mobility diameters for particle volume calculations. This might indicate that $PM_{2.5}$ gravimetric measurements were underestimated.

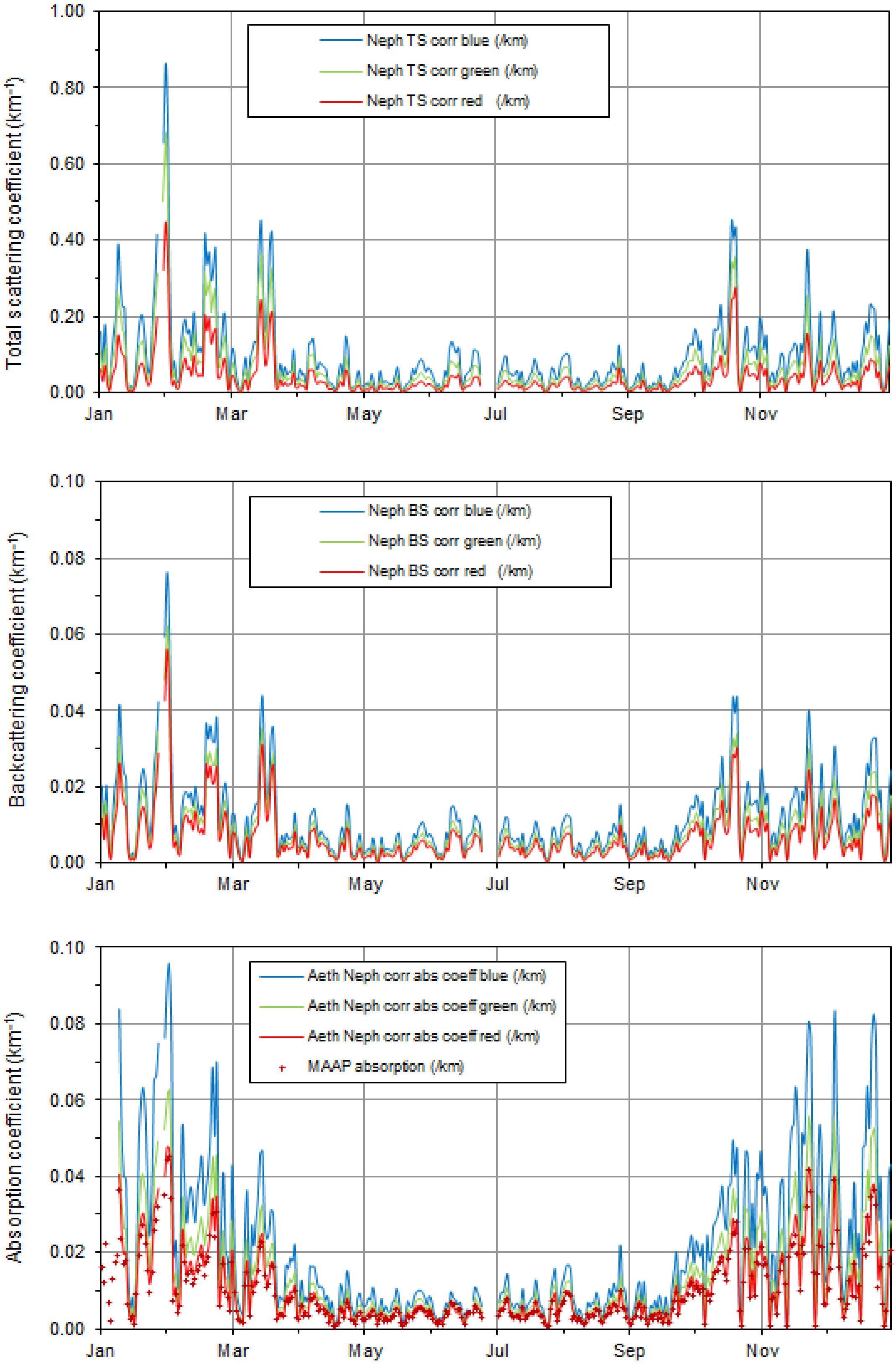

Fig. 36. Daily mean atmospheric particle light scattering (top), backscattering (middle), and absorption (bottom) coefficients at three wavelengths, derived from Nephelometer, Aethalometer and MAAP measurements (not corrected for RH) performed in 2017.

4.4.3.5 Aerosol optical properties

Aerosol optical properties have been monitored continuously during 2017 (data coverage = 98% for both light scattering and light absorption measurements). Data from the Nephelometer (Fig. 36 (a and b) have been corrected for angular non-idealities (truncation to 7 – 170°, slightly not cosine-weighted distribution of illumination) according to Anderson and Ogren (1998), but not for RH effects. Thanks to the use of a Nafion dryer and the reduction of the sampling flow rate to 6-12 L min^{-1}, the Nephelometer internal RH was maintained below 40% for 70% of the time, with exception occurring mainly in May - Sept. At 40% RH, aerosol scattering is on average increased by about 20 % compared to 0% RH in Ispra (Adam et al., 2012).

Atmospheric particle absorption coefficients at 7 wavelengths were derived from the Aethalometer AE-31 data corrected for the shadowing and multiple scattering effects when Nephelometer data were available, according to Weingartner et al. (2003), making use of coefficients derived from Schmid et al. (2006), i.e. 3.60, 3.65 and 3.95 at 470, 520, and 660 nm, respectively (Fig. 36 c).

Both scattering and absorption coefficients follow seasonal variations (Fig. 36) in line with PM mass variations, mainly controlled by pollutant dispersion rates.

The uncertainty in the multiple scattering correction factor may introduce a quite large uncertainty in the aerosol absorption coefficient values, since correction factors ranging from 2 to 4 have been proposed (Weingartner et al., 2003; Arnott et al., 2005). The use of the correction factors listed above leads to an aerosol absorption coefficient at 660 nm slightly larger than the absorption coefficient obtained from the Multi Angle Absorption Photometer (MAAP) for 670 nm, which cannot be explained by the difference in wavelengths only (Fig. 37). NB: in December 2015, it was recommended by ACTRIS that the coefficient 3.5 should be used for all wavelengths without any correction for the filter loading.

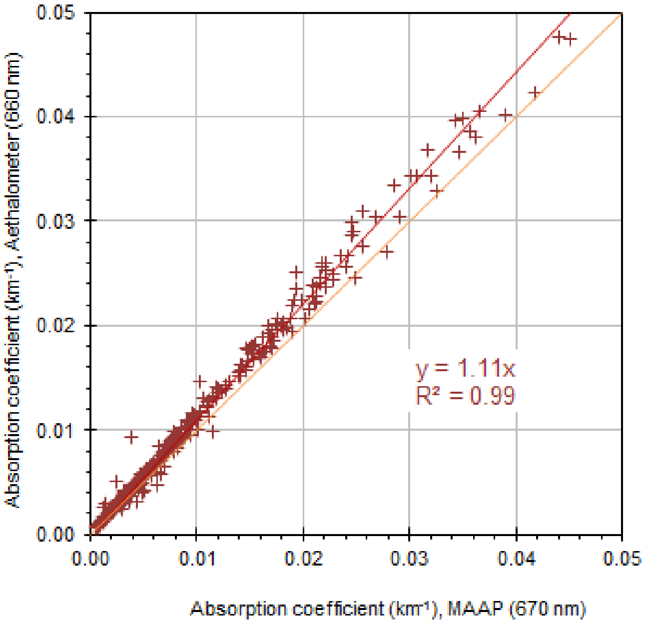

Fig. 37. Comparison between the Aethalometer and MAAP derived light absorption coefficients at 660 and 670 nm, respectively. Data points are daily averages (2017).

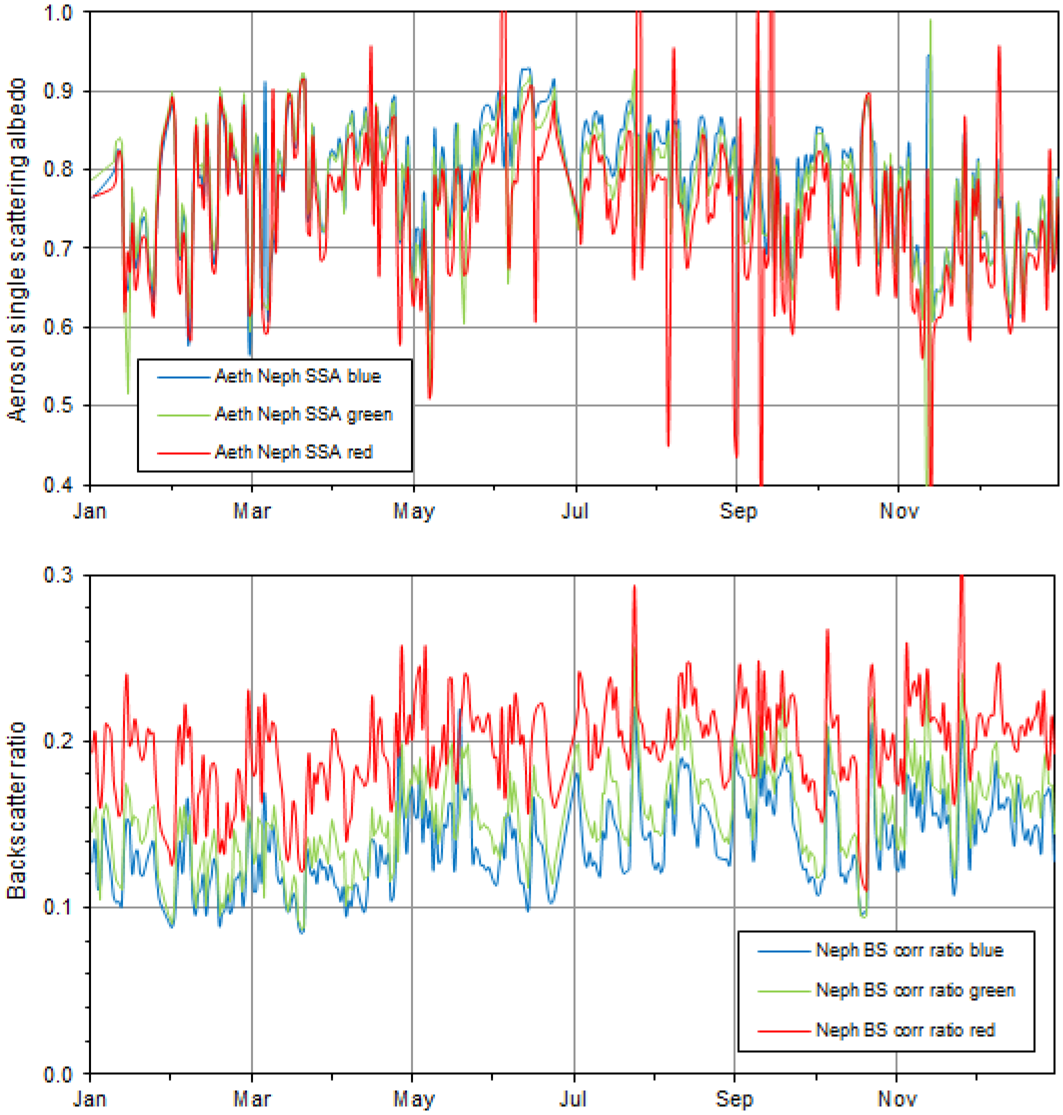

Fig. 38. Aerosol 24-hr averaged single scattering albedo and backscatter to total scatter ratio at three wavelengths corresponding to blue, green and red, as calculated for 2017 (RH < 40%).

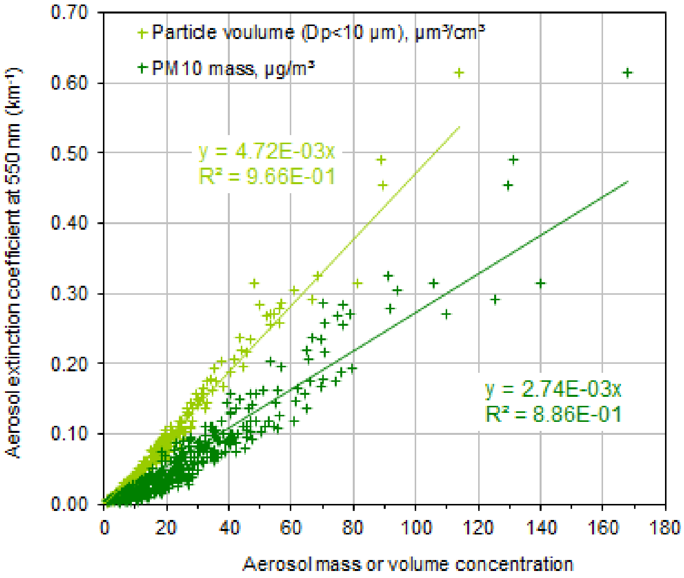

Fig. 39. Regression between the aerosol extinction coefficient and PM_{10} mass (FDMS-TEOM) and volume (DMPS + APS) concentrations in 2017.

The 24 hr-averaged aerosol single scattering albedo (SSA) at $\lambda = 550$ nm (at RH generally < 40 %) ranged from 0.51 to 0.93 (annual average 0.78), with generally lower values in autumn and winter compared to spring and summer (Fig. 38, top). In 2017, measurements were performed at the new atmospheric observatory, further away from internal and external roads than the provisional site. As a consequence, the mean SSA was higher than in 2016 (0.72), and reached similar values to 2010-2013 (0.75-0.79), when measurements were performed at the historical site (Fig. 1). Excluding the values clearly affected by local influences, the mean single scattering albedo was 2% greater. The absorption coefficients were flagged for local contamination before submission to the WDCA data bank (EBAS).

The backscatter / total scatter ratio at 550 nm (Fig. 38, bottom) ranged from 0.09 to 0.26 (average 0.16), i.e. about 10% greater than the previous year.

The aerosol extinction coefficient and particle mass or volume concentrations are rather well correlated (Fig. 39). The slope of the regression between extinction and mass shows that the mass extinction cross section was on average 2.7 $m^2\,g^{-1}$ in 2017 (vs 3.1 in 2016, 2.5 in 2015, 2.8 in 2014, and 3.4 in 2012 and 2013), i.e. very low compared with 4.7 $m^2\,g^{-1}$, the value calculated based on the aerosol mean chemical composition during 2017, and mass cross section coefficients for the various constituents found in the literature (see Table 5). Based on the particle volume determination, and assuming a mean aerosol density of 1.5 g cm^{-3}, the mass extinction cross section would be greater (3.2 $m^2\,g^{-1}$). The agreement between these two estimates of the aerosol extinction cross section has deteriorated since 2010 – 2012, which underlines the necessity of implementing urgently new independent measurements of the light extinction.

Table 5: Mean aerosol chemical composition ($PM_{2.5}$) in 2017 and extinction cross section.

	2017 $PM_{2.5}$ comp. (%)	σ_{ext} (m²/g)	Reference (for σ_{ext})
"sea salt"	3	1.3	Hess et al., 1998
NH_4^+, NO_3^- and SO_4^{2-}	40	5.0	Kiehl et al., 2000
organic matter	47	3.6	Cooke et al., 1999
elemental carbon	9	11	Cooke et al., 1999
Dust	1	0.6	Hess et al., 1998
Total	**100**	**4.7**	

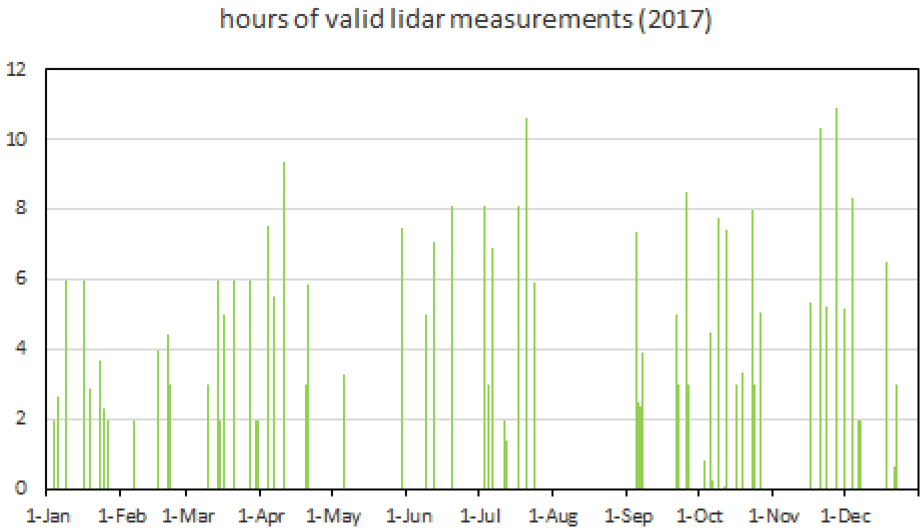

Fig. 40. Aerosol vertical profile measurements performed daily with the Raman Lidar in 2017.

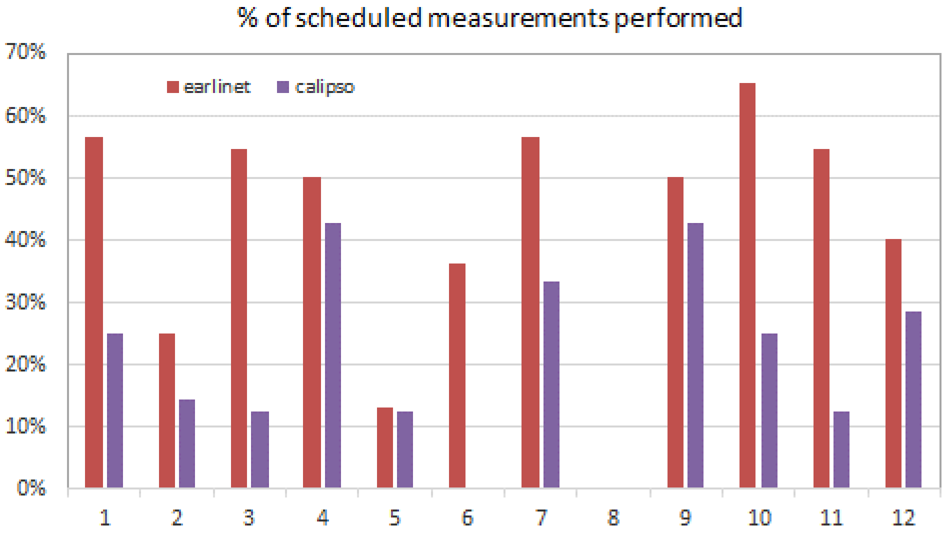

Fig. 41. Scheduled aerosol vertical profiling measurements performed monthly during the EARLINET climatology and Calipso overpass time slots in 2017.

4.4.3.6 Aerosol vertical profiles

The Raman LiDAR from Raymetrics was operated for measuring aerosol vertical profiles from the historical EMEP Ispra site (Bd 77R) for the whole of 2017, weather and staff availability permitting.

In 2017, the LiDAR was operated for 320 hours (Fig. 40) vs 177 hours in 2016 to fulfil the ACTRIS requirements: at noon (2 hr) and sunset (4-5 hr) on Mondays, and at sunset (4-5 hr) on Thursdays (EARLINET climatology), plus during the ESA satellite Calipso overpasses ± 1 hr (every ~9 days at 01:40 and 12:35 UTC). The scheduled measurements were thus covered at 42% and 22% (Fig. 41), respectively, i.e. still below ACTRIS' target of 50%. This is mainly due the fact that the LiDAR cannot be run automatically and currently only 1 operator is qualified to operate it.

The LiDAR emission and reception windows were replaced by the manufacturer on May 23rd. Alas, the emission window was damaged again by the laser on July 27th. The LiDAR data obtained from end of May to end of July were successfully submitted to the ACTRIS-EARLINET Single Calculus Chain (SCC) for data inversion, and optical products were submitted to the data base. The data obtained before and after this period shall be processed after the determination of a series of parameters characterising the LiDAR optics.

Fig. 42 shows an example of aerosol light backscatter profiles signal at 532 nm measured in Ispra and retrieved using the SCC for July 3rd, 2017, from 19:35 to 21:00 UTC. The data show particles accumulating close to the Earth's surface in the evening, and another huge pollution layer between 1000 and 4000 m above the ground.

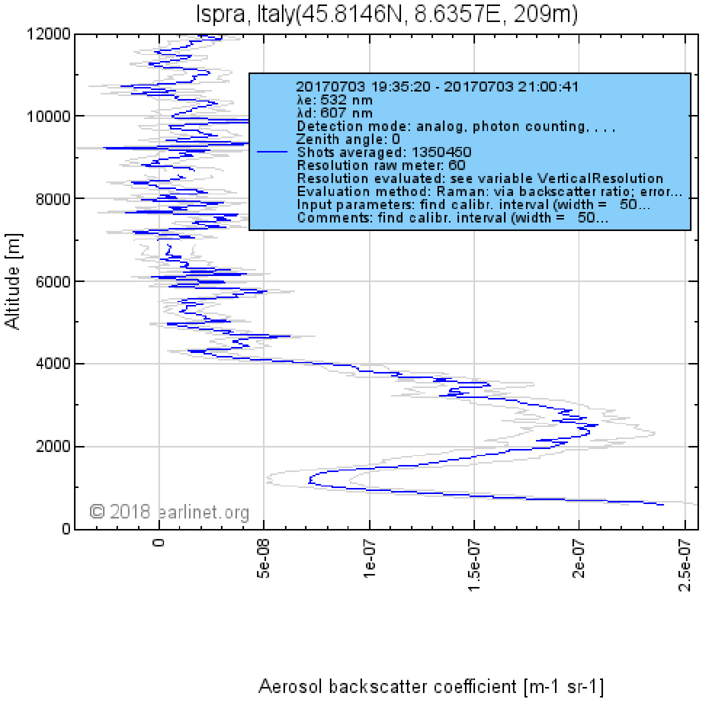

Fig. 42: Examples of aerosol light backscatter profiles obtained at JRC-Ispra with the Raman LiDAR using the ACTRIS Single Calculus Chain and retrieved from the ACTRIS-EARLINET database, for July 3rd, 2017, between 19:35 and 21:00 UTC.

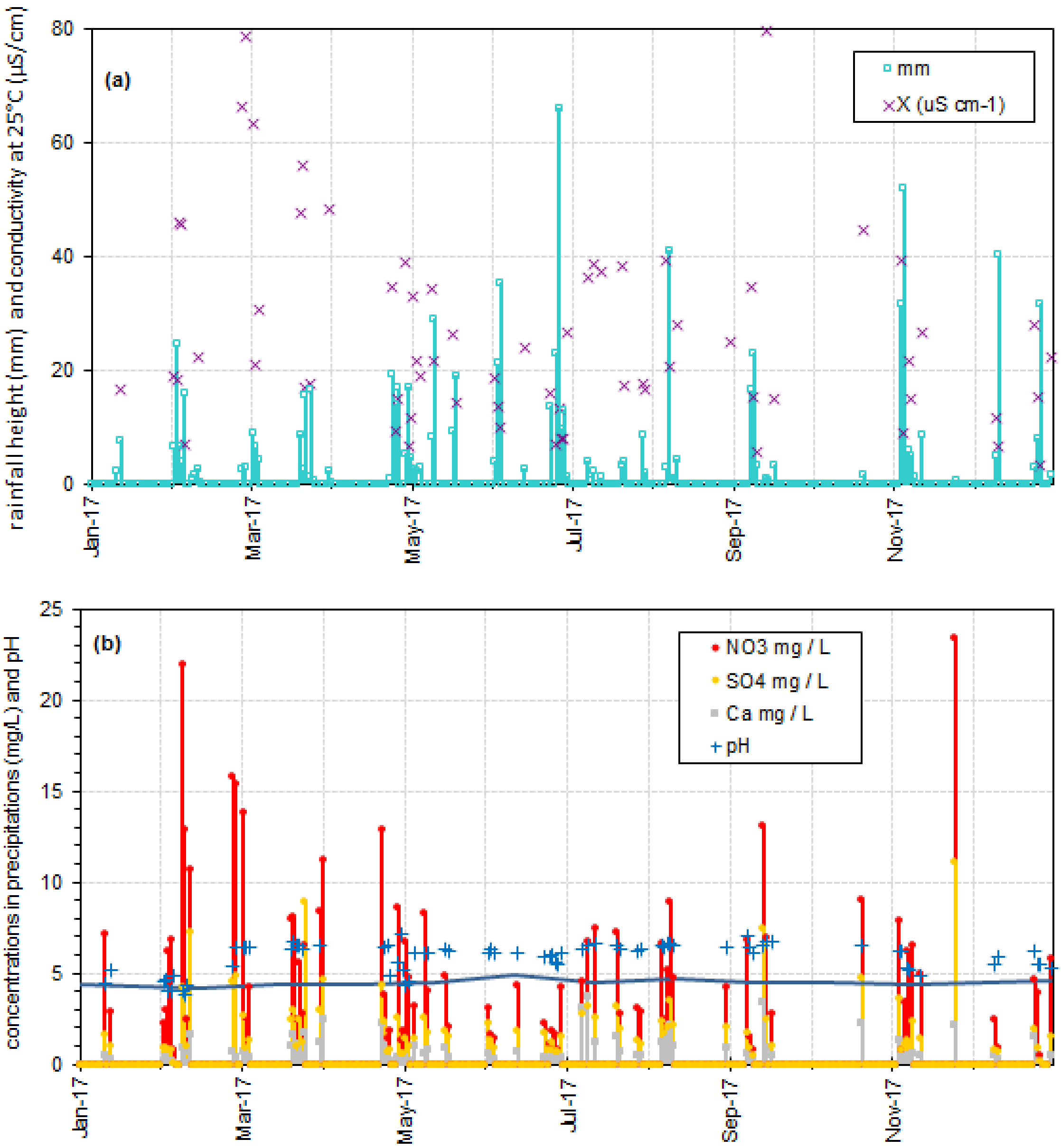

Fig. 43 (a) *Precipitation amount, conductivity and (b) concentrations of 3 major ions in precipitation (bars) and pH (crosses) in 2017, and during the 1990-99 period (line).*

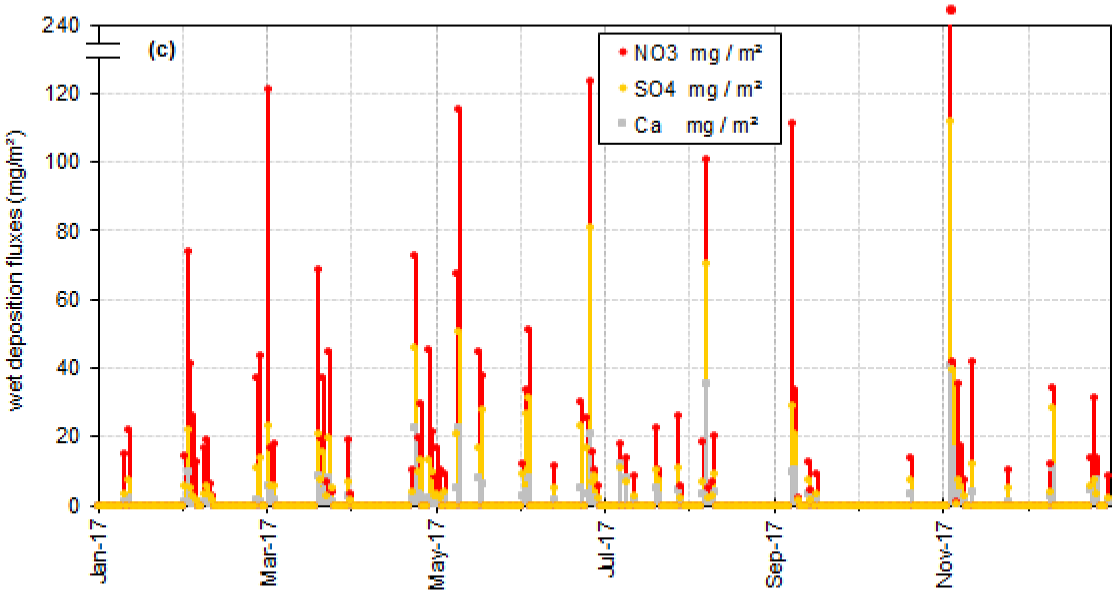

Fig. 44. Wet deposition fluxes of 3 main ions measured in rain water in 2017.

4.4.4 Wet deposition chemistry

In 2017, 83 precipitation samples were collected, fewer than in previous years, due to the fact that it rained much less frequently than usual. The ionic content, acidity (pH) and conductivity were measured in 83, 75 and 68 of these samples (those where the water volume was sufficient minus 4 major events). The precipitation height measured during the collected events ranged from 0.24 to 66 mm (Fig. 43a) for a total of 804 mm.

The ranges of concentrations measured in these samples are indicated in Table 6. Volume weighted mean concentrations of the anthropogenic species NO_3^- and SO_4^{2-} were lower than the 1990-1999 averages in 2017 less, the concentration of and NH_4^+ was higher, while concentrations of all the marine and crustal components were similar to the long-term average. All but 2 precipitation samples collected in 2017 were acidic (pH < 7.0), and 24 had a pH<5.6 (equilibrium with atmospheric CO_2), compared to 25 in 2016, 43 in 2015, and 58 in 2014. Amongst those, 9 samples had a pH < 4.6 (compared to 3 in 2016, 18 in 2015, and 9 in 2014 and 2013).

Wet deposition was quite evenly distributed over the year, but almost no wet deposition occurred in January and October (Fig. 44). In 2017, the annual wet deposition flux of the main acidifying and eutrophying species was 1.1, 2.5, and 1.1 g m^{-2} for SO_4^{2-}, NO_3^-, and NH_4^+, respectively, i.e. about 20% less than in 2016 and the previous years (see also section 4.6 next page),probably due to the low level of precipitation in 2017.

Table 6: Statistics relative to the precipitation samples collected in 2017 (averages are volume weighted).

	pH	cond. µS / cm	Cl- mg / l	NO3- mg / l	SO42- mg / l	Na+ mg / l	NH4+ mg / l	K+ mg / l	Mg2+ mg / l	Ca2+ mg / l
Average	5.36	20.70	0.46	3.62	1.60	0.36	1.46	0.10	0.09	0.69
Min	3.82	3.0	0.10	0.43	0.09	0.04	0.08	0.01	0.01	0.06
Max	7.12	79.6	5.3	23.4	11.1	4.0	9.4	0.7	0.8	3.7
1990-1999	4.40	24.86	0.44	3.94	3.07	0.23	1.25	0.09	0.06	0.45

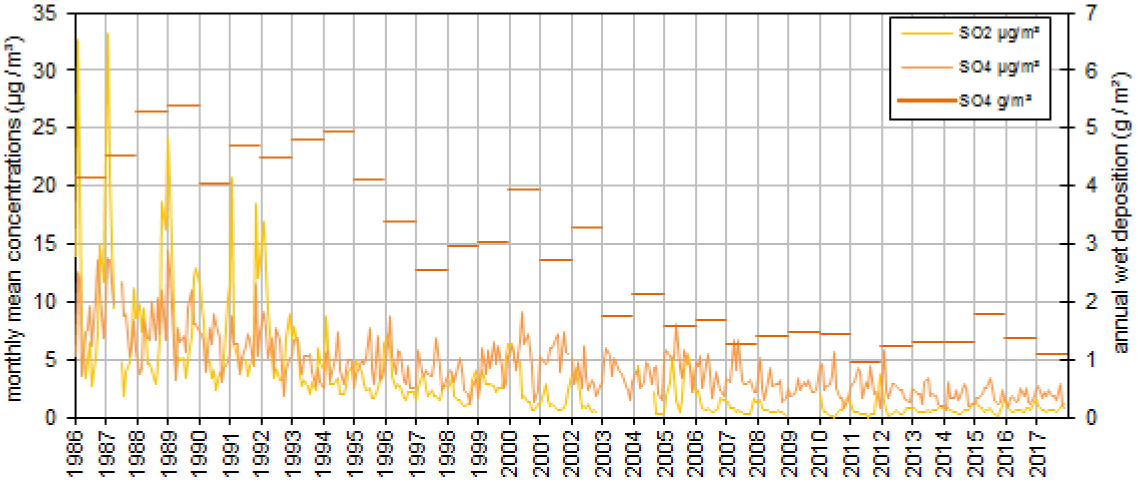

Fig. 45. Oxidised sulphur species monthly mean concentrations and yearly wet deposition.

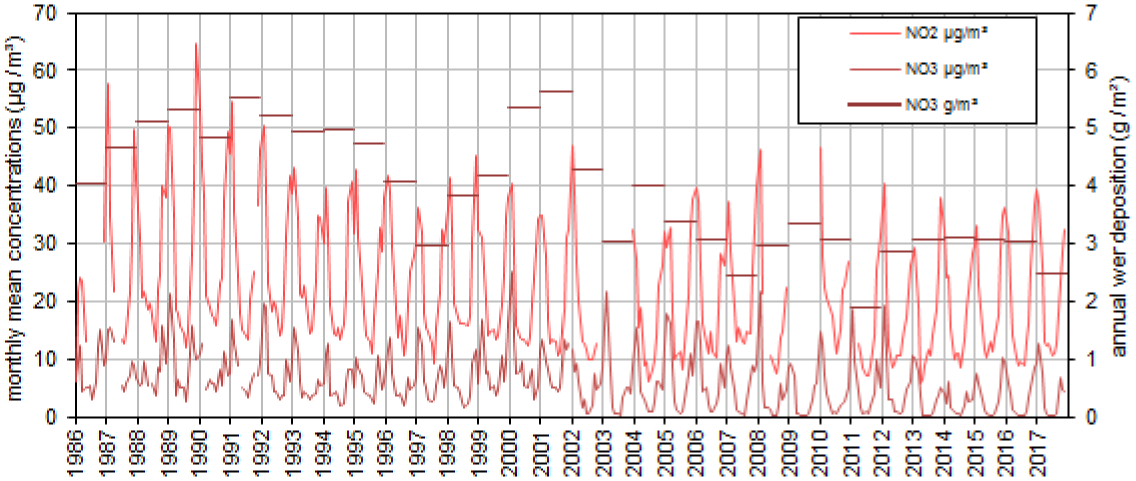

Fig. 46. Oxidised nitrogen species monthly mean concentrations and yearly wet deposition.

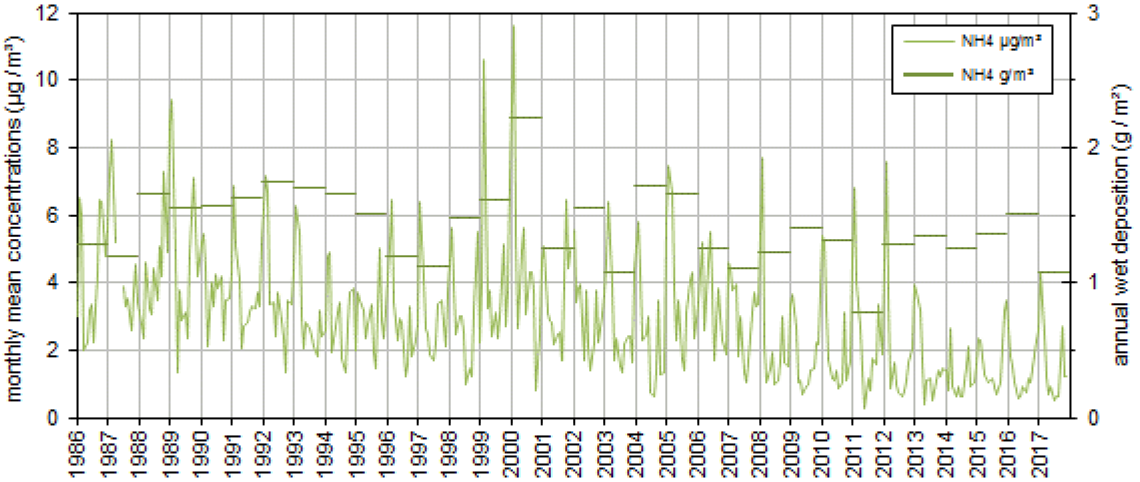

Fig. 47. Reduced nitrogen species monthly mean concentration and yearly wet deposition.

4.5 Results of year 2017 in relation to 30+ years of measurements

4.5.1 Sulphur and nitrogen compounds

The annual mean SO_2 concentration in 2017 was slightly higher than in 2016, but in line with the range of values (0.6 – 0.8 µg/m³) observed at our station in the 2010's. SO_2 concentrations are nowadays ~10 times smaller than in the 90's, and less than half compared to the 2000's. Annual mean particulate SO_4^{2-} concentration was 13% more than its historical minimum of 2016, but in the range of the values observed for the 3 previous years. Still, 2017 SO_4^{2-} concentrations were on average half compared to the 2000's, and 1/3 compared to the 90's. It should be kept in mind that SO_4^{2-} concentrations were measured in PM_{10} or in $PM_{2.5}$ from 2002 onwards, whereas it was measured in TSP (Total Suspended Particulate) from 1986 to 2001. However, simultaneous sampling of PM_{10} and TSP over 14 months showed that SO_4^{2-} in PM_{10} is generally less than 5 % lower than in TSP. SO_4^{2-} is mainly present in the $PM_{2.5}$ fraction at our site (see Fig. 24 of the ABC-IS annual report 2010). From 2005 onwards the calculations were as follows:

$$SO_4^{2-}(PM_{10}) = SO_4^{2-}(PM_{2.5}) \times \langle SO_4^{2-}(PM_{10}) / SO_4^{2-}(PM_{2.5}) \rangle$$

the average $\langle SO_4^{2-}(PM_{10})/ SO_4^{2-}(PM_{2.5}) \rangle$ being calculated based on the simultaneous PM_{10} and $PM_{2.5}$ samples collected in 2010-2012.

Particulate SO_4^{2-} concentrations decreased much less than SO_2 concentrations, which suggests that locally produced SO_2 decreased much more than possibly long-range transported SO_4^{2-} over the past 25-30 years. SO_4^{2-} wet deposition in 2017 was the second lowest on record, and 20% less than over the past 5 years. The relatively high SO_4^{2-} concentrations and low wet deposition can be related to the high temperature and insolation and low precipitation observed in 2017.

In 2017, the annual mean NO_2 concentration was not specially low, i.e. equal to the average over the 2010's, and still 25% less compared to the 90's. Monthly mean concentrations of nitrogen dioxide (NO_2) do not show as much of a pronounced decreasing trend as seen for SO_2 over the past 30 years (Fig. 46). Over the last decade, NO_2 maxima are not significantly lower than during the previous one and tend to increase, which does not reflect the 30 % abatement in NO_x emissions reported in the emission inventories for this period. The particulate NO_3^- annual mean concentration observed in 2017 was also larger than during the past 4 years, but still 40% less than the average over 1990 – 2010. It should be noted that since October 2000, NH_4^+ and NO_3^- have been measured from quartz fibre filters, which are known to lose NH_4NO_3 at temperatures > 20 °C, as demonstrated e.g. by the comparison with the ACSM measurements we performed in Ispra in 2013. This might contribute significantly to the low summertime minima NO_3^- seen since 2002. Furthermore, NO_3^- was measured from PM_{10} or in $PM_{2.5}$ from 2002, and no more from TSP, as over the 1986 to 2001 period. However, simultaneous sampling of PM_{10} and TSP over 14 months showed that NO_3^- in PM_{10} is generally less than 5 % lower than in TSP, like SO_4^{2-}. From 2005 and onwards the calculations were as follows

$$NO_3^-(PM_{10}) = NO_3^-(PM_{2.5}) \times \langle NO_3^-(PM_{10}) / NO_3^- (PM_{2.5}) \rangle$$

the average $\langle NO_3^-(PM_{10})/ NO_3^-(PM_{2.5}) \rangle$ being calculated based on the simultaneous PM_{10} and $PM_{2.5}$ samples collected in 2010-2012. NO_3^- wet deposition annual flux observed in 2017 was the second lowest ever recorded since 1986 in Ispra, and 20% less than the average over the 5 past years.

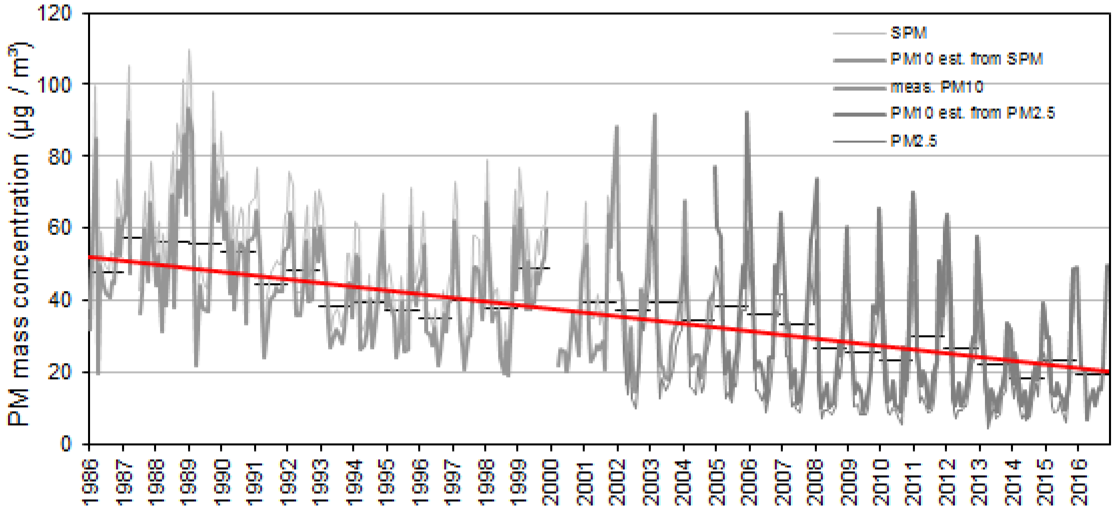

Fig. 48. *Particulate matter mass concentration monthly (grey) and annual (black) averages. The red line is the long term trend over annual averages. All values are gravimetric measurements or estimates from gravimetric measurements.*

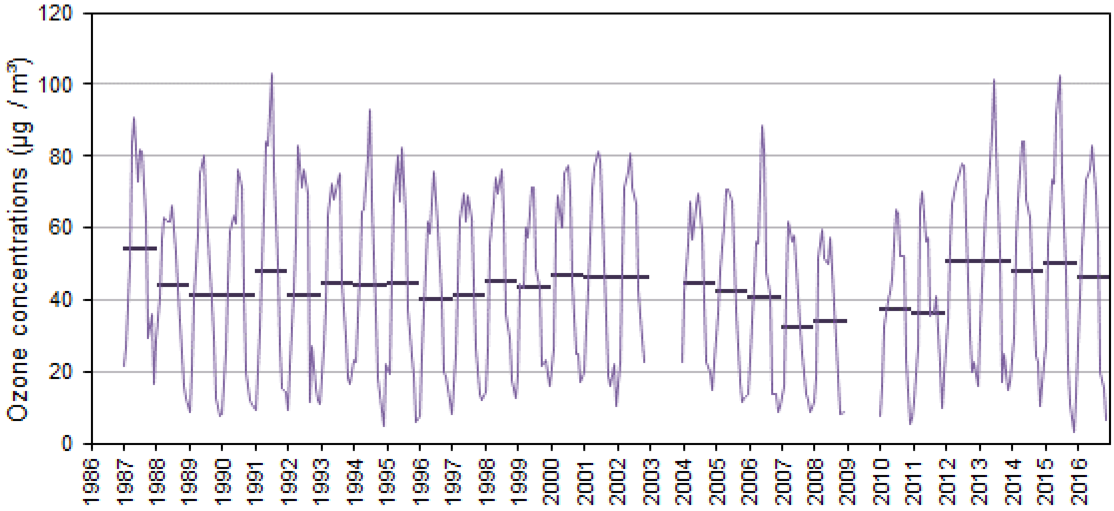

Fig. 49. Ozone yearly and monthly mean concentrations at JRC-Ispra.

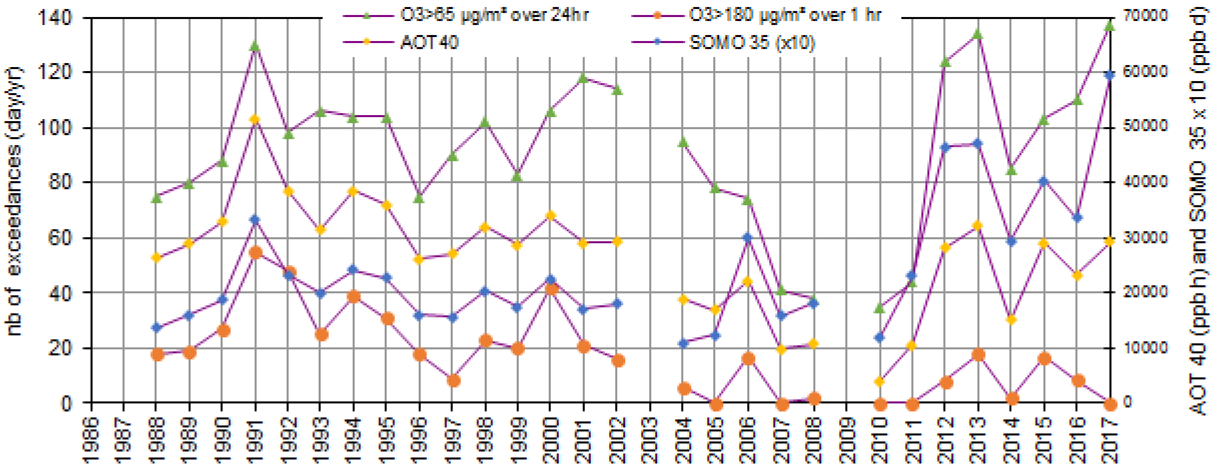

Fig. 50. AOT40, SOMO35 values, and number of O_3 *limit value exceedances.*

Despite relatively high concentrations in January, the annual mean concentration of NH_4^+ in particulate matter has remained similar to the average over the 5 past years in 2017 (Fig. 47), i.e. half that of the previous decade.

It should be noted that from the year 2002, NH_4^+ was measured in the PM_{10} or in the $PM_{2.5}$ fraction. From 2005 and onwards, NH_4^+ concentrations in PM_{10} were calculated as follows:

$$NH_4^+(PM_{10}) = NH_4^+(PM_{2.5}) \times \langle NH_4^+(PM_{10}) / NH_4^+(PM_{2.5}) \rangle$$

where the average $\langle NH_4^+(PM_{10}) / NH_4^+(PM_{2.5}) \rangle$ is calculated based on simultaneous PM_{10} and $PM_{2.5}$ measurements performed in 2010-2012. On average, NH_4^+ can neutralise nearly 100% of the acidity associated with NO_3^- and SO_4^{2-} in the particulate phase (see Fig. 29). NH_4^+ is also quite well correlated with $NO_3^- + SO_4^{2-}$ in rainwater. NH_4^+ annual wet deposition in 2017 was indeed very low, as for the other eutrophying and acidifying substances, and close to 20% less than the average recorded in Ispra over the 5 past years.

4.5.2 Particulate matter mass

The 2017 annual mean $PM_{2.5}$ concentration measured at 20% RH (15.5 µg/m³) was greater than in 2016, but less than in 2015. The annual value for PM_{10} at 50% RH estimated from $PM_{2.5}$ measurements is therefore in line with the general decreasing trend of - 1.0 $\mu g\ m^{-3}\ yr^{-1}$ over the 3 last decades (Fig. 48). It should however be kept in mind that PM_{10} concentrations were estimated from TSP mass concentration measurements (carried out by weighing at 60 % RH and 20 °C cellulose acetate filters sampled without any particle size cut-off and "dried" at 60 °C before and after sampling) over 1986-2000, based on a comparison between TSP and PM_{10} over the Oct. 2000 - Dec. 2001 period ($R^2 = 0.93$, slope = 0.85), and derived from measured $PM_{2.5}$ values for years 2005-2017. After the historical low winter concentrations observed in winter 2013 – 2014, winter concentrations have steadily increased in 2015, 2016, and 2017, at least partly due to the exceptionally dry Dec. 2015, Jan. and Dec 2016, and Jan. 2017. Summertime PM minima showed a robust decreasing trend over 1986 – 2010, and a more modest decreasing trend since the slight increase in 2011.

4.5.3 Ozone

Fig. 49 shows monthly and yearly mean O_3 concentrations observed since 1987. Ozone was not measured in 2009 and there was a major data acquisition breakdown in 2003. Annual average O_3 concentrations have been consistently high from 2012. In 2017, the annual mean O_3 concentration reached the 2nd highest record since the measurements started. This high annual average was due to high wintertime background values and only moderately high summer values. Indeed, ozone indicators for 2017 (Fig. 50) show a decrease in extreme O_3 pollution event frequency, but a large increase of the occurrence of concentrations greater than 30-40 ppb (60-80 µg/m³).

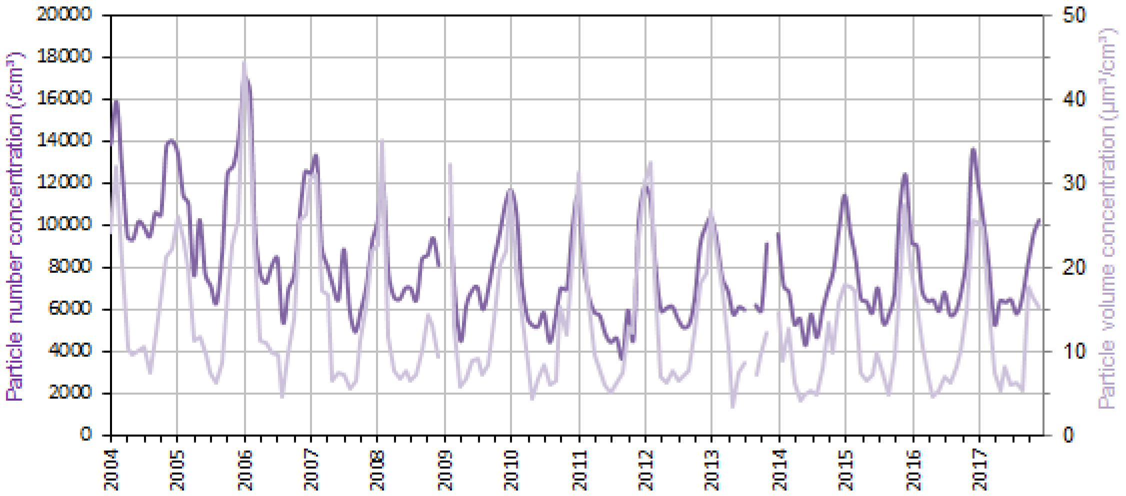

Fig. 51. Particle number (left) and volume (right) monthly mean concentrations.

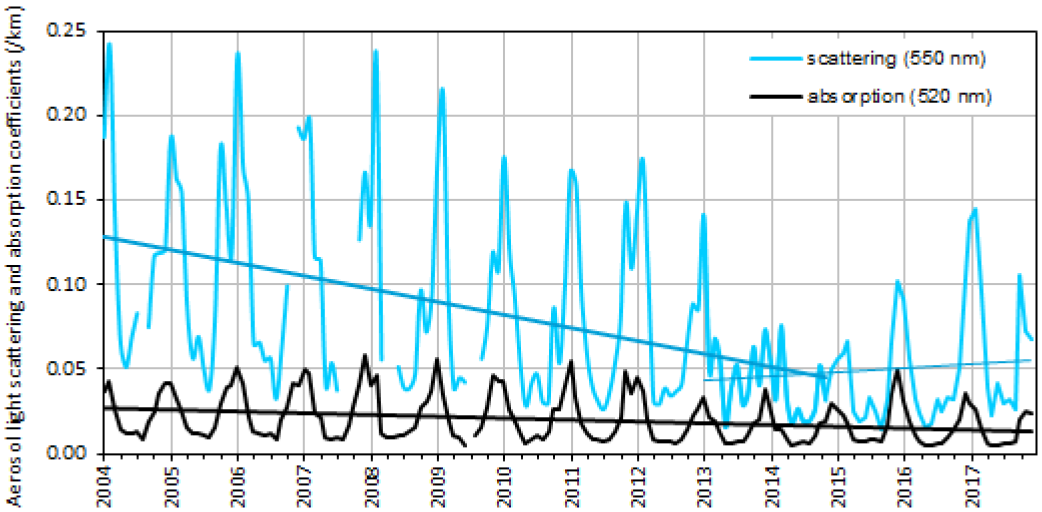

Fig. 52. Aerosol green light scattering and absorption monthly mean coefficients

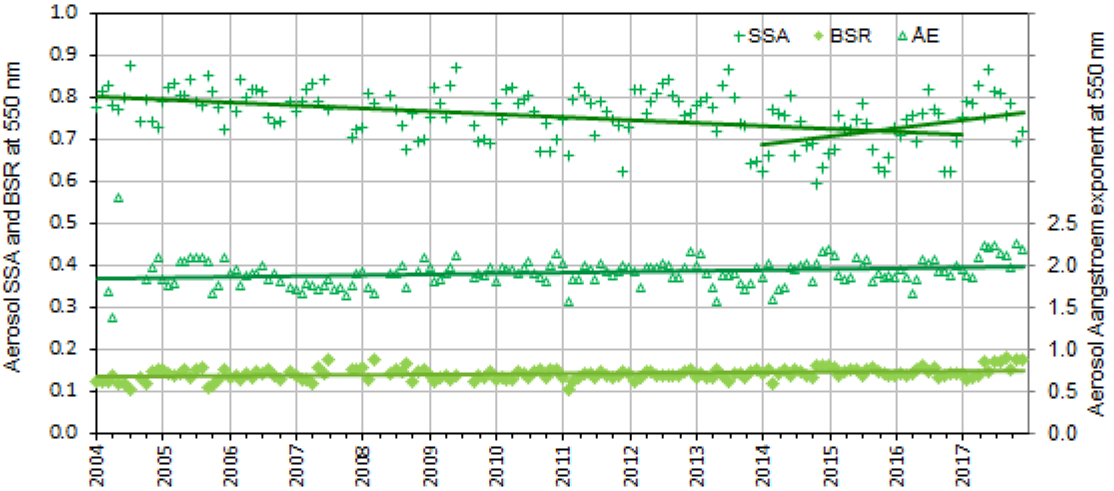

Fig. 53. Aerosol optical characteristics at 550 nm (monthly means): single scattering albedo and backscatter ration (left hand axis) and scattering Ångström exponent (right hand axis).

Both indicators for the vegetation protection (number of days with a 24-hour mean O_3 concentration > 65 µg/m³, vegetation protection limit, and the AOT40, Accumulated Ozone exposure over a Threshold of 40 ppb) have generally been increasing during the 2010's and now reached levels similar or greater than the values observed in the 1990's after the minimum observed in the 2000's. The population exposure indicator SOMO 35 (Sum of Ozone Means Over 35 ppb, where means stands for maximum 8-hour mean over day) was higher than ever in 2017. Only the number of days with extreme maximum O_3 concentrations (limit of 180 µg/m³ over 1hr exceeded) dropped (down to 0), as in the 2000's, showing a net improvement compared to the 1990's.

4.5.4 Aerosol micro-physical and optical properties

Measurements of aerosol microphysical properties started at the atmospheric research station of the JRC-Ispra in 2004, which represents one of the longest time series for this kind of measurements across Europe. These time series show a tipping point around year 2014.

After the decreasing trend observed in sub-µm aerosol particle number and volume concentrations observed between 2004 and 2011, the annual average of both variables have started to increase since 2014 (Fig. 51). While summertime minimum particle volume concentrations remain low, wintertime maximum as well as both wintertime and summer particle number concentrations are responsible for this increase.

These trends are reflected in the long-term variations of the aerosol light scattering coefficient (Fig. 52), which is sensitive to both the number and size of atmospheric particles. In contrast, the aerosol light absorption coefficient still decreases slowly, both in summer and winter. As a consequence, the aerosol single scattering albedo (SSA = scattering/(scattering + absorption)) significantly decreased between 2004 and 2015, and seems to be increasing since then. The Ångström exponent (which increases with decreasing particle diameters) has perhaps been increasing faster since 2015 (Fig. 53), but longer time series are needed to confirm this trend or not. The aerosol backscatter ratio on the other hand clearly increased in 2017 only. These variations are good for climate change mitigation since the impact of these recent changes is an increase of the direct cooling effect by atmospheric particles at the top of the atmosphere, in contrast to what we observed between 2004 and 2012 (Putaud et al., 2014).

4.6 Conclusions

Measurement of short-lived pollutants and climate forcers were carried out continuously in 2017 at 4.5 m agl at the provisional site until June, and at 9 m agl at the new atmospheric observatory (*Fig. 1*) from July 2017. However, gaseous pollutants were also monitored at the provisional site until December 2017. Data coverage ranged from 93 to 98% for the various instruments measuring near surface variables. The remote aerosol vertical profiler was operated for the whole year, weather and staff availability permitting, and covered more than 36% of the scheduled measurement slots.

2017 as a whole was warmer and sunnier compared to the reference period (1990 – 1999), specially from March to October , and very dry, particularly in January and October, which can probably explain at least partly the relatively high particulate and O_3 pollution levels observed in 2017 compared to the previous years.

The impact of the weather conditions on O_3 concentrations is difficult to quantify, but it is probably not sufficient to explain the high O_3 concentrations and exposure indicators observed in 2017, which further worsened in line with the trend observed since 2010, except for the frequency of extreme O_3 pollution events which dropped to low values compared to the early 1990's. In contrast, the annual mean concentrations of SO_2, NO_2 and CO were not much higher than during the previous years, and confirm the general trend of improvement in these air quality indicators over the last 3 decades.

Daily $PM_{2.5}$ aerosol sampling on quartz fibre filter through a carbon monolith denuder, and subsequent gravimetric and chemical analyses, showed that the concentration of $PM_{2.5}$ mass and of most of its components (SO_4^{2-}, NO_3^-, NH_4^+, POM and EC) slightly increased in 2017 compared to 2016, but remained similar to the values observed during the previous 5 years. $PM_{2.5}$ average chemical composition was dominated by carbonaceous species (POM: 46%, EC: 7%), followed by secondary inorganics (NH_4^+: 9%, NO_3^-: 14%, SO_4^{2-}: 15%). It is worth mentioning that in 2017 the unaccounted mass averaged 6%, excluding days where $PM_{2.5}$ concentration was less than 3 µg / m², for which uncertainties are too big. As previously observed, there was a clear increase of NO_3^- contribution to $PM_{2.5}$ when shifting from cleaner ($3 < PM_{2.5} < 10$ µg/m³) to more polluted periods ($PM_{2.5} > 25$ µg/m³) during both cold and warmer months. $PM_{2.5}$ (from gravimetric analyses at 20% RH) annual mean mass concentrations (16 µg/m³) was well below the EU annual limit value (25 µg/m³). In contrast, PM_{10} measurements performed with the FDMS-TEOM led to 43 exceedances of the daily limit value (50 µg/m³), while the annual average (29 µg/m³) stayed below the annual PM_{10} limit value (40 µg/m³). The long-term time series of PM concentrations still suggests a decreasing trend of -1.0 $\mu g\ m^{-3}\ yr^{-1}$ over the last 3 decades.

Particle number size distributions were in 2017, as usual, generally broadly bimodal, with a submicron mode at ca. 100 nm (dry) and a less pronounced coarse mode around 2 µm. The annual mean particle number concentration (average: 7900 cm^{-3}) was higher than in 2016 but lower than in (also dry) 2015. The 14-yr time series in particle size distribution highlight a striking feature: particle number and volume concentrations have decreased till 2011, but seem to increase since 2014. This changing trend is reflected in several other variables like the aerosol light scattering coefficient, and as a consequence, the aerosol single scattering albedo (0.78 in 2017 vs 0.72 in 2016 and 0.70 in 2015). It can also be observed in PM mass concentrations, for which wintertime maxima have also increased since 2014. Together with the O_3 pollution indicators, these observations suggest that a tipping point was reached in the trend of air pollution measured at the JRC-Ispra around 2014. It would be worth investigating if such a feature can be observed in the time series obtained at air monitoring stations in our area.

All the aerosol extensive variables measured at JRC-Ispra (at ground level) have similar seasonal variations with summer minima. These variables are generally well correlated and lead to variable degrees of chemical, physical, and optical closure. In 2017, a reasonable overlap between the particle size distributions as measured with the DMPS and the APS was obtained for a particle density ranging between 1.1 and 1.5 g/cm^3. These values are reasonably consistent with the average sub-2.5 µm aerosol density of 1.13 g/cm^3 determined from the regression between the gravimetric $PM_{2.5}$ mass and the DMPS + APS volume. However, such a density is low compared to literature values (1.6 ±0.1), and is also low compared to 2010 - 2012 values (1.3 – 1.4 g/cm^3). In contrast, the ratio between the PM_{10} mass concentration measured with the FDMS-TEOM and the aerosol volume DMPS + APS volume leads to a density of 1.5 g/cm^3. It is unlikely that the density of PM_{10} and $PM_{2.5}$ are so different from each other. This difference might indicate a systematic bias in one of these measurements in 2017. Similarly, the mean mass extinction cross section (i.e., the extinction-to-mass ratio) of 2.7 to 3.1 m^2 g^{-1} (depending on the measurements used to calculate this variable) obtained in 2017 is low compared to the value that can be calculated from the mean $PM_{2.5}$ chemical composition (4.7 m^2 g^{-1}), which suggests that either the aerosol volume and PM_{10} concentrations were overestimated, or the extinction coefficient calculated as scattering + absorption was underestimated. The measurement of light scattering and absorption by atmospheric particles remain challenging and prone to uncertainties. A direct measurement of the aerosol light extinction would be very useful to address this issue.
Aerosol vertical profiles were obtained with the Raymetrics Raman LiDAR for the whole of 2017. Mainly due to unsuitable meteorological conditions and staff unavailability, only 36% of the profiles scheduled by ACTRIS could be measured. Data have been successfully processed using the ACTRIS Single Calculus Chain and valid optical products have been submitted to the ACTRIS/EARLINET. Specific characterisations of the LiDAR optics are needed before the whole of the data obtained in 2017 can be processed

The concentrations of the ions measured in rainwater (Cl^-, NO_3^-, SO_4^{2-}, Na^+, NH_4^+, K^+, Mg^{2+}, and Ca^{2+}) were in 2017 all greater than in 2016, but the amount of precipitation was exceptionally low (804 mm) so that the annual wet deposition fluxes of the main acidifying and eutrophying species (1.4, 3.0, and 1.5 g m^{-2} for SO_4^{2-}, NO_3^-, and NH_4^+, respectively) were amongst the 3 lowest records observed during the past 30 years. In contrast, only 8 rain samples with pH<4.6 (i.e. 10 times more acidic than due to the equilibrium with atmospheric CO_2) were observed in 2017, compared to 3 in 2016. Rainwater acidity has hover drastically dropped over the past 3 decades.

Ground-level 2017' data listed by EMEP and ACTRIS as core variables have all been reported to EBAS by May 2018, as requested by these programmes. They can be freely downloaded from these data centres.

Fig. 54: the flux tower of 24 m at the Pinus pinea site in San Rossore

5. Atmosphere – Biosphere flux monitoring at the forest station of San Rossore

5.1 Location and site description

The measurement site 'San Rossore' (43°43.9205′N, 10°17.45817E, 4 m a.s.l.), operated by the Air and Climate Unit, is located in the Parco San Rossore (www.parcosanrossore.org), approximately 9 km west of Pisa and 1200 m east of the seashore in a Mediterranean forest ecosystem (seeFig. 54).

The Climate Change and Air Quality Unit began to operate the predecessor site in the Parco San Rossore site in 1999; the present location is running since 2013.

The measurement site is situated in an almost flat area with a morphology characterised by the presence of sandy dunes. The vegetation in the direct vicinity is a pinewood established in 1921 following artificial seeding and it is dominated by the evergreen tree Pinus pinea with very sparse Quercus ilex. The average canopy height is approximately 19 m whereas the needles start at about 16.5 m. The understory vegetation is confined to the forest edges and canopy gaps and very sparse.

The area has a Mediterranean – type climate within the sub-humid zone, with a mean annual rainfall of 876 mm yr^{-1} and a range of 534 – 1270 mm for the period 1980 – 2005. The long-term data were obtained from a meteorological station located at a distance of approximately 10 km and managed by the Regional Hydrologic Service of Tuscany. Rain falls mainly during autumn and winter with about 50% occurring between September and November, while the driest months are July and August. The average annual temperature is approximately 14.2 °C with the average temperature of the coldest month (January) being 7 °C and that one of the warmest month (August) being 25 °C. The wind regime is characterized by a sea – land breeze circulation, i.e. the air flows quite predictable from the west (sea) during day and from east (land) during night.

The scientific activities at the site are embedded into the ICOS initiative. ICOS (Integrated Carbon Observation System, www.icos-ri.eu) is one of the pan-European research infrastructure projects identified by the European Strategy Forum on Research Infrastructures (ESFRI) for implementation. After its preparatory phase planned for 2008 until 2013 with an extension towards 2015, during which monitoring infrastructure and technical procedures are developed, its operational phase will run for 20 years from 2016 onwards.

Table 7: ICOS class 2 Ecosystem Station core parameters.

Core variables continuous	**Core variables daily to monthly**	**Core variables yearly**
CO_2, H_2O and energy fluxes	leaf area index	biomass (above ground)
wind speed and direction		soil carbon
CO_2 concentration vertical profile, normal precision		stem diameter
net radiation: • incoming/reflected global radiation • incoming/outgoing longwave radiation • Albedo		above-ground Net Primary Production (NPP)
diffuse global radiation		litter fall
incoming / reflected under canopy Photosynthetic Active Radiation (PAR)		land-use history
temperature and relative humidity vertical profile		managements and natural disturbances
air pressure		C and N import and export on managed sites
precipitation, through-fall, snow depth		
soil heat flux		
ground water level		
soil temperature profile		
water content profile		

Table 8: ICOS variables measured continuously during 2017 in San Rossore

FLUXES	CO_2, latent heat, sensible heat
METEOROLOGY	3D wind speed, temperature, relative humidity, pressure, precipitation
RADIATION	short & long wave incoming & outgoing, direct & diffuse photosynthetic active radiation
SOIL	temperature profile, water content profile, heat flux, water table height

Once in operational mode, greenhouse gas concentrations and fluxes will be monitored on a routine basis following a very strict quality controlled protocol, both in terms of measurement instrumentations required to be used and procedures to be followed. The JRC plans to contribute with a class 2 Atmospheric Station (AS) for the high precision monitoring of greenhouse gas concentrations and a class 2 Ecosystem Stations (ES), the San Rossore forest flux tower, for the monitoring of ecosystem fluxes. Class 2 stations provide data for less parameter compared to class 1 stations and thus require less investment for instrumentation and have lower running costs in terms of instruments and staff. The mandatory variables to be monitored at the class 2 Ecosystem Station are shown in Table 7.

With regards to data reporting, as in the previous years, quality checked data for 2017 have been submitted for the measurement site under the station name IT-SR2 to the Fluxnet database at the European Fluxes Database Cluster at www.europe-fluxdata.eu.

5.2 Measurements in 2017

Despite being still in the upgrading phase of the measurement site to comply with ICOS class 2 requirements, the monitoring programme at the new Pinus pinea site continued well. The main parameters measured are summarised in Table 8.

Fluxes of CO_2, H_2O and sensible heat were measured with the eddy covariance technique using EddyMeas (Olaf Kolle, www.bgc-jena.mpg.de) for data acquisition and evaluated with the EdiRe software package from the University of Edinburgh (www.geos.ed.ac.uk/abs/research/micromet). The ancillary parameters (meteorology, radiation and soil) were obtained with their respective sensors and the data quality checked for instrument malfunctioning, obvious outliers and consistency. In the following chapters, the instruments used are described and then daily averages of the different parameters measured during the course of 2017 are presented.

5.3 Description of the instruments

5.3.1 Infrastructural

5.3.1.1 Sensor location

The instruments for eddy covariance flux system, i.e. sonic anemometer and fast gas analyser, solar radiation and meteorological parameters are mounted on the top of the guided wire tower at a height of 24 m above ground, 5 m above the canopy top at 19 m.

Soil parameters are measured at an undisturbed soil plot approximately 20 m west of the tower.

A wooden hut complements the installation hosting IT and communication equipment, a UPS system and is also used for storage.

5.3.1.2 Data acquisition

Eddy covariance flux data are stored with high frequency, i.e. 10 Hz, as chunks of 30 minutes on a local laptop connected to the sonic anemometer. Data from the sensors located on the tower top are read every 10 s and averaged and stored every 30 minutes by a CR3000 data logger from Campbell (www.campbellsci.co.uk) also installed on the tower top. Soil measurements are handled the very same way by a CR3000 installed on the ground.

For eddy covariance flux data, the start time of every 30 minutes measurement period is saved as the reference time, whereas for all other data, the end of the 30 minutes measuring period is used. The time reference used for all San Rossore measurements is has been changed in October 2015 to local solar time (UTC+1) to comply with ICOS requirements.

5.3.1.3 Power supply, IT & communication infrastructure

The fixed line power supply of approx. 4 kW is locally backed up by an UPS system MSM 10 from Riello (www.riello-ups.de) to protect the system for transient power outages and provide an autonomous running time of approx. 19 hours for the installation. Computers and data loggers are connected via a local TCP/IP network. In addition, a cellular router TK704U from Welotec (www.welotec.com) provides internet access via the mobile 3G network. For safety reason at the remote site, a 3G repeater provides mobile phone coverage also on the forest ground in the vicinity of the site.

Measurement data is automatically transferred from San Rossore via ftp to a server (sanrosso@ftp-ccu.jrc.it) in Ispra at 6:00 local solar time. Remote connection to a computer at the site can be established as well.

5.3.2 Ecosystem fluxes

5.3.2.1 Sonic Anemometer for 3D wind direction Gill HS-50

Sonic anemometers determine the three-dimensional wind vectors at high frequency using the speed of sound. The Gill HS-50 (www.gill.co.uk) emits ultrasonic pulses between its pairs of transducers, measures the flight time of the pulses to the paired transducer and calculates the wind speed in the direction of the transducer pair (see Fig. 55). Combining the results from the three transducer pairs, the 3-dimensional wind speed is calculated at a frequency of 10 Hertz. After a rotation of the coordinate system during the data processing to align it with the north direction, horizontal and vertical wind speeds and the wind direction are calculated besides their use for flux calculations. As the speed of sound measured with the anemometer depends on the temperature, the so-called sonic temperature is reported by the instrument as well.

Due to the absence of moving parts and the fact that no calibration is required, the instrument is very robust and reliable. Instrument servicing is done at the manufacturer.

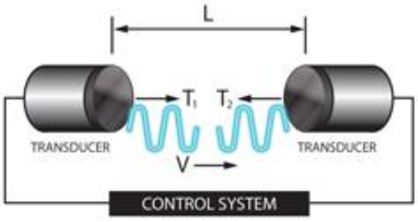

$$T_2 = \frac{L}{C - V} \quad \text{and} \quad T_1 = \frac{L}{C + V}$$

therefore

$$V = \frac{L}{2}\left\{\frac{1}{T_1} - \frac{1}{T_2}\right\} \qquad C = \frac{L}{2}\left\{\frac{1}{T_1} + \frac{1}{T_2}\right\}$$

Fig. 55: Measurement principle of sonic anemometers, sketch from www.gill.co.uk (T: travelling time of sound pulses, L: distance between transducers, C: speed of sound, V: wind speed in direction of transducers)

5.3.2.2 Fast infrared gas analyser (IRGA) for CO_2 & H_2O concentration LI-7200 FM from Licor

For the determination of CO_2 and H_2O fluxes with the eddy covariance technique, fast analysers (10 to 20 Hertz) for concentration measurements of the gases of interest are obligatory. At the San Rossore forest flux tower, a LI-7200 FM system from LI-COR (www.licor.com) has been installed, consisting of the LI-7200 enclosed CO_2/ H_2O analyser, the LI-7550 analyser interface unit and the LI-7200-101 flow module.

The LI-7200 is a high performance, non-dispersive, enclosed open path infrared CO_2/H_2O analyser based on the infrared absorption of CO_2 and H_2O at ambient conditions that provides concentration measurements at a frequency of up to 20 Hertz. With the flow module, ambient air is drawn into to analyser through the sample inlet at a set flow rate of 15 l/min. In the sample volume of 16.09 cm^3 (see Fig. 57), light from the infrared source is absorbed at characteristic wavelengths for CO_2 and H_2O. This specific absorption is a function of the gas concentration in the sample volume. Using the absorption measurements at the CO_2 & H_2O wavelengths, at a non-absorbing wavelength plus calibration factors and measured temperature and pressure, the LI-7200 reports molar densities, mass densities or mole fraction of the two gases.

Zero and span checks and calibrations are done regularly using zero gas from a cylinder plus a dew point generator (RH CAL from EdgeTech) and a CO_2 standard from a cylinder.

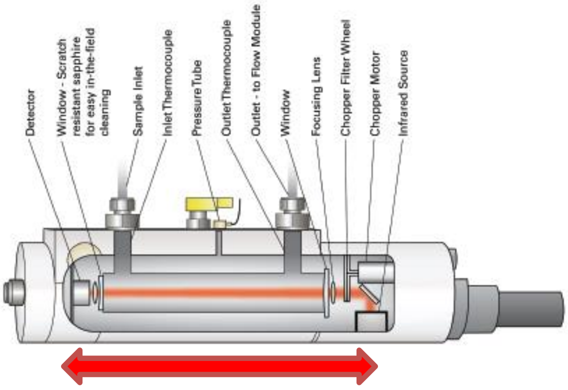

Fig. 56: LI-7200 analyser head (from www.licor.com), arrow indicates sampling volume

5.3.3 Radiation instruments

5.3.3.1 Net radiometer Kipp & Zonen CNR4

The net radiometers CNR 4 from Kipp & Zonen (www.kippzonen.com) measures the energy balance between incoming and reflected radiation in the short (305 – 2800 nm) and long (5-50 µm) wavelength range to obtain the net radiation at the earth's surface. The short wavelength range is measured with two CM3 pyranometers, one facing upwards and one downwards. For the long range, two CG3 pyrgeometers facing opposite directions are used. The design of the instrument ensures a field of view of 180° upwards and downwards for the respective sensors. The CNR 4 features a blower and heating system to minimize the influence of dew and frost on the radiation measurements.

The energy E_{short} of the short wave or so-called global (solar) radiation is calculated from the voltages provided by the CM3's using their sensitivity C_{CM3}: $E_{short} = V / C_{CM3}$. To calculate the energy E_{long} of the long wave radiation from the reported voltages, besides the sensitivities of the CG3's C_{CG3}, also the sensor temperature T measured with a PT-100 is needed: $E_{long} = V / C_{CG3} + 5.67 \cdot 10^{-8} \cdot T^4$. The net radiation over all wavelengths is then easily calculated by adding the respective energies: $E_{net} = E_{short}^{up} + E_{long}^{up} - E_{short}^{down} - E_{long}^{down}$. In addition, the Albedo of the earth's surface defined as the ratio of outgoing to incoming solar radiation can be obtained with the instrument as well: $Albedo = E_{short}^{downt} / E_{short}^{up}$.

Calibration and instrument checks at the factory are recommended every two years according to the manufacturer.

5.3.3.2 Photosynthetic active radiation Delta-T BF5

With the Sunshine Sensor BF3 from Delta-T (www.delta-t.co.uk), total (in the sense of direct plus diffuse) solar radiation, diffuse radiation and the sunshine state is measured as photosynthetic active radiation (PAR) of the solar spectrum, i.e. from 400-700 nm. To distinguish between direct and diffuse radiation, a set of seven photodiodes (PD) is arranged under a patterned hemispherical dome with 50% black bands such that at any position of the sun in the sky at least one photodiode is completely in the shade and at least one is fully exposed to direct sunlight. This design eliminates the necessity of frequent alignment of the shading parts to the position of the sun. The diffuse radiation is then given by $PAR_{diffuse} = 2 \cdot PD_{\min}$ and the direct radiation by $PAR_{direct} = PD_{\max} - PD_{\min}$

The instrument reports $PAR_{diffuse}$, $PAR_{total} = PAR_{diffuse} + PAR_{direct}$ and sunshine state. The latter one indicates sunshine if

$$PAR_{total} / PAR_{diffuse} > 1.25 \text{ and } PAR_{total} > 50\ \mu mol \cdot m^{-2} \cdot s^{-1} .$$

5.3.4 Meteorological sensors

5.3.4.1 Temperature & relative humidity UMS KPK1/5-ME

To measure ambient temperature and relative humidity, a combined sensor KPK1/5-ME from UMS (www.ums-muc.de) is installed into a passive radiation shield.

5.3.4.2 Ambient air pressure Keller Druckmesstechnik PAA-41

Ambient air pressure is measured with a PAA-41 capacitive pressure sensor from Keller Druckmesstechnik (www.keller-druck.com) using a ceramic measurement cell for enhanced reliability.

5.3.4.3 Rain sensor UMS ARG 100/std

The ARG 100/std from UMS (www.ums-muc.de) is a tipping bucket type of rain gauge. It features a collecting funnel with a surface area of 500 cm^2 and a resulting resolution of 0.2 mm of rain fall per tip.

5.3.5 Soil instruments

5.3.5.1 Soil heat flux sensors HFP01 from Hukseflux

Three thermal sensors HFP01 from Hukseflux (www.hukseflux.com) have been buried ten centimetres underground in the undisturbed soil around the tower to obtain a good spatial averaging of the soil heat flux. The determination of the heat flux is based on measuring the temperature difference of two sides of a plate that is exposed to a heat flow using a number of thermocouples connected in series (see Fig. 57) with the convention that positive values indicate a heat flux into the soil, a negative one heat flux out of the soil. Ignoring possible errors, the temperature difference between the hot and cold side of the sensor is proportional to the heat flow. As the thermocouples provide a voltage proportional to the temperature, the voltage output of the sensor is proportional to the heat flow across the sensor.

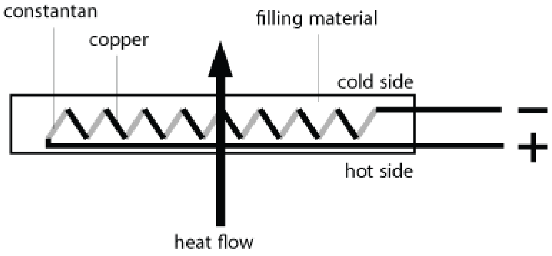

Fig. 57: Sketch of a soil heat flux sensor (drawing from www.wikipedia.org)

5.3.5.2 Soil water content vertical profile with TRIME-TDR from IMKO

Profile measurements of soil water content are performed using the TRIME-TDR (Time domain Reflectometry with Intelligent MicroElements with) from IMKO (www.imko.de). Based on Time-Domain-Reflectometry, the sensor generates high frequency electromagnetic pulses that propagate along a wave guide and reflect back into the sensor. Depending on the dielectric constant of the material surrounding the waveguide, the round trip time of the hf-pulses varies between some tens and thousand picoseconds. As the dielectric constant of soil and thus the round trip time strongly depends on the soil moisture content, measuring this time gives the water content of the soil surrounding the sensor. Burying several sensors at depths of 5, 30, 50, 100 cm below ground provides the soil humidity profile.

5.3.5.3 Soil temperature profile with Th3-v probe from UMS

For the measurement of soil temperatures at different depths, a Th3-v probe from UMS (www.ums-muc.de) is used. This probe features a convenient set of 6 temperature probes in a profile system buried at 5, 10, 20, 30, 50 and 100 cm below ground.

5.3.5.4 Ground water level CS456-SA from Campbell Scientific

The ground water level is monitored with a Diver from Campbell Scientific (www.campbellsci.co.uk). The device is placed in a water filled hole, 1.9 m below ground, and logs autonomously the pressure. Combining the measurement with the barometric pressure at the site gives the height of the water column above the sensor. Together with the known sensor depth below ground, the water table height can be easily calculated (see also Fig. 58):

$$WL = TOC - CL - WC \text{ with } WC = 9806.65 \cdot {(p_{Diver} - p_{baro})}/{\rho \cdot g};$$

g = 9.81 m/s^2, ρ = 1.00 kg/m^3

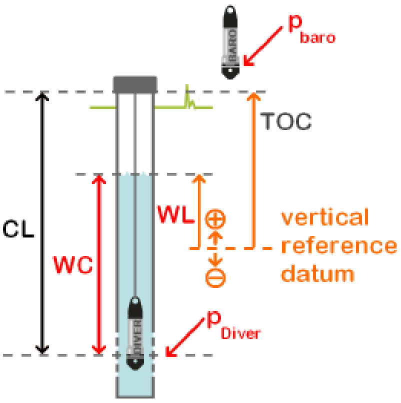

Fig. 58: Principle of water level calculation using the Diver (sketch from www.swstechnology.com). CL: cable length, TOC: top of container, WC: water column, WL: water level relative to a reference, p: pressure.

Table 9: Processing steps for flux calculations using the EdiRe Software package.

EdiRe Process	**brief description**
Preprocessed Files	data from input file, gas concentrations as molar densities
Extract	all high speed data
Despike	all high speed data
Linear	conversion of raw data from voltages into physical variables
1 chn statistics	averages of 3D wind, sonic temperature and gas concentration
Gas conversion	conversion of molar densities to molar fraction
Filter – detrend	linear detrending of gas concentrations
Wind direction	align with geographic direction
Rotation coefficients	perform 3D coordinate rotation
Cross Correlate	gas concentrations with vertical wind speed
Remove Lag	remove time lag between anemometer and gas analyser
Friction Velocity	calculate u*
Sensible heat flux coefficient	
Latent heat of evaporation	
2 chn statistics	calculate covariances, i.e. uncorrected fluxes
Sonic T - heat flux correction	
Stability - Monin Obhukov	calculate z/L stability parameter
Frequency response	calculate high frequency correction for all fluxes
Webb correction	calculate water density fluctuation correction for all fluxes
Stationarity	perform stationarity test
Integral Turbulence	calculate integral turbulence
Cospectra	calculate co-spectra for all fluxes
Storage	calculate storage term
User defined	determine quality flag (0,1,2) for all flux data according to Carboeurope methodology

5.3.6 Flux data processing

Data evaluation for flux data is done using the free EdiRe software package developed at the micrometeorology group from the University of Edinburgh. (www.geos.ed.ac.uk/abs/research/micromet/EdiRe/). As input data, EdiRe uses the 30 min raw flux data files in the binary *.slt format plus 30 minute averaged pressure, temperature and relative humidity data in ASCII format. As time convention, the start of the measurement period has to be assigned to the input data, the middle of the measurement period is assigned to the output data.

The main processing steps used within EdiRe to arrive at final, 30 minute averaged flux data that are corrected for various effects are listed in Table 9. In order to obtain budgets from e.g. annual datasets that unavoidably contain gaps in the data, a gap filling procedure must be established to calculate the missing values based on drivers for the respective parameter. In addition, partitioning of the measured CO_2 flux (that is the Net Ecosystem Exchange, NEE), into Gross Primary Production (GPP, the gross carbon uptake) and respiration of the Ecosystem (Reco) enables a better understanding of the underlying ecosystem exchange processes. Gap-filling and partitioning of the data is done with the online tool at: www.bgc-jena.mpg.de/bgi/index.php/Services/REddyProcWeb.

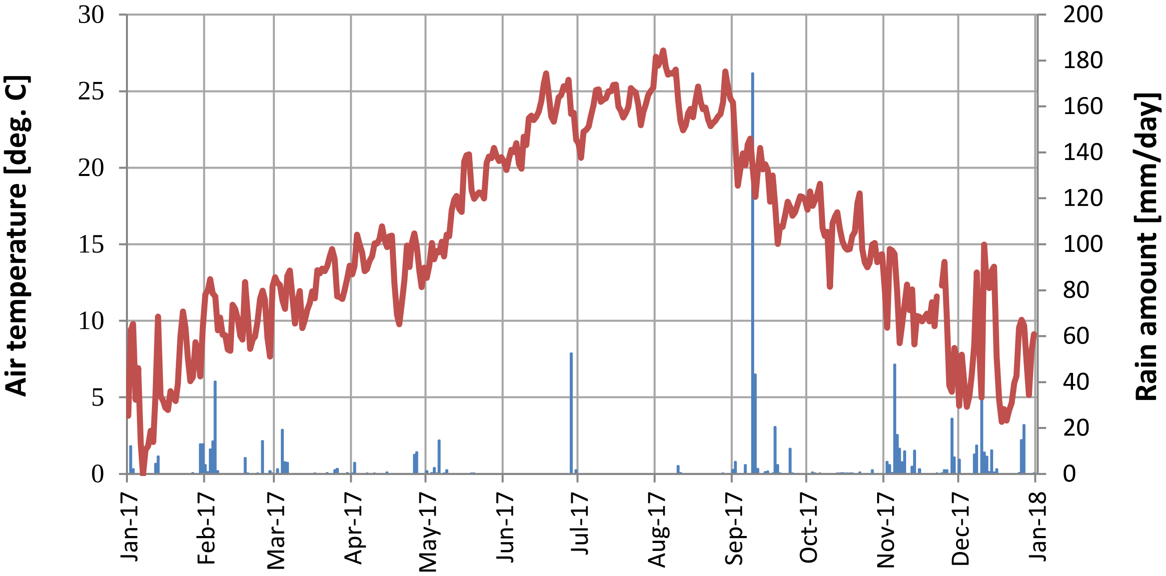

Fig. 59: Daily averages of air temperature (left) and daily sum of precipitation (right) as measured in the Parco San Rossore.

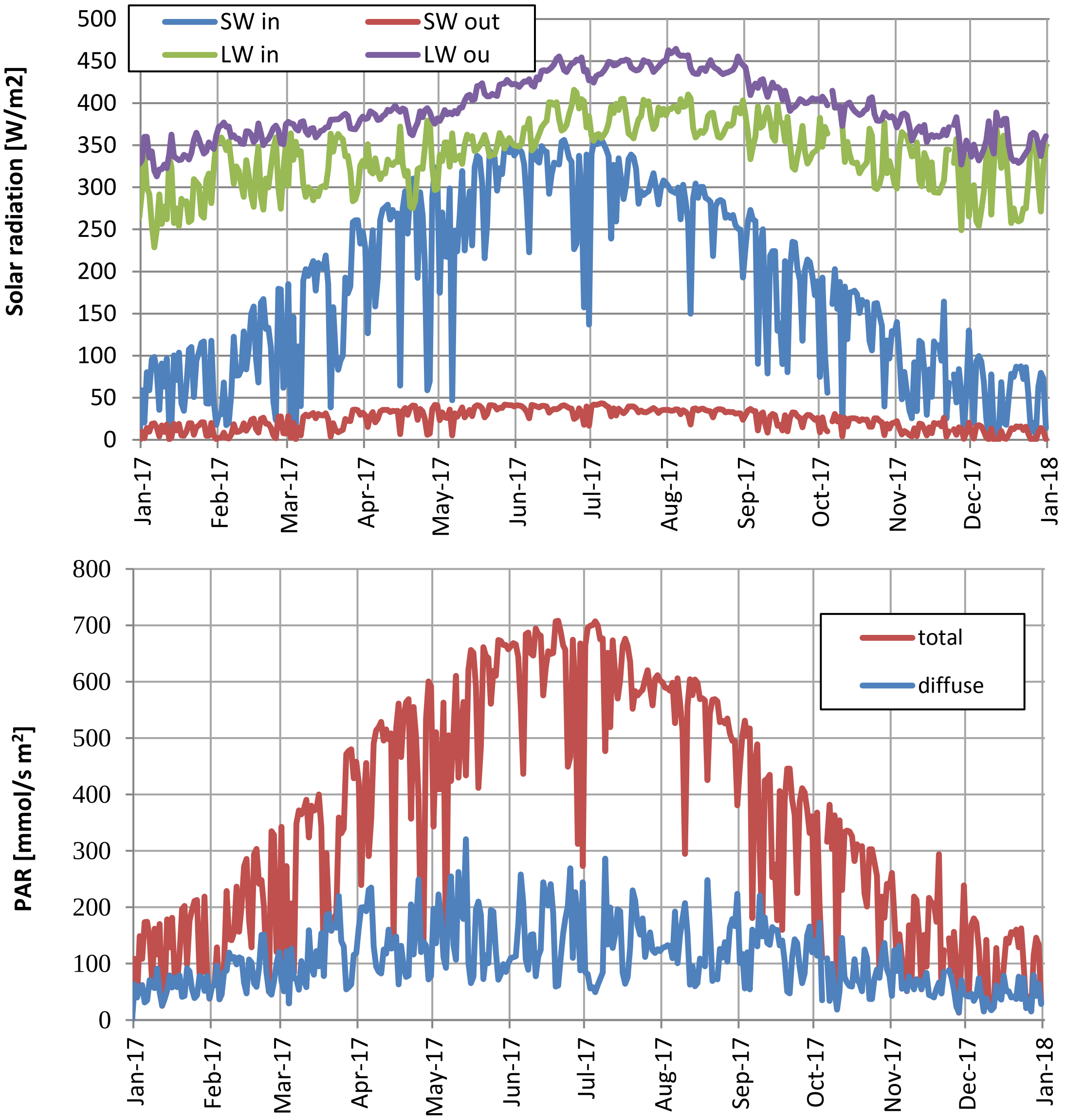

Fig. 60: Daily averages of short wave incoming radiation (top) and incoming photosynthetic active radiation (bottom).

5.4 Results of the year 2017

5.4.1 Meteorology

Daily averages for the annual cycle of air temperature and precipitation are shown in Fig. 59. The annual mean temperature for 2017 was 15.5° C (15.6° C for 2016), 1.3° C above the long-term average of 14.2° C. With a total measured rainfall of 848 mm (1123 mm in 2016), 2017 was an average year for San Rossore with a mean annual rainfall of 876 mm yr^{-1}. Similarly, 2017 was an average year regarding rainfall pattern, with most precipitation in spring / autumn and a rather long, dry period during summer.

The predominant sea – land breeze wind circulation can be seen from the statistical evaluation of the 3D wind direction measurements and is shown in Fig. 61. The red plot shows the frequency distribution of the wind for winds speed > 0.5 m/s in terms of its origins; the blue line indicates the average wind speed per directional bin. The average annual wind speed was 1.6 m/s.

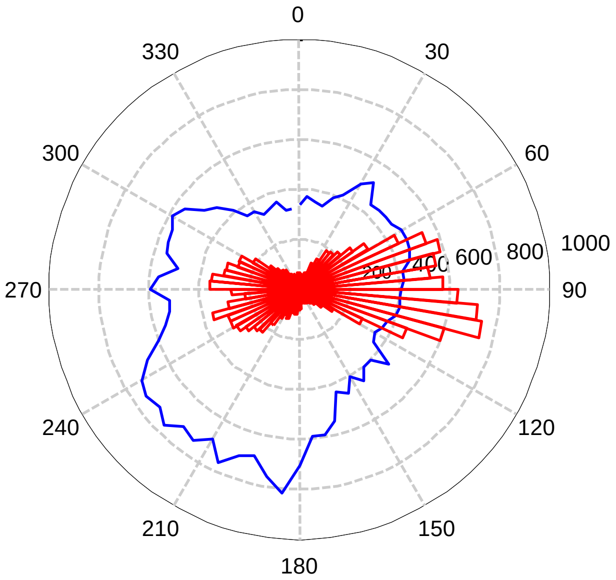

Fig. 61: Wind rose for 30 min. averages of wind measurements with wind speed >0.5 m/s. Red: directions of the wind origin, blue: average wind speeds per direction interval in a.u.

5.4.2 Radiation

In Fig. 60, the annual cycle of short & long wavelength incoming & outgoing radiation are plotted as measured with the CNR 4 net radiometer above the forest canopy at 24 m.

The surface albedo, i.e. the ratio between SWout and SWin (305 – 2800 nm) averages to approximately 0.12 for the summer period and 0.14 for the winter period of the measurement. On the bottom part of Fig. 60, the photosynthetic active radiation (PAR) part of the solar spectrum (approx. 400 – 700 nm) is shown as total and diffuse incoming radiation.

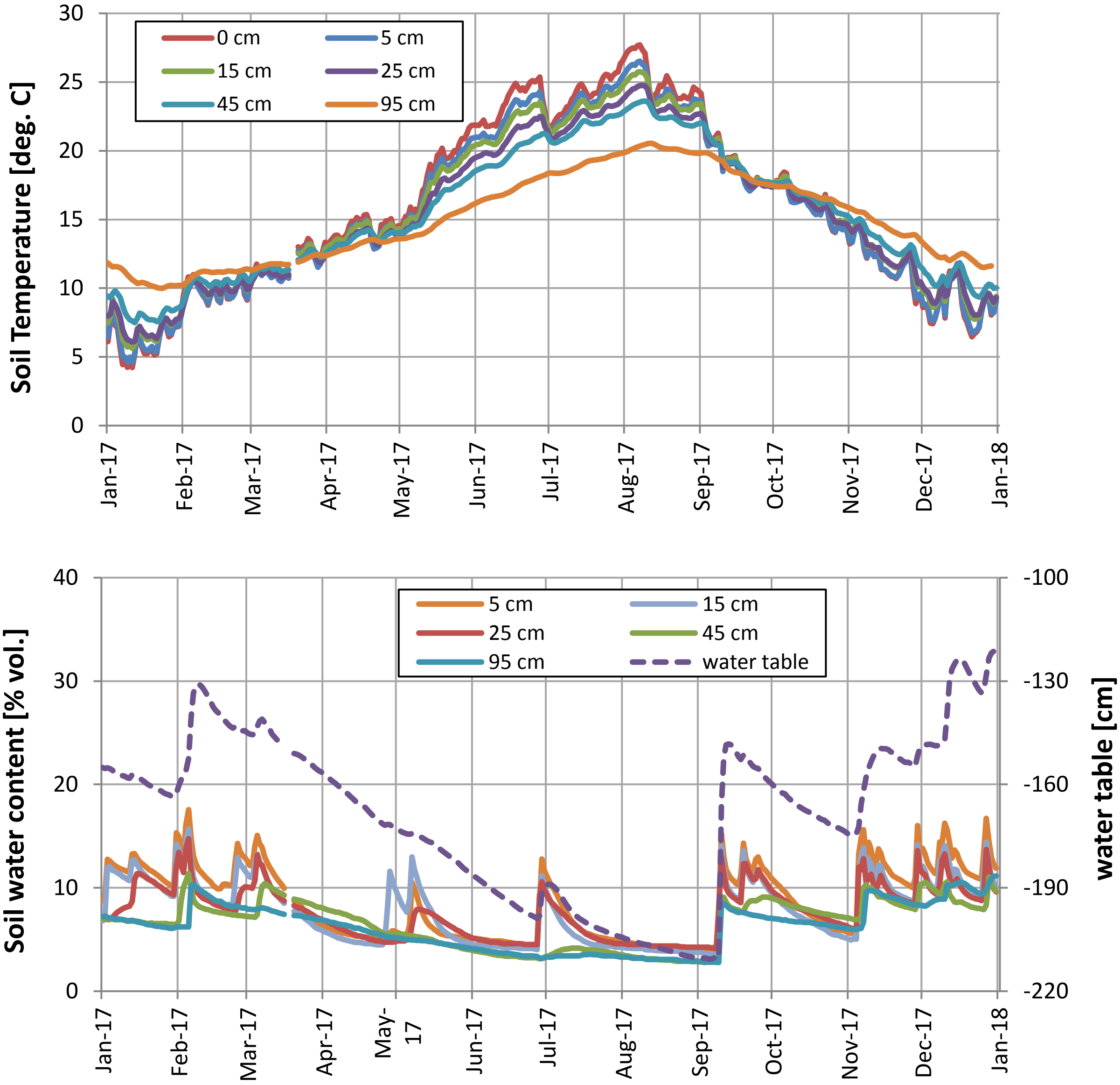

Fig. 62: Profiles of soil temperature (top) and soil water content plus water table (bottom) measured as daily averages.

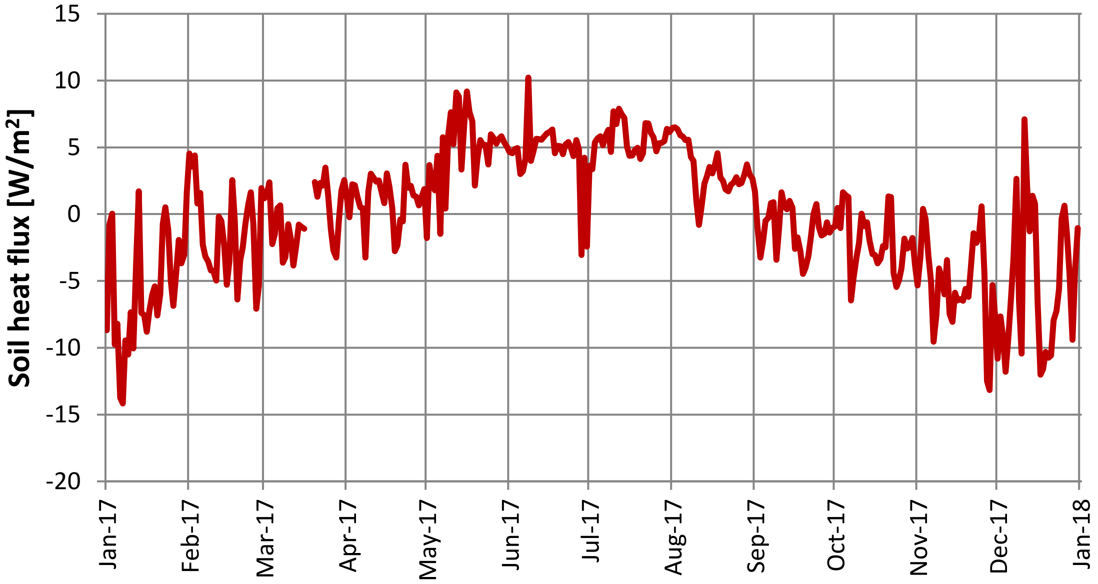

Fig. 63: Soil heat fluxes measured with three identical sensors located some meters apart.

5.4.3 Soil variables

Soil parameters monitored in 2017 were the temperature at six different depths 0, 5, 15, 25, 45 and 95 cm relative to the transition of the top organic layer and mineral soil at approx. 5 cm below surface, soil water content profile (5 cm, 15, 25, 45 and 95 cm), soil heat flux at 5 cm (using the convention that positive values indicate a heat flux into the soil, negative values out of the soil) plus water table depths measured with a well requiring a minimum water level of 260 cm below ground. The daily averages of these measurements are illustrated in Fig. 62 and Fig. 63.

5.4.4 Eddy covariance flux measurements

The daily averages of CO_2 and heat fluxes measured during 2017 are shown in Fig. 64 and Fig. 65, respectively. To obtain the eddy covariance flux data for the 30 minute measurement periods, the high frequency data from the LiCor 7200 infrared gas analyser for CO_2 and H_2O have been evaluated together with the anemometer data using the EdiRe software package from the University of Edinburgh.

The Carboeurope quality classification for the flux data points for 2017 is used also at San Rossore. A value of 0 indicates strong turbulence and good stationarity, giving reliable EC flux values. A QF = 1 indicates acceptable quality and flux data with QF = 2 are unreliable and thus should not be used in further calculations. For the measurements at San Rossore, the distribution of quality flags for all flux data are given in Table 10, which shows that 62 – 78 % of the data depending on the flux type are usable for further data evaluation and interpretation.

Table 10: Total number of flux data points and percentage of data points with quality flags according to the Carboeurope methodology (H: sensible heat, LE latent heat, FC CO_2 flux).

	H [%]	LE [%]	FC [%]
data points	17489	17489	17489
QF = 0	17	6	13
QF = 1	61	56	59
QF = 2	22	38	28

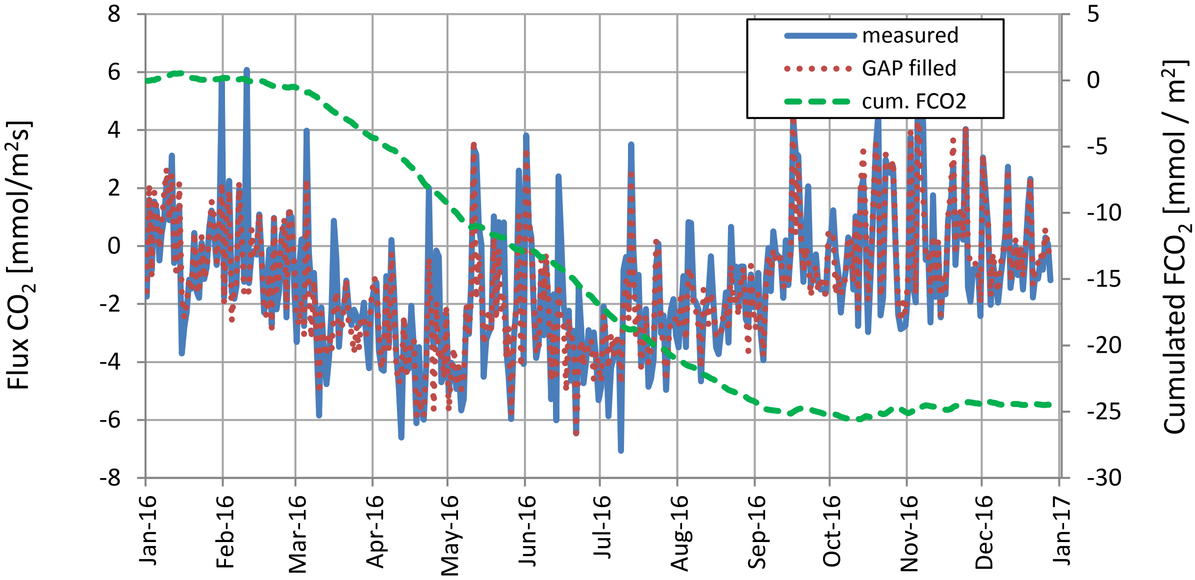

Fig. 64: Daily averages of measured (blue), gap filled (red) and cumulated (green) CO₂ fluxes.

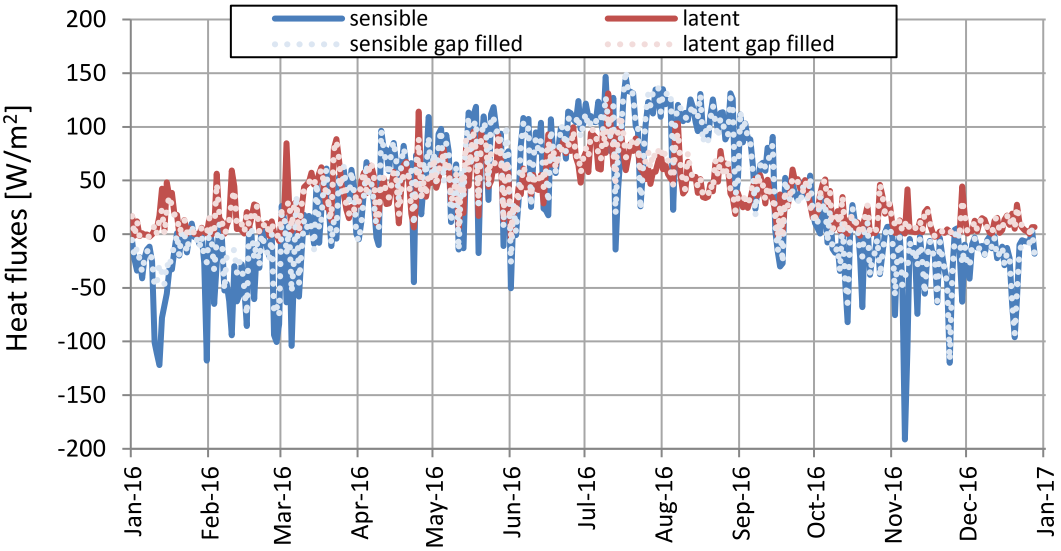

Fig. 65: Daily averages of latent (red) and sensible (blue) heat fluxes.

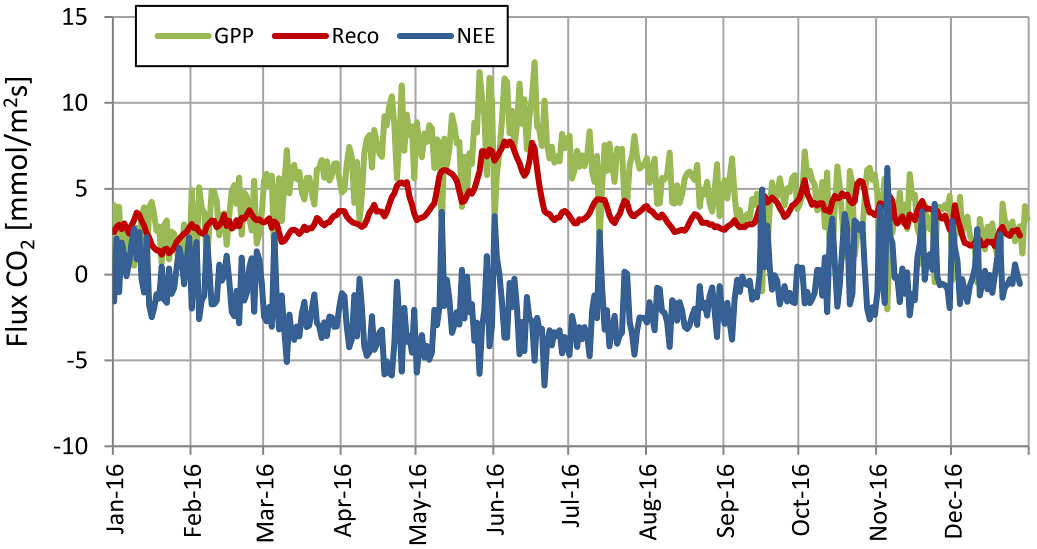

Fig. 66: Daily averages of NEE, GPP and Reco.

Gap filling of the dataset has been performed without filtering for friction velocities (u*) below a threshold (that would indicate how turbulent the wind is) using the 'Eddy covariance gap-filling & flux-partitioning tool' online available at: www.bgc-jena.mpg.de/~MDIwork/eddyproc/ for missing and quality class 2 data. The cumulated sum of the gap filled 30 min CO_2 fluxes is shown in Fig. 66. The plot shows that in 2017 the Pinus pinea stand is a clear sink for CO_2 from February until October. Then ecosystem respiration and CO_2 uptake balance for the rest of the year. Using the flux partitioning module of the above mentioned online tool, the Net Ecosystem Exchange (NEE), i.e. the CO_2 flux measured, has been partitioned into Gross Primary Production (GPP) and Ecosystem Respiration (Reco) according to the equation: $NEE = Reco - GPP$ and plotted as daily averages in Fig. 66. Calculating the budgets for 2017 (2016 in parenthesis), NEE sums up to -514 (-532) g C m^{-2} $year^{-1}$, GPP to -1777 (-1898) g C m^{-2} $year^{-1}$ and Reco to 1264 (1366) g C m^{-2} $year^{-1}$. Comparing 2017 to 2016 shows a similar behaviour of the ecosystem.

Comparing 2017 to 2016 it is noteworthy that NEE is very similar despite a lower GPP which is then compensated by a lower Reco.

Fig. 66 shows the latent (red) and sensible (blue) heat fluxes for 2017 as daily averages. As it is typical for dryer ecosystems, the sensible heat flux especially in summer is higher than the latent heat flux.

References

Adam, M., J. P. Putaud, S. Martins dos Santos, A. Dell'Acqua, and C. Gruening, Aerosol hygroscopicity at a regional background site (Ispra) in Northern Italy, Atmos. Chem. Phys., 12, 5703–5717, 2012

Anderson, T.L., and Ogren, J.A., Determining aerosol radiative properties using the TSI3563 integrating nephelometer, *Aerosol Sci. Technol.*, **29**, 57-69, 1998.

Arnott, W.P., Hamasha, K., Moosmüller, H., Sheridan, P.J., and Ogren, J.A., Towards aerosol light-absorption measurements with a 7-wavelength Aethalometer: Evaluation with a photoacoustic instrument and a 3 wavelength nephelometer, *Aerosol Sci. Technol.*, **39**, 17-29, 2005.

Bergamaschi P. and D. Brunner, Analysis of the sensitivity of atmospheric measurements at the JRC Ispra Atmosphere - Biosphere - Climate Integrated monitoring Station, Footprint analysis based on FLEXPART-COSMO model, JRC technical report, EUR 27131 EN, 2015.

Cavalli, F., Putaud, J.P., Toward a standardised thermal-optical protocol for measuring atmospheric organic and elemental carbon: the EUSAAR protocol, *Atmos. Meas. Tech.*, **3**, 79-89, 2010.

Cavalli, F., Alastuey, A., Areskoug,H., Cech, J., Ceburnis, D., Genberg, J., Harrison, R.M., Jaffrezo, J.L., Kiss, G., Mihalopoulos, N., Perez, N., Quincey, P., Schwarz, J., Sellegri, K., Spindler, G., Theodosi, C., Yttri,K.E., Aas,W., Putaud, J.P., 2016.A European aerosol phenomenology -4: harmonized concentrations of carbonaceous aerosol at 10 regional background sites across Europe. Atmos. Environ., 144, 133-145, 2016.

Cooke, W.F., Liousse, C., Cachier, H., and Feichter, J., Construction of a 1x1°fossil fuel emission data set for carbonaceous aerosol and implementation and radiative impact in the ECHAM4 model, *J Geophys. Res.*, **104**; 22,137-22, 1999.

Dlugokencky, E.J., P.M. Lang, J.W. Mund, A.M. Crotwell, M.J. Crotwell, and K.W. Thoning (2017), Atmospheric Carbon Dioxide Dry Air Mole Fractions from the NOAA ESRL Carbon Cycle Cooperative Global Air Sampling Network, 1968-2016, Version: 2017-07-28, Path: ftp://aftp.cmdl.noaa.gov/data/trace_gases/co2/flask/surface/

EMEP manual for sampling and chemical analysis (1995). *EMEP/CCC-Report 1/95.* (*Revised 1996; 2001; 2002).* 1995.

European Directive 2008/50/EC. On ambient air quality and cleaner air for Europe. 2008.

Gruening C., et al., JRC Ispra EMEP-GAW regional station for atmospheric research: 2008 report, EUR 24088 EN, (2009), JRC55382.

Hess, M., Koepke, P. Schult, I., Optical Properties of Aerosols and Clouds: The Software Package OPAC, *Bull. of Am. Meteorol. Soc.*, **79**; 831-844, 1998.

Jensen, N. R., Gruening, C., Adams, M., Cavalli, F., Cavalli, P., Grassi, F., Dell'Acqua, A., Martins Dos Santos, S., Roux, D., Putaud, J.-P. JRC Ispra EMEP – GAW regional station for atmospheric research, 2009 report, *EUR 24678 EN*, (2010), *JRC62602*.

Kiehl, J. T., Schneider, T. L., Rasch, P. J., Barth, M. C., Wong, J., Radiative forcing due to sulfate aerosols from simulations with the National Center for Atmospheric Research Community Climate Model, Version 3 (Paper 1999JD900495), *J. Geophys. Res.,* **105**; 1441-1458, 2000.

Koffi, E. N., Bergamaschi, P., Karstens, U., Krol, M., Segers, A., Schmidt, M., Levin, I., Vermeulen, A. T., Fisher, R. E., Kazan, V., Klein Baltink, H., Lowry, D., Manca, G., Meijer, H. A. J., Moncrieff, J., Pal, S., Ramonet, M., Scheeren, H. A., and Williams, A. G.: Evaluation of the boundary layer dynamics of the TM5 model over Europe, Geosci. Model Dev., 9, 3137-3160, https://doi.org/10.5194/gmd-9-3137-2016, 2016.

McMurry, P., Wang, X., Park, K., and Ehara, K. The relationship between mass and mobility for atmospheric particles: A new technique for measuring particle density, *Aerosol Sci. Tech*., **36**, 227–238, 2002.

Mira-Salama, D., Van Dingenen, R., Gruening, C., Putaud, J.-P, Cavalli, F., Cavalli, P., Erdmann, N., Dell'Acqua, A., Dos Santos, S., Hjorth, J., Raes, F., Jensen, N.R. Using Föhn conditions to characterize urban and regional sources of particles, *Atmospheric Research* **90**, 159–16, 2008.

Mueller, T., *Development of correction factors for Aethalometers AE31 and AE33, ACTRIS-2 workshop*, Athens, 2015, http://wmo-gaw-wcc-aerosol-physics.org.

Pépin L., Schmidt M., Ramonet M., Worthy D.E.J. and Ciais, P. Notes des Activités Instrumentales, A new gas chromatographic experiment to analyze greenhouse gases in flask samples and in ambient air in the region of Saclay, Institut Pierre-Simon Laplace (2001), http://www.ipsl.jussieu.fr.

Petzold, A., H., Schönlinner, M., Multi-angle absorption photometry - A new method for the measurement of aerosol light absorption and atmospheric black carbon, *Journal of Aerosol Science*, **35** (4), 421-441, 2004.

Putaud, J.-P., et al. (21 authors), 2004, A European aerosol phenomenology—2: chemical characteristics of particulate matter at kerbside, urban, rural and background sites in Europe. *Atmospheric Environment*, **38**, 2579-2595.

Putaud, J.-P., et al. (39 authors), 2010, A European aerosol phenomenology—3: Physical and chemical characteristics of particulate matter from 60 rural, urban, and kerbside sites across Europe. *Atmospheric Environment*, **44**, 1308-1320.

Putaud, J.P., F. Cavalli, S. Martins dos Santos, and A. Dell'Acqua, Long-term trends in aerosol optical characteristics in the Po Valley, Italy, Atmos. Chem. Phys., 14, 9129–9136, 2014.

Putaud J.P., Bergamaschi P., Bressi M, Cavalli F., Cescatti A., Daou D., Dell'Acqua A., Douglas K., Duerr M., Fumagalli I., Goded I., Grassi F., Gruening C., Hjorth J., Jensen N.R., Lagler F., Manca G., Martins Dos Santos S., Matteucci M., Passarella R., Pedroni V., Pokorska O., Roux D. JRC – Ispra Atmosphere – Biosphere – Climate Integrated monitoring Station. 2013 report, JRC report EUR 26995 EN, 2014.

Putaud J.P., Bergamaschi P., Cavalli F., Dell'Acqua A., Douglas K., Duerr M., Fumagalli I., Goded I., Grassi F., Gruening C., Jensen N.R., Lagler F., Manca G., Martins Dos Santos S., Matteucci M., Passarella R., Pedroni V., Pokorska O., Roux D. JRC – Ispra Atmosphere – Biosphere – Climate Integrated monitoring Station. 2015 report, JRC report EUR 28153 EN, 2017.

Russell, L.M.: Aerosol organic-mass-to-organic carbon ratio measurements, *Environ. Sci. Technol.*, **37**, 2982-2987, 2003.

Schmid, O., et al., Spectral light absorption by ambient aerosols influenced by biomass burning in the Amazon Basin I: comparison and field calibration of absorption measurements techniques, *Atmos. Chem. Phys.*, **6**, 3443-3462, 2006.

Stratmann, F., Wiedensohler, A. A new data inversion algorithm for DMPS-measurements. *J. Aerosol Sci.*, **27** (Suppl 1), 339-340, 1996.

Thoning, K.W., P.P. Tans, and W.D. Komhyr, Atmospheric carbon dioxide at Mauna Loa Observatory, 2. Analysis of the NOAA/GMCC data, 1974-1985., J. Geophys. Res., 94, 8549-8565, 1989.

Van Dingenen, R., et al. (28 authors), 2004, A European aerosol phenomenology –1: Physical characterization of particulate matter at kerbside, urban, rural and background sites in Europe, *Atmospheric Environment*, **38**, 2561-2577.

Weingartner, E., Saathoff, H., Schnaiter, M., Streit, N., Bitnar, B., and Baltensperger, U., Absorption of light by soot particles: determination of the absorption coefficient by means of aethalometers, *J. Aerosol Sci.*, **34**, 1445-1463, 2003.

Weitkamp, C. (editor), LIDAR Range-Resolved Optical Remote Sensing of the Atmosphere, *Springer*, New York, 2005.

WHO, Health risks of ozone from long-range transboundary air pollution, 2008.

WMO Greenhouse gas bulletin, The State of Greenhouse Gases in the Atmosphere Based on Global Observations through 2016, https://library.wmo.int/opac/doc_num.php?explnum_id=4022, 2017.Worthy D. E. F., Levin,I., Trivett N. B. A., Kuhlmann A.J., Hopper J. F., and Ernst M. K. Seven years of continuous methane observations at a remote boreal site in Ontario, Canada, J. Geophys. Res., 103 (D13), 15995-16007, 1998.

Worthy, D. E. F., I. Levin, N. B. A. Trivett, A. J. Kuhlmann, J. F. Hopper, and M. K. Ernst, Seven years of continuos methane observations at a remote boreal site in Ontario, Canada, J. Geophys. Res., 103 (D13), 15995-16007, 1998.

Zahorowski, W., S. D. Chambers, A. Henderson-Sellers, Ground based radon-222 observations and their application to atmospheric studies, J. Environm. Radioact., 76, 3-33, 2004.

Links

ACTRIS, *www.actris.eu*

ARPA Lombardia, *ita.arpalombardia.it/ITA/qaria/doc_RichiestaDati.asp*

Calipso, *www.nasa.gov/mission_pages/calipso/main*

Chemical Co-ordinating Centre of EMEP, *www.nilu.no/projects/ccc*

CLRTAP, *www.unece.org/env/lrtap/welcome.html*

EARLINET, *www.earlinet.org*

EMEP, *www.emep.int*

EPTR, European Pollutant Release & Transfer Register, prtr.ec.europa.eu/MapSearch.aspx

European Committee for Standardisation (CEN), *www.cen.eu/cen/pages/default.aspx*

EUSAAR, *www.eusaar.net*

Global Atmosphere Watch (GAW), *www.wmo.int/pages/prog/arep/gaw*

ICOS, *www.icos-ri.eu*

InGOS, *www.ingos-infrastructure.eu*

WDCA, *www.gaw-wdca.org*

World Meteorological Organization (WMO), *www.wmo.int/pages/index_en.html.*

List of figures

Fig. 1: The JRC-Ispra site and the location of the provisional EMEP-GAW station and the new atmospheric observatory, built on the spot of the historical EMEP-GAW station. 3

Fig. 2: The laboratories for atmospheric GHG measurements at Building 5 with 15m mast (left), and at the new JRC Atmospheric Observatory with the 100m-tall tower (Building 77r).......... 6

Fig. 3: Bd 5 GHG-system flow scheme 6

Fig. 4: The top panel shows a schematic of the GC-system set-up. Typical chromatograms are shown in the lower panels. 8

Fig. 5: Sampling, conditioning and distribution system diagram for the GHG measurements at the new Atmospheric Observatory (Building 77r). 10

Fig. 6: Time series of continuous CH_4 ambient measurements at Ispra (Building 5) between October 2007 and December 2017 with associated uncertainties. CH_4 ambient concentrations are reported as hourly mean values of dry air mole fractions. Furthermore, monthly mean concentrations from the background station Mace Head (MHD) on the West coast of Ireland are also included (Mace Head data from Simon O'Doherty, University of Bristol). 13

Fig. 7: Time series of continuous CO_2 ambient measurements at Ispra (Building 5) between October 2007 and December 2017 with associated uncertainties. CO_2 ambient concentrations are reported as hourly mean values of dry air mole fractions. Furthermore, flask measurements from the background station Mace Head (MHD) on the West coast of Ireland are also included (Dlugokencky, et al., 2017)... 15

Fig. 8: Time series of continuous N_2O ambient measurements at Ispra (Building 5) between September 2010 and December 2017 with associated uncertainties. N_2O ambient concentrations are reported as hourly mean values of dry air mole fractions. Furthermore, monthly mean concentrations from the background station Mace Head (MHD) on the West coast of Ireland are also included (Mace Head data from Simon O'Doherty, University of Bristol)...................... 16

Fig. 9: Time series of continuous SF_6 ambient measurements at Ispra (Building 5) between September 2010 and December 2017 with associated uncertainties. SF_6 ambient concentrations are reported as hourly mean values of dry air mole fractions. Furthermore, monthly mean concentrations from the background station Mace Head (MHD) on the West coast of Ireland are also included (Mace Head data from Simon O'Doherty, University of Bristol)...................... 17

Fig. 10: Trends in atmospheric GHG concentrations. Top panel: CO_2; middle panel: CH_4; lower panel: N_2O. The figures show daily average values, using only daytime measurements (between 12:00 and 15:00 LT) and excluding GHG measurements under stagnant meteorological conditions (with wind speed below 0.5 ms^{-1}). Solid red line: fit to daily data (based on NOAA fitting procedure [Thoning et al., 1989]); dashed red line: trend derived from fitting procedure; blue solid line: baseline concentrations at Mace Head. 18

Fig. 11: Time series of continuous CH_4 and CO_2 ambient measurements at the Atmospheric Observatory (Bd 77r), sampled at three different heights (40m, 60m, 100m), between December 2016 and December 2017. Concentrations are reported as hourly mean values of dry air mole fractions. Furthermore, monthly mean concentrations from the background station Mace Head (MHD) on the West coast of Ireland are also included (Mace Head data from Simon O'Doherty, University of Bristol)... 18

Fig. 12: ^{222}Rn measurements at Atmospheric Observatory (building 77r). The figure shows the time series of hourly mean ^{222}Radon activity, collected at 100m height, between December 2016 and December 2017. 19

Fig. 13: most recent map of the EMEP stations across Europe (2014) made available by the Chemical co-ordinating Centre (CCC)... 20

Fig. 14: Atmospheric short-lived species measurements performed at the JRC-Ispra atmospheric observatory since 1985.. 22

Fig. 15. Short-lived pollutants' data coverage for year 2017. 24

Fig. 16. Sampling inlet system for the gaseous air pollutant at the mobile lab. Inlet for the measurements is about 3.5 m above ground 27

Fig. 17: particle number size distribution observed at both ends of the horizontal part of the aerosol manifold (Dec. 2017)........ 29

Fig. 18: MAAP detection chamber (sketch from the manual of the instrument)........ 34

Fig. 19: Set-up of the EMEP- GAW station Data Acquisition System........ 36

Fig. 20: Graphic user interface of the EMEP-GAW station data evaluation........ 39

Fig. 21. EMEP inter-laboratory comparisons for rainwater analyses (1987-2017): JRC-Ispra results........ 40

Fig. 22. JRC-Ispra instrument's (#17) performance for the determination of (top) total carbon (TC) and (bottom) elemental carbon (EC/TC ratio) during the ACTRIS inter-laboratory comparison 2017-1 (ACTRIS)........ 40

Fig. 23. Solar global irradiation, precipitation amount, and temperature monthly values observed at JRC-Ispra in 2017, compared to the 1990-1999 period ± standard deviations........ 42

Fig. 24. Seasonal variations of the 24 hr averaged concentrations of SO_2, CO, NO_2, NO, O_3 and NO_x in 2017 (thin lines) and 1990-1999 monthly averages (thick lines: yellow=SO_2, blue=CO, green=NO_2, orange=O_3)........ 44

Fig. 25: AOT 40 (ppb h) and SOMO35 (ppb day) in 2017 (bars). No exceedance of the 1-hour averaged 180 µg/m³ threshold value was observed in 2017. Lines show values for the reference period 1990-1999........ 45

Fig. 26: 24hr-integrated $PM_{2.5}$ mass concentrations from off-line gravimetric measurements at 20 % RH and chemical determination of main constituents in 2017.The red line indicates the annual limit value of 25 µg/m³ to be reached by 2015 (European directive 2008/50/EC)........ 46

Fig. 27. Regressions between the gravimetric $PM_{2.5}$ measurements at 20 % RH and the sum of the $PM_{2.5}$ chemical constituents (left), and the FDMS-TEOM PM10 measurements (right) in 2017. 46

Fig. 28. 24-hr integrated concentrations of the main $PM_{2.5}$ constituents in 2017, and the relative unaccounted mass........ 48

Fig. 29. SO_4^{2-} + NO_3^- vs. NH_4^+ (µeq/m³) in $PM_{2.5}$ for 2017........ 49

Fig. 30: Average composition of $PM_{2.5}$ in 2017 for days on which $PM_{2.5}$ > 25 µg/m³ (top) and 3 < $PM_{2.5}$ < 10 µg/m³ (bottom), over cold (Jan., Feb., Mar., Nov., Dec.) and warm (Apr. – Oct.) months........ 50

Fig. 31. 24 hr – mean particle number concentrations for Dp < 600 nm and Dp >500 nm........ 52

Fig. 32. 24 hr - averaged particle geometric mean mobility diameter (from the DMPS) and standard deviation 52

Fig. 32. 24 hr - averaged particle volume concentrations for Dp< 800 nm and Dp > 800 nm........ 52

Fig. 34. Monthly mean particle number (left) and volume (right) size distributions measured in 2017 with a DMPS (10-800 nm, solid lines) and an APS (0.85-10 µm, dashed lines). Particle densities of **1.5 g cm^{-3}** for cold months and **1.1 g cm^{-3}** for warm months (May –Sept.) were used to convert aerodynamic to geometric diameters........ 54

Fig. 35. 2017 regressions between (left) $PM_{2.5}$ mass concentrations determined from gravimetric measurements at 20% RH and particle volume (Dp < 2.5 µm) calculated from DMPS and APS measurements (<40% RH), and (right) between PM_{10} mass concentrations measured with the TEOM-FDMS at 30 % RH and particle volume (Dp < 10 µm) at <40% RH........ 54

Fig. 36. Daily mean atmospheric particle light scattering (top), backscattering (middle), and absorption (bottom) coefficients at three wavelengths, derived from Nephelometer, Aethalometer and MAAP measurements (not corrected for RH) performed in 2017........ 56

Fig. 37. Comparison between the Aethalometer and MAAP derived light absorption coefficients at 660 and 670 nm, respectively. Data points are daily averages (2017)........ 57

Fig. 38. Aerosol 24-hr averaged single scattering albedo and backscatter to total scatter ratio at three wavelengths corresponding to blue, green and red, as calculated for 2017 (RH < 40%). 58

Fig. 39. Regression between the aerosol extinction coefficient and PM_{10} mass (FDMS-TEOM) and volume (DMPS + APS) concentrations in 2017. 58

Fig. 40. Aerosol vertical profile measurements performed daily with the Raman Lidar in 2017. 60

Fig. 41. Scheduled aerosol vertical profiling measurements performed monthly during the EARLINET climatology and Calipso overpass time slots in 2017. 60

Fig. 42: Examples of aerosol light backscatter profiles obtained at JRC-Ispra with the Raman LiDAR using the ACTRIS Single Calculus Chain and retrieved from the ACTRIS-EARLINET database, for July 3rd, 2017, between 19:35 and 21:00 UTC. 61

Fig. 43 (a) Precipitation amount, conductivity and (b) concentrations of 3 major ions in precipitation (bars) and pH (crosses) in 2017, and during the 1990-99 period (line). 62

Fig. 44. Wet deposition fluxes of 3 main ions measured in rain water in 2017. 62

Fig. 45. Oxidised sulphur species monthly mean concentrations and yearly wet deposition. .. 64

Fig. 46. Oxidised nitrogen species monthly mean concentrations and yearly wet deposition. . 64

Fig. 47. Reduced nitrogen species monthly mean concentration and yearly wet deposition. .. 64

Fig. 48. Particulate matter mass concentration monthly (grey) and annual (black) averages. The red line is the long term trend over annual averages. All values are gravimetric measurements or estimates from gravimetric measurements. 66

Fig. 49. Ozone yearly and monthly mean concentrations at JRC-Ispra. 66

Fig. 50. AOT40, SOMO35 values, and number of O_3 limit value exceedances. 66

Fig. 51. Particle number (left) and volume (right) monthly mean concentrations. 68

Fig. 52. Aerosol green light scattering and absorption monthly mean coefficients 68

Fig. 53. Aerosol optical characteristics at 550 nm (monthly means): single scattering albedo and backscatter ration (left hand axis) and scattering Ångström exponent (right hand axis). 68

Fig. 54: the flux tower of 24 m at the Pinus pinea site in San Rossore 72

Fig. 55: Measurement principle of sonic anemometers, sketch from www.gill.co.uk 77

Fig. 56: LI-7200 analyser head (from www.licor.com), arrow indicates sampling volume 77

Fig. 57: Sketch of a soil heat flux sensor (drawing from www.wikipedia.org) 79

Fig. 58: Principle of water level calculation using the Diver (sketch from www.swstechnology.com). 79

Fig. 59: Daily averages of air temperature (left) and daily sum of precipitation (right) as measured in the Parco San Rossore. 82

Fig. 60: Daily averages of short wave incoming radiation (top) and incoming photosynthetic active radiation (bottom). 82

Fig. 61: Wind rose for 30 min. averages of wind measurements with wind speed >0.5 m/s. Red: directions of the wind origin, blue: average wind speeds per direction interval in a.u. 83

Fig. 62: Profiles of soil temperature (top) and soil water content plus water table (bottom) measured as daily averages. 84

Fig. 63: Soil heat fluxes measured with three identical sensors located some meters apart. . 84

Fig. 64: Daily averages of measured (blue), gap filled (red) and cumulated (green) CO_2 fluxes. 86

Fig. 65: Daily averages of latent (red) and sensible (blue) heat fluxes. 86

Fig. 66: Daily averages of NEE, GPP and Reco. 86

List of tables

Table 1: Measurement sequence of Picarro G2401. This cycle is repeated continuously every hour. 12

Table 2: Variables related to short-lived pollutants and radiative forcers measured in 2017.. 24

Table 3: Parameters of the EUSAAR-2 analytical protocol 35

Table 4: Annual mean concentrations and contributions of major $PM_{2.5}$ constituents in 2016. 51

Table 5: Mean aerosol chemical composition ($PM_{2.5}$) in 2017 and extinction cross section..... 59

Table 6: Statistics relative to the precipitation samples collected in 2017 (averages are volume weighted). 63

Table 7: ICOS class 2 Ecosystem Station core parameters. 74

Table 8: ICOS variables measured continuously during 2017 in San Rossore 74

Table 9: Processing steps for flux calculations using the EdiRe Software package. 80

Table 10: Total number of flux data points and percentage of data points with quality flags according to the Carboeurope methodology (H: sensible heat, LE latent heat, FC CO_2 flux). . 85

KJ-NA-29638-EN-N

The European Commission's science and knowledge service

Joint Research Centre

JRC Mission

As the science and knowledge service of the European Commission, the Joint Research Centre's mission is to support EU policies with independent evidence throughout the whole policy cycle.

EU Science Hub
ec.europa.eu/jrc

@EU_ScienceHub

EU Science Hub - Joint Research Centre

Joint Research Centre

EU Science Hub

Publications Office

doi:10.2760/698101

ISBN 978-92-79-99284-1